Nanostructured Materials for Tactile and Catalytic Applications

by

Long Pu

A thesis

presented to the University of Waterloo

in fulfillment of the

thesis requirement for the degree of

Doctor of Philosophy

in

Chemistry (Nanotechnology)

Waterloo, Ontario, Canada, 2018

Examining Committee Membership

The following served on the Examining Committee for this thesis. The decision of the Examining Committee is by majority vote.

External Examiner   Igor Zhitomirsky

                           Professor

Supervisor   Vivek Maheshwari

                           Associate Professor

Internal Members   Tong Leung

                           Professor

                           Rodney Smith

                           Assistant Professor

Internal-external Member   Youngki Yoon

                           Assistant Professor

Author's Declaration

This thesis consists of material all of which I authored or co-authored: see Statement of Contributions included in the thesis. This is a true copy of the thesis, including any required final revisions, as accepted by my examiners.

I understand that my thesis may be made electronically available to the public.

Statement of Contributions

This thesis contains material from several published journal papers that I authored or co-authored, some of which resulted from collaboration with my colleagues in the Maheshwari group.

- Part of the content in Chapter 1 has been published in

    L. Pu, M. Baig, V. Maheshwari, *Anal. Bioanal. Chem.* **2016**, *408*, 2697.

    Long Pu and Maarij Baig contributed equally to this work.

- Part of the content in Chapter 2 has been published in

    L. Pu, R. Saraf, V. Maheshwari, *Sci. Rep.* **2017**, *7*, 5834.

    Long Pu and Rohit Saraf contributed equally to this work. V. Maheshwari planned the idea, L. Pu and R. Saraf conducted the experiments, and all authors analyzed and discussed the results and contributed to the writing of the manuscript.

- Part of the content in Chapter 3 has been published in

    R. Saraf, L. Pu, V. Maheshwari, *Adv. Mater.* **2018**, 1705778.

    Long Pu and Rohit Saraf contributed equally to this work. V. Maheshwari planned the idea, R. Saraf carried out the synthesis of the perovskite film and device fabrication. L. Pu and R. Saraf conducted the experiments, and all authors analyzed the discussed the results and contributed to the writing of the manuscript.

- The content in Chapter 4 has not been published yet. However, it is in a near-verbatim state to what is intended for submission.

Abstract

In response to the needs of the modern information-rich society, there is an increasing demand for multifunctional materials with novel properties to advance the development of the new-generation electronics. To synthesize these materials, many biomaterials have been extensively studied and research suggests that their outstanding performance is strongly related to the sophisticated hierarchical structures. Since the development of nanotechnology, numerous nanostructured materials have been reported to exhibit unprecedented performance by mimicking the structures of biological materials. However, there is still a significant gap between experimental research and commercialization of the nanostructured materials, as a result of the typical high-cost fabrication procedures involving lithography or patterning process. Thus, developing new nanostructured materials that can be fabricated with ease can greatly advance their use in practical applications. Inspired by the growth of the biological materials, this dissertation investigates the facile synthesis and explores the use of two types of nanostructured materials, which are three-dimensional hierarchical ZnO nanostructure and self-assembled Au nanoparticle chains.

3-D ZnO nanostructures are synthesized using electrochemical methods by combining 2-D nanosheets with 1-D nanorods. These structures made in high density without any patterning process can be easily assembled over a large area. Upon the application of pressure, the hierarchical structures lead to a highly sensitive and dynamic modulation of the conductive pathways. The tactile sensor made of the high density nanostructured material shows an outstanding sensitivity in the low-pressure regime with a 0.4 Pa limit of detection and a response time of less than 2 ms. The ZnO structures can also detect temperature changes with a non-linear response similar to skin perception in the 298-400 K range. Combining both the pressure and temperature sensitivities, the device is able to differentiate between 20 μl and 40 μl water droplets and also differentiate between 10 μl droplets of room temperature and 323 K. Such performance in a single device which can be prepared by a simple fabrication procedure will bring the tactile sensor closer to skin ability and make this type of devices easily accessible at the same time.

Combining the ferroelectric and semiconducting nature of organolead trihalide perovskite $MAPbI_3$, a light harvesting, self-powered monolith tactile sensor is fabricated. ZnO nanostructure on the $MAPbI_3$ film serve as a pressure-sensitive drain whose interfacing area modulates in response to the applied pressure. The sensor is operational for at least 72 h with just light illumination after consuming 55 $\mu W \cdot h\ cm^{-2}$ energy during the poling process. A linear response is observed till 76 kPa with a sensitivity of 0.57 kPa^{-1} which can be modulated by the strength of the external electric field.

Additionally, PtRu/Au catalysts for ethanol oxidation is synthesized using self-assembled Au nanoparticle chains linked by Pt^{4+} and Ru^{3+} cations. The facile assembly process allows the easy

optimization of the relative amounts and relative placement with respect to each other. By inter-mixing the chains at varying stages of assembly, spatial control of distinguishable domains of Pt and Ru on the size of 5-10 nm is achieved. The electrocatalytic activity of the synthesized catalyst is 3.1 times that of commercial Pt/C. The catalyst also shows a higher carbon monoxide-tolerance by negatively shifting the CO oxidation peak for about 0.1 V. Compared to the homogenous mixed catalyst, a 29 % increase of current density is observed for the catalyst with well-defined domains.

The findings of this research therefore provide insights for synthesis of nanostructured materials with unprecedented properties using cost-effective methods instead of complex lithography or patterning process. Such simple fabrication procedures extend our knowledge of preparing and use of similar nanostructured materials in a wide range of applications.

Acknowledgements

First of all, I would like to express my deepest appreciation to my supervisor, Professor Vivek Maheshwari, for giving me the opportunity to work in his group in the first place and for guiding me throughout the six years of my graduate study. His expertise, insights and patience has led me to solve countless problems that I encounter. I could have achieved nothing without his guidance and help.

I would like to also thank all my committee members: Professor Tong Leung, Professor Eric Prouzet, and Professor Youngki Yoon for answering my questions when I needed guidance.

Special thanks go to my colleagues and friends: Rohit Saraf and Maarij Baig. We have spent countless hours working together in the lab and it was my pleasure to work with you. I would like to also thank other colleagues in the lab: Hua Fan, Shehan Salgado and Venkatesh Gurupsarad for their support.

Finally, I would like to acknowledge the support from my family. It was your love and care which gave me the strength and courage to pursue my goals.

Table of Contents

List of Figures

xi

List of Tables

List of Abbreviations

Abbreviations	Full Names
CNT	Carbon nanotubes
PDMS	Polydimethylsiloxane
CV	Cyclic voltammetry
PEMFC	Proton-exchange membrane fuel cell
DEFC	Direct-ethanol fuel cell
EOR	Ethanol oxidation reaction
ITO	Indium tin oxide
FESEM	Field emission scanning electron microscopy
EDS	Energy-dispersive X-ray spectroscopy
GIXRD	Glancing incidence X-ray diffraction
DLS	Dynamic light scattering
UV-Vis	Ultraviolet-visible spectroscopy
XPS	X-ray photoelectron spectroscopy
TEM	Transmission electron microscopy
GCE	Glassy carbon electrode
CA	Chronoamperometry
ECSA	Electrochemical active surface area

Chapter 1

Introduction

1.1 Nanostructured Materials

Multifunctional materials with novel physical and chemical properties are the essential components and they play a critical role in the new-generation electronics, such as flexible electronic skins, energy storage devices, sensors, catalysts, wearables, and medical devices.[1–3] Many biomaterials exist with exceptional performance and high mechanical durability in nature.[4–7] Research efforts have been devoted to study biomaterials for fabrication of manmade materials with similar properties. Evidence suggests that the growth/synthesis of the biological materials generally occur at room temperature with limited supply of resources for living life forms, whereas their outstanding performance is strongly related to the sophisticated hierarchical structures at micro or nanoscale.[2,5,8,9] However, the fabrication of manmade multifunctional materials has been challenging using the traditional methods and techniques. One of the main obstacles was the controlled manipulation of the microstructures with limited preparation approaches. Since the recent development in nanotechnology, there has been a remarkable increase interest in the fabrication and characterization of nanostructured materials, as a major area of research within the field.[10–12] While numerous papers on nanostructured materials have been published for various applications with unprecedented performance, there are few studies that have investigated the preparation of these materials without complex patterning or lithography process.

It is necessary here to clarify what is meant exactly by "nanostructured materials". The term has been used to refer to "materials with a microstructure the characteristic length scale of which is on the order of a few nanometers".[11] Previous research has established the importance of structure on materials' physical and chemical properties.[6,13,14] An extreme but well-known example is the transformation from graphite to diamond. Similar to the structure change at the atomic scale, alteration of structure at the micrometer scale has a profound effect on the

macroscopic properties, such as the superhydrophobicity of lotus leaf, adhesion of gecko feet, and durability of spider silk.[5,15–17]

Hundreds and thousands of nanostructured materials have been prepared via various advanced techniques. For commercialization of these materials in industry, ease of fabrication and integration are of great significance. Despite the rapid development in nanostructured materials for sensing and catalytic applications, preparations of the nanostructured materials have been mostly restricted to complex processes involving patterning and lithography.[5,10,18–20] There has been little discussion on the facile synthesis methods, in which no patterning or lithography is involved. Therefore, developing new nanostructured materials which can be fabricated with ease can significantly benefit the commercialization and use of these materials in a diverse range of applications.

Inspired by the motivations presented above, the objectives for this dissertation are to investigate the facile fabrication and explore the use of two different types of nanostructured materials – three-dimensional (3-D) hierarchical ZnO nanostructures and self-assembled Au nanoparticle chains. The nanostructured materials are prepared and characterized respectively for tactile sensing and catalytic applications (details in Chapter 2, 3, and 4).

1.2 Tactile Sensing

Skin, the large sensory organ of the human body, is highly sensitive to a diverse range of tactile stimuli.[21,22] As the most sensitive touch sensor known, human skin can detect gentle touches of around 1 kPa. Additionally, a human finger can differentiate surface roughness at a at a spatial resolution of about 40 μm by moving back and forth across the surface. Apart from detecting the normal touch (tactile), skin is also capable of sensing temperature, pain, itch, and even pleasure, while working as the sensory transduction system at the same time. The extraordinary performance can be attributed to the hybrid system in which the dermis transmits the mechanical contact to the neuron imbedded in it.[22] With the capability of simulating skin to a certain extent, electronic skin (e-skin) is fast becoming a key component in various applications, including robotics, wearable sensors, and healthcare devices.[19,23,24] As the critical element in e-skins, tactile sensors with performance on par with human analogues are in great demand. Extensive research has been done to develop tactile sensor with superior properties, such as high sensitivity, flexibility, and the ability to distinguish static and dynamic stress.[20,25,27]

Capacitive, resistive, and transistor-based tactile sensor have been fabricated, in which the primary sensing basis is the change in electrical response to change in pressure.[25–27] Since the development of nanotechnology, most research in tactile sensor has emphasized the use of nanostructured materials with unique properties. Structural interlocking and multi-contact pathways as a result of the complex structures are the predominant advantages.[28–30] Typical nanomaterials used for tactile sensors includes conductive polymer nanofibers, carbon nanotubes (CNTs), graphene and semiconducting (Si, ZnO) materials.[27,29,31] However, most nanostructured materials suffer from the high cost and complex lithography process associated with the fabrication.

In nature, unprecedented performance is achieved by hierarchical structures made without any lithography process.[9] Biological composites typically have a gradient composition of structures from micron to nanoscale. These sophisticated hierarchical structures maximize the structural functions in response to environmental changes.[5,6] Inspired by nature, extensive research have been devoted to mimic the biological morphologies for

better performance. Pang et al. demonstrated a strain sensor with interlocking nanofiber arrays mimicking the wing-to-body locking microstructures.[28] Polydimethylsiloxane (PDMS) micropillars decorated with ZnO nanowire arrays have been developed by Ha et al.[20] These bioinspired nanostructured materials show high pressure sensitivities with fast response times which can significantly benefit the development of many tactile sensing-based applications.

1.2.1 3-Dimensional ZnO Nanostructure

Hierarchical nanostructures are tailored and used routinely in nature to accomplish tasks with high performance. Their formation in nature is accomplished without the use of any patterning process. Inspired by such structures, We combined 2-D ZnO nanosheets with 1-D nanorods in high density without any patterning process, and the use of the resulting nanostructured material for tactile and thermal sensing is examined in Chapter 2 and 3, respectively.

Zinc oxide, with a chemical formula of ZnO, is a water-insoluble white powder. ZnO is classified as a semiconductor in the group II-VI, with a wide band gap of ≈ 3.3 eV at room temperature and an intrinsic doping of n-type.[32–34] The compound ZnO does exist as a mineral zincite in nature, but most ZnO is manufactured synthetically. Due to its wide range of properties, including the large band gap, relatively high electron mobility, high transparency, and piezoelectricity, ZnO has attracted much academic interest.[35,36] The commercially synthesized ZnO has been used as a multifunctional material in numerous applications such as: dye-sensitized solar cells, transparent electrodes, and batteries, as a result of its unique properties.[12,33,36] Manufacturing of ZnO can be accomplished through various techniques, including chemical vapor deposition, thermal evaporation, and electrochemical deposition.[32]

ZnO is one of the few semiconducting and piezoelectric materials that form self-assembled nanostructures in specific orientations.[37–39] Well-defined nanostructures, such as nanowires, nanorods, nanosheets, and nanorings have been successfully synthesized using various methods, owing to its wurtzite crystal structure. In this dissertation, 3-D ZnO nanostructure is made electrochemically by hierarchical growth of 1-D nanorods on the 2-D nanosheets.

Both morphologies of ZnO are deposited by electrochemistry without using any patterning process. During the deposition, crystal growth along the c-axis is favored. The reason for the preferentially growth is the electrostatic deposition of zincate ion – $Zn(OH)_4^{2-}$ on the (0001) plane. Consequently, the anisotropic growth leads to the formation of 1-D nanorods.[40-42] To synthesize 2-D nanosheets, Cl^- is added to the electrolyte to selectively bind to the (0001) plane. The adsorption prevents the contact of $Zn(OH)_4^{2-}$ to the top surface and results in growth of nanosheets. Lastly, the nanorods grow predominately on the large surface side of the sheets due to its lower resistance and crystal orientation to form 3-D nanostructures (details in Chapter 2).

The high density hierarchical structures lead to a highly sensitive and dynamic modulation of the conductive pathways with pressure. In Chapter 2, I investigate a tactile and thermal sensor made of the 3-D ZnO nanostructures. The sensor can detect pressure as low as 0.4 Pa, with a response time in milliseconds. A light harvesting, self-powered tactile sensor is made by using ZnO nanosheets as pressure-sensitive drain on a $MAPbI_3$ film in Chapter 3. Organolead trihalide perovskite $MAPbI_3$ shows a distinctive combination of properties such as being both ferroelectric and semiconducting, with ion migration effects under poling by electric fields. Once poled, the sensor is operational for at least 72 h with just light illumination. The sensor is monolithic in structure and has a linear response till 76 kPa. These tactile sensors are discussed in detail in Part A (Chapter 2 and 3).

1.3 Ethanol Oxidation

Energy conversion/storage has become one of the most popular topic in the past decades, to meet the increasing need of energy of the information-rich society.[43–45] Fuel cells have drawn much research efforts as a prominent energy conversion device for sustainably converting chemical energy to electrical energy. They are known to have sustained operation at high current density, electrical efficiencies, and fuel utilization, along with the heat and power generation capability at end-use sites.[46,47]

Hydrogen is the most widely used fuel in proton-exchange membrane fuel cells (PEMFCs), as a result of its low operating temperature, light weight and no greenhouse gas emissions.[46] However, the commercialization of PEMFCs is hindered by the lack of hydrogen storage and transport technologies. As a good alternative to hydrogen, small organic molecules (methanol, ethanol, formic acid), which are in liquid forms, can be transported much more easily through the existing infrastructure.[48] Among various types of small organic molecules, ethanol draws a significant amount of research attention because of its low toxicity and wide availability. Nevertheless, the utilization of ethanol in fuel cells is not fully developed for commercialization, owing to the low power densities and lifetimes of direct-ethanol fuel cells (DEFCs).[47] The lack in performance can be attributed to the kinetics of ethanol oxidation reaction (EOR), which is a complex process that requires relocating of 12 electrons per ethanol molecule and breaking of the C-C bond[49,50]: $C_2H_5OH + 3H_2O \rightarrow 2CO_2 + 12H^+ + 12e^-$ (1.1)

In contrast, electrooxidation of hydrogen and methanol involve only 2 and 6 electrons. Consequently, intense research efforts have been devoted to developing new anode catalysts to improve the electrode kinetics of EOR.[49–51] Noble metals have been used widely as catalytic materials at the anode of DEFCs owing to their excellent ability to adsorb and desorb target molecules. Specifically, Pt exhibited a unique ability in breaking the C-C bond in acidic solutions despite the high cost related to its rarity.[51] Nevertheless, instead of the complete oxidation of ethanol to CO_2, typically acetaldehyde (two-electron oxidation) or acetic acid (four-electron oxidation) are formed during the process.[50,52,53] The intermediates will preferably bind to available sites on Pt surface and consequently hinder the

adsorption of more ethanol molecules. The process was reported as the "poisoning effect", and it has been shown to significantly decrease Pt's performance over time. To overcome the challenges, binary or ternary Pt-based catalysts have been studied by many research groups. Ru, Rh, Au, Sn, and Ni have been reported for exhibiting outstanding catalytic performance as co-catalyst with metallic Pt.[53,54] Predominantly, PtRu catalysts demonstrated the exceptional ability for the electrooxidation of CO compared to other bimetallic catalysts by promptly oxidizing the surface adsorbed CO and CH_X-type adsorbates.[55,56]

Fabrication of Pt-based nanostructures has attracted much research attention for enhancing the catalytic properties during the past decades. Many papers have focused on developing nanostructured materials based on Pt and shown outstanding performance by providing more available active sites compared to macroscopic Pt materials.[53,58] Additionally, another successful approach to reduce the cost while maintaining the high surface area is depositing a thin layer of Pt-based materials on nanoscale structures. Graphene, CNTs, and TiO_2 matrices have been used as supporting materials for effectively catalyze ethanol oxidation reactions.[57,58,59]

1.3.1 Self-Assembled Nanoparticle Chains

The second approach that we took towards the nanostructured materials is the self-assembled nanoparticle chains. Nanoparticles have been used as building blocks for developing nanostructured materials.[60-62] Instead of using a single nanoparticle, I report a facile fabrication of PtRu catalysts for EOR using nanoparticle chains assembled with Pt^{4+} and Ru^{3+}. The chain-like catalyst shows well-defined domains of Pt and Ru, which notably increase the catalytic performance (details in Chapter 4).

Gold (Au) have been investigated as one of the most ancient topics owing to its stability. As the most stable metal nanoparticles, Au nanoparticles possess fascinating properties including self-assembly, size-related electronic, optical, and magnetic characteristics.[63,64] Because of its compelling properties, Au nanoparticles have been used as building blocks in the bottom-up design for applications in biochemistry and catalysis.[63,65] Apart from single nanoparticles, various types of assembled structures of Au have been reported for use in nanostructured

materials.[66,67] With no complex patterning process, self-assembly has been reported to be an easy and cost-effective method to organize nanoparticles into chains. Nanoparticles are usually stabilized with capping agents to form stable colloidal suspensions. The functionality of the capping agent has been used to self-assemble the particles into distributed chains (branched 1-D arrays). Typically, the citrate-capped Au nanoparticles suspended in aqueous medium have a negative zeta potential and can be brought into close physical proximity through controlled addition of ionic linkers. As a result of the electrostatic force, the nanoparticles and linkers self-assemble to form chains. Ultraviolet-visible spectrophotometry have been used to monitor the assembly of 0-D nanoparticle into higher ordered nanostructures. The wavelength for peak absorbance associated with the surface plasmon of the nanoparticle undergoes a redshift because of its delocalization over adjacent nanoparticles upon self-assembly.

We have previously reported a hybrid nanostructure combining Au chains with ZnO nanorods.[68] Similarly, starting with self-assembled chains, I explored the utilization of PtRu catalyst on these chains for EOR in Part B (Chapter 4). The self-assembly process of Au nanoparticle chains enables the control over the spatial distribution of multiple catalysts. Additionally, the chain-like structures work as a template to assure effective dispersion of catalysts. The spatially confined growth on Au nanoparticle chains maximizes the exposing surface area for effective catalytic process. The catalyst shows good performance in both EOR and stability, and it is 29 % higher in specific activity compared to samples that are homogeneously dispersed with no spatial control. Compared to commercial Pt/C catalyst, a 207% increase in specific activity is observed. (details in Chapter 4).

1.4 Thesis Organization

This dissertation is organized into two parts with five chapters.

Part A of this dissertation contains Chapter 2 to 3. In this part, the three-dimensional ZnO nanostructures is studied for tactile sensing applications. Chapter 2 specifically discusses use of the interlocking random ZnO 3-D structures for tactile and thermal sensing. In Chapter 3, a self-powered tactile sensor is fabricated by combining the $MAPbI_3$ perovskite with ZnO nanostructures.

Part B of this dissertation includes Chapter 4, and this part explores the use of self-assembled nanoparticle chains for catalysts preparation. PtRu nanocomposites with spatial distribution is fabricated and shows good specific activity for EOR.

Chapter 5 concludes this dissertation with summarized findings and proposed future work.

Part A

Nanostructured Materials for Tactile Sensing

Chapter 2

Bio-Inspired Interlocking Random 3-D Structures for Tactile and Thermal Sensing

2.1 Introduction

Hierarchical structures with mechanical and functional integration of distinct nanomaterials and/or morphologies in a cohesive manner show many remarkable features and properties.[1,2,69–71] As a result, such structures made with multiple micron and nano scale components are being actively studied for use in diverse devices ranging from high surface area current collectors in batteries,[72–74] solar cells[75,76] and supercapacitors,[77,78] to biomimetic adhesives[16,79,80] and as surface coatings.[15,81,82] In nature such hierarchical structures, made without the use of any lithography or pattering processes, are ubiquitously present and are used to accomplish specific tasks with great efficiency and unparalleled performance.[83–85] The ongoing expansion of robotic and humanoid platforms requires the development of sensory interfaces such as electronic skin (or tactile sensors), with performance on par with human analogues.[86–88] This will also impact other areas of tactile sensing application such as wearable sensors and medical devices.[24,34,89–91] Electronic skin (or tactile) devices that sense pressure have been made using hair-like patterned polymer nanofibers,[31,33] CNT and graphene networks,[29,92–95] hollow sphere microstructures[96] and ZnO rods on patterned PDMS micro pillars,[20] among others. Structural interlocking and multi-contact conductive pathways that lead to inherent piezo-resistive and percolation effects are the primary basis of pressure sensing in these devices.[33,97] Lithography and/or patterning process are typically involved during the fabrication of similar devices with such complex structures. Being a large area device (human skin has an area of ~ 2 m^2, and specifically the palm and fingers have an area of ~ 120 cm^2), the translation of non-patterned hierarchical structures as tactile

sensors (or electronic skin) will lead to significant benefits due to ease of fabrication and integration. This has to be coupled with high sensitivity and rapid response time for sensing of pressure and a robust integrity.[27,31,32,98] Besides pressure, integrated temperature sensing will significantly enhance the capabilities of such electronic skin devices bringing them closer to the multi-functional capabilities of human skin.[21,25,99,100] By using a rationally designed hierarchical structure we address these requirements as reported below.

The electronic skin sensor is made by rationally combining 1-D ZnO nanorods (length scale 400 nm) onto 2-D ZnO sheets (length scale of micron) as a hierarchical structure, using simple electrochemical synthesis and without any patterning process. Compared to similar hierarchical structures made using lithography process, this sensor has, an exceptional sensitivity (greater than 10^5 times change in resistance) in the low-pressure regime, a minimum pressure sensing threshold of at least 0.4 Pa with a response time of less than 2 ms and also the ability to sense temperature. We show that the sensor is able to differentiate between 20 µl and 40 µl water droplets and also differentiate between 10 µl droplets of room temperature and 50 °C. The temperature and pressure stimuli can be differentiated based on their response time scales, which are in seconds and milliseconds respectively. By comparing the response characteristics of sensors with different structuring elements, the exceptional performance of the hierarchical sensor is attributed to its inter-locking structure and the formation of multi-contact pathways due to the rational combination of nanorods with sheets. The number of pathways increases rapidly with pressure leading to the pressure sensing ability. Further, the hierarchical template is used as a pseudocapacitor by conformal electrochemical deposition of a MnO_2 layer, and compared to planar counter parts it shows an order of magnitude improvement in energy density. The increase in energy density indicates the high surface area of the ZnO nanostructured template which will be advantageous for application in supercapacitors.

2.2 Materials and Methods

2.2.1 Synthesis

Hierarchical Electrochemical Deposition of ZnO Nanostructures and MnO$_2$: Indium tin oxide (ITO) coated glasses with a surface resistivity of 10 Ω/sq obtained from Delta Technologies were used as substrates for the hierarchical growth of ZnO nanostructures. The electrochemical deposition was carried out by using an Ivium CompactStat Electrochemical Analyser with a standard three-electrode setup. A Ag/AgCl electrode was used as the reference electrode, with a platinum wire as the counter electrode for all depositions. Different substrates were connected to the working electrode during each step of the deposition. For the ZnO nanosheets, a clean ITO substrate was used as the working electrode. A constant electric potential of -1.0 V was applied for one hour. 0.028 M ZnCl$_2$ with 0.1 M KCl aqueous solution was used as the electrolyte. A beaker filled with the electrolyte solution was immersed in a silicon oil bath, which was heated on a hot plate, to maintain a steady temperature of 75 °C during the deposition. Substrates were washed thoroughly with Millipore water after the deposition and dried under a nitrogen stream. The substrates were then heated at 350 °C for one hour for the annealing of ZnO nanosheets. A thin layer of gold (~15 nm) was coated on ZnO nanosheets using magnetron sputtering to improve the surface conductivity. For deposition of nanorods, the substrate was again used as the working electrode. Same voltage of -1.0 V was applied for the same amount of time at the same temperature as in the first step. A lower concentration of 1.25 mM ZnCl$_2$ with 0.1 M KCl aqueous solution was used as the electrolyte.[42] Same cleaning and annealing process was followed. To electrochemically deposit a film of MnO$_2$ on the ZnO nanostructured template, a thin layer of gold was sputtered again for improving the surface conductivity on the substrate with the pre-deposited ZnO nanostructures. The substrate was then immersed in a plating solution of 20 mM Mn(NO$_3$)$_2$ with 100 mM NaNO$_3$. A constant current density of 100 μA cm^{-2} was applied for 5 minutes. The substrate was washed with Millipore water after the deposition to remove excessive electrolyte and then annealed on a hot plate at 60 °C for one hour.

2.2.2 Characterizations

A Zeiss Ultraplus Field-emission Scanning Electron Microscope (FE-SEM) equipped with energy-dispersive X-ray spectroscopy (EDS) was used to examine the morphologies of the hierarchical ZnO structure and MnO_2 nanoparticles. The crystal structures were characterized by glancing incidence X-ray diffraction (GIXRD) using a PANalytical X'Pert Pro MRD diffractometer with Cu Kα radiation ($\lambda = 1.54$ Å) at an incidence angle of 0.4°. A Keysight 3458A Digital Multimeter and a Keysight 6614C 50 Watt Power Supply were used for measuring current responses and applying the potential bias, respectively. Our samples were connected in series with the multimeter and power supply to form a circuit. A two-probe method was used by connecting one probe to the ITO layer on the bottom substrate directly and connecting the other probe to the ITO substrate on the top sample through a very small amount of Gallium-Indium eutectic. By using the highly conductive liquid metal alloy, we could maintain a good electric contact with minimum pressure. An MFA Motorized Miniature Linear Stage was used to apply the load to the samples. A Honeywell Model 31 Miniature Load Cell was connected to the stage for measuring the load. Combined with a Micro-pro series digital panel meter, we were able to read out the measurements and record the data. Pressure values were determined by dividing the weight by the contact area between the top and bottom samples. For the temperature sensitivity test, the temperature of the samples was controlled by changing the temperature setting on a hot plate on which the samples were placed. Accurate temperature readings on the sample surface were measured by an infrared thermometer. Electrochemical characterizations were done again by using the Ivium CompactStat Electrochemical Analyser. For cyclic voltammetry and galvanostatic charge/discharge testing, two symmetric samples were separated by a porous ion-permeable membrane (separator) as the working and counter electrodes, with a Ag/AgCl electrode as the reference electrode.

2.3 Results and Discussion
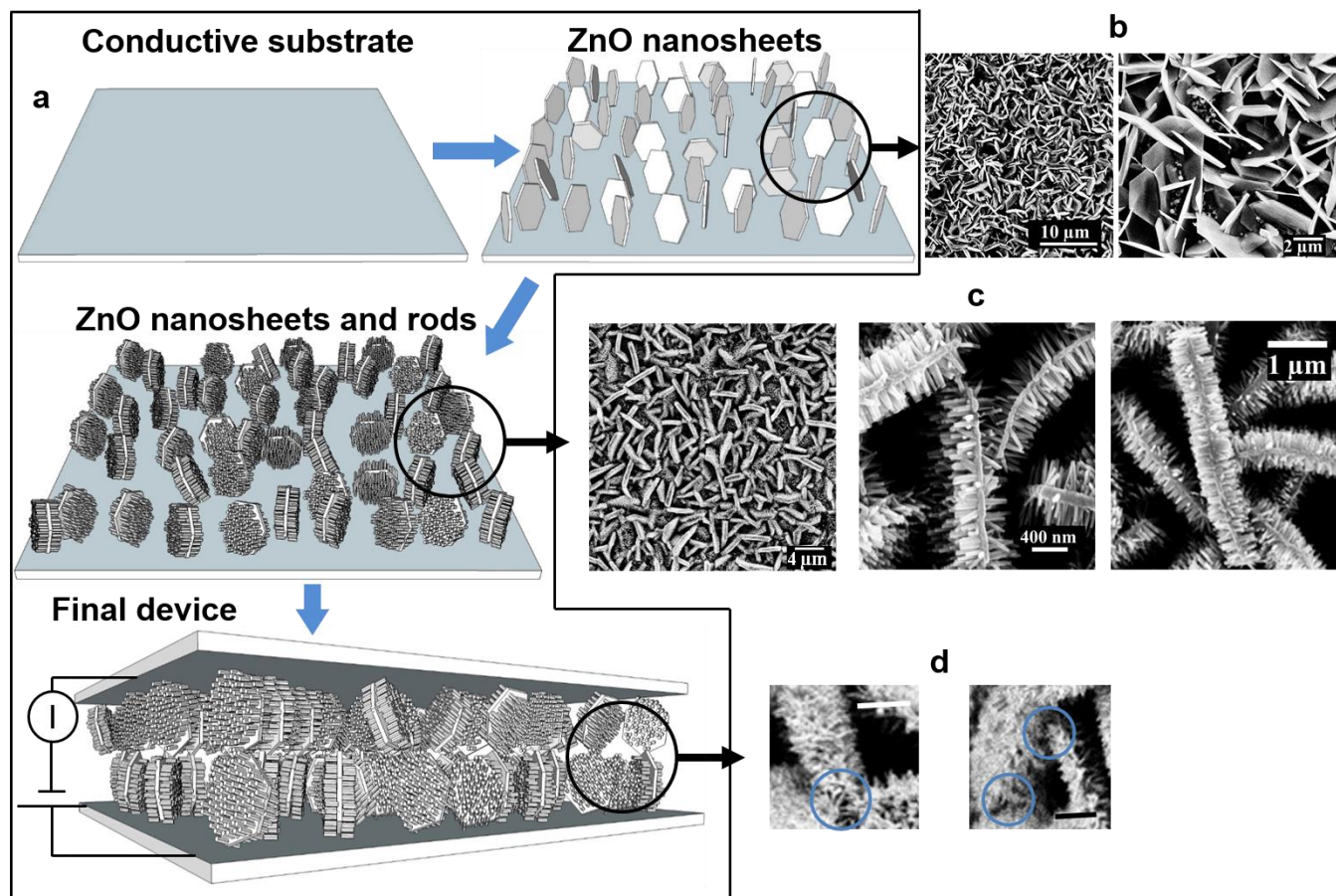
Figure 2.1. (a) Schematic showing the formation of the device structure. (b) FESEM images showing the ZnO sheets that form the first layer of the device. The higher resolution image on the right shows that the sheets are microns in size with a thickness on the scale of 50-200 nm. (c) FESEM images of the sheet-rod nanostructure. The image on the left shows the high density of the structure. The higher resolution images on right clearly show the sheet outline and the rods growing primarily on the larger area plane of the sheets. The length of the rods is 200-400 nm. (d) The cross section of the final device structure shows the interlocking between the sheet-rod nanostructure of the top and bottom electrodes. This has been highlighted in blue. The scale bars are 1 μm.

The schematic of the sensor is presented in Fig. 2.1a. The sensor is made by first forming 2-D ZnO nanosheets (Fig. 2.1b) on a planar conductive substrate, followed by formation of ZnO nanorods (Fig. 2.1c). Both morphologies of ZnO are made electrochemically and are controlled by varying the composition of the electrolyte solution.[42,101] The 1-D rods grow predominately on the large surface area side of the sheets due to its lower resistance and crystal orientation, as can be seen in the field emission scanning electron microscopy (FESEM) images of Fig. 2.1c and X-

ray diffraction data (XRD details in Appendix). The final ZnO sheet-rod nanostructure is a dense array of these 2-D-1-D units. Two such substrates are placed together and sealed with PDMS. A cross section of the device showing the interlocking contacts is presented in Fig. 2.1d.

The response of the device to typical pressure cycles is shown in Fig. 2.2a and an over 10^5 order change in current is observed on increasing the pressure to 6.5 kPa. The response is consistent over repeated fast pressure cycling (100 cycles of 10 kPa) as observed in the inset of Fig. 2.2a. The response time of the sensor is measured as 1.38 ms, on subjecting it to a step change of 10 Pa in pressure that occurs within 20 ms and is illustrated by Fig. 2.2b. The current accurately tracks the change in pressure, signifying the rapid response from the device. The fast response time in pressure is indicative of the rapid change in the density of conductive pathways in the device. Further as the device structure is made with ZnO this limits viscoelastic effects in the response. The correspondence between the current and pressure is more clearly illustrated in Fig. 2.2c, the response of the device is in step with the pressure profile tracking both negative and positive derivatives in the pressure-time profile (inset of Fig. 2.2c). The sensitivity of the device to pressure is illustrated in Fig. 2.2d, the current changes by 2.2 and 9 times respectively on placing 20 µl (~ 0.8 Pa) and 40 µl (1.6 Pa) water droplets in succession, and it reverts to the original level on removing 40 µl the droplet. As illustrated below, the formation of the sheet-rod structure is the key to achieving this performance.
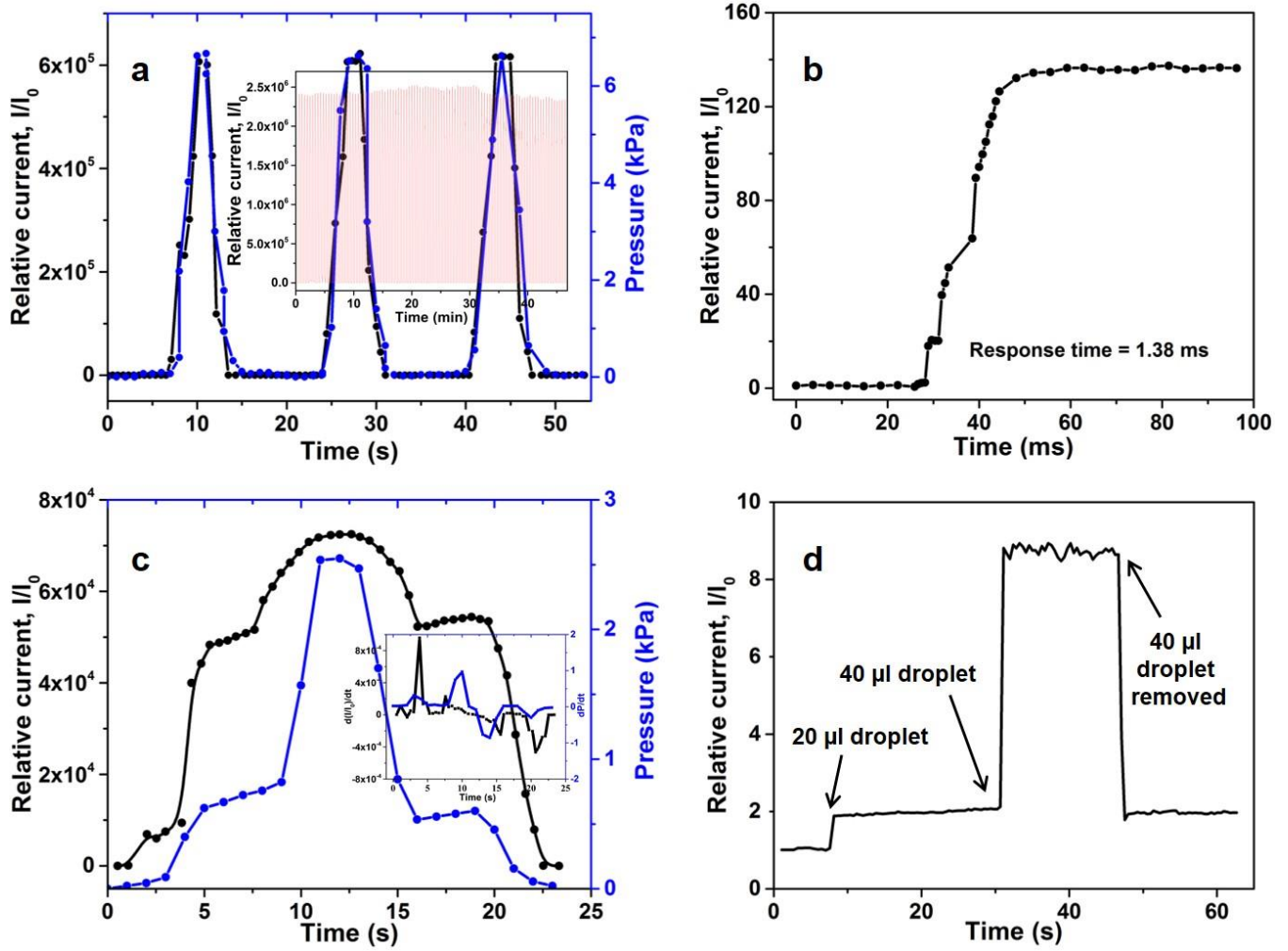
Figure 2.2. Tactile sensing characteristics of the device. (a) The relative current in the sensor increases more than 5 orders of magnitude on increasing the base pressure to ~ 6.5 kPa. The response from the device is robust as seen in the inset, where over 100 pressure cycles of 10 kPa are applied. (b) The device responds in less than 2 ms on being subjected to a 0.01 kPa step increase in load. (c) The device responds in step to both positive and negative changes in the pressure stimuli. The inset shows that the derivative of the response tracks that of the applied stimuli. (d) The device is sensitive to pressure changes due to placement of small water droplets. Both the initial placement of the droplet and subsequently another one were detected. The device also tracks the removal of one of the droplets.

To develop a better understanding of the hierarchical structure, its response is modelled as a power law given by:[97]

$$I_r = I_0 + A \times P^\alpha \tag{2.1}$$

where P is the applied pressure in kPa above the base pressure (arising from the weight of the device), I_r is the relative current, I_0 is the relative current at the base pressure (is hence equal to ~ 1). A is a measure of the

conductance of the structures which is affected by both, their inherent conductivity based on composition (in this case ZnO) and their morphology which will affect the change in the density of conduction pathways with pressure. α is dependent on the structure of the template. The product A×α is a measure of overall tactile sensing performance of the device and α also affects the dynamic range of response. A higher α will lead to a greater dynamic range.

We observe that the power law model accurately fits the response from the sheet-rod device as seen in Fig. 2.3a. The basis for the power law can be described similar to the percolation effects in which the conductance scales with the power of the concentration of the conductive filler (in the insulating matrix), as this increases the conduction pathways.[97,102] In this tactile sensor, the increase in pressure leads to greater interpenetration (and bending) between the nanostructures which increases the density of the pathways available for electrical conduction. There are two distinct effects in this structured device compared to a flat configuration that result in the observed performance, First, the structuring by the ZnO sheets provides discreet contact points between the two electrode surfaces. This concentrates the applied pressure and with increasing pressure will lead to a greater overlap between the sheets (both due to interpenetration and bending) making the structure dynamic with pressure. Second, the rods serve to increase the overlap volume for the sheets to make electrical contacts. This is shown in Fig. 2.3b, with just sheets there has to be direct contact between them for conduction. However in presence of rods (~ 400 nm in length), even sheets separated by 800 nm can serve as conduction channels due to contacts between the rods. Increasing pressure will lead to greater interpenetration and bending of the sheets and rods. This will increase the number of rods in contact between adjacent sheets that serve as conduction pathways. The combined effect of the hierarchical structuring leads to the observed high sensitivity and low detection threshold in the device.

To develop a more comprehensive understanding of the relationship between the device structure and its performance, tactile sensors with different morphologies were characterized and their response was fit to the power law model, Fig. 2.3c-g. The parameters, A, α, and the measure of the overall performance (A×α), at P =1 kPa for the samples are reported in Table 2.1. The complete plots of sensitivity for all the device structures, as calculated

from their response are shown in Fig. 2.3h. Four distinct ranges of behaviors are observed. The device consisting of an ITO coated flat top electrode with a sheet-rod structure as the bottom electrode has the least sensitivity and the smallest A (~ 17). The next set of devices consisting of only a single type of structuring on both the electrodes, either nanosheets or rods, show very similar behaviours with an increase in A and sensitivity (by 3-10 times) compared to the flat electrode configuration. The next sets of devices consist of hierarchical structures (nanosheet-rods) on one electrode and a single type of structuring (nanosheets or rods) on the other electrode. The presence of the hierarchically structured electrode further increases the sensitivity (by ~ 2-8 times) and A (by ~ 5 times) in these devices. The highest sensitivity and A are achieved with the device that has hierarchically structuring on both electrodes. The results in A and the sensitivity show that structuring leads to a significant enhancement in tactile sensing due to formation of specific contact points and dynamic modulation of the conduction pathways due to interpenetration and bending of the structures (both sheets and rods). Similar to the ridges on the finger, the presence of structuring will intensify the applied pressure at the contact points, as has been shown with other micro structures.[26,103] Based on the density of sheets in hierarchical structures, the contact area between the two electrodes is reduced by ~ 85-90 % (see Appendix) increasing the pressure experienced by the sheets edges by 7-9 times. A significant improvement also results from the fact that the sheet structures are randomly oriented, as a result when the two substrates are placed in contact only a small fraction of sheet edges will make contact, significantly increasing the effective pressure (see Appendix). The formation of hierarchical structures further improves the device characteristics, as the effective volume for making contacts is increased due to the presence of rods on the sheets. Further in these structures, a single rod on one sheet can also form multi-point contacts (that change with applied pressure) with rods on adjacent sheets, significantly increasing the density of conduction pathways compared to single point contacts.
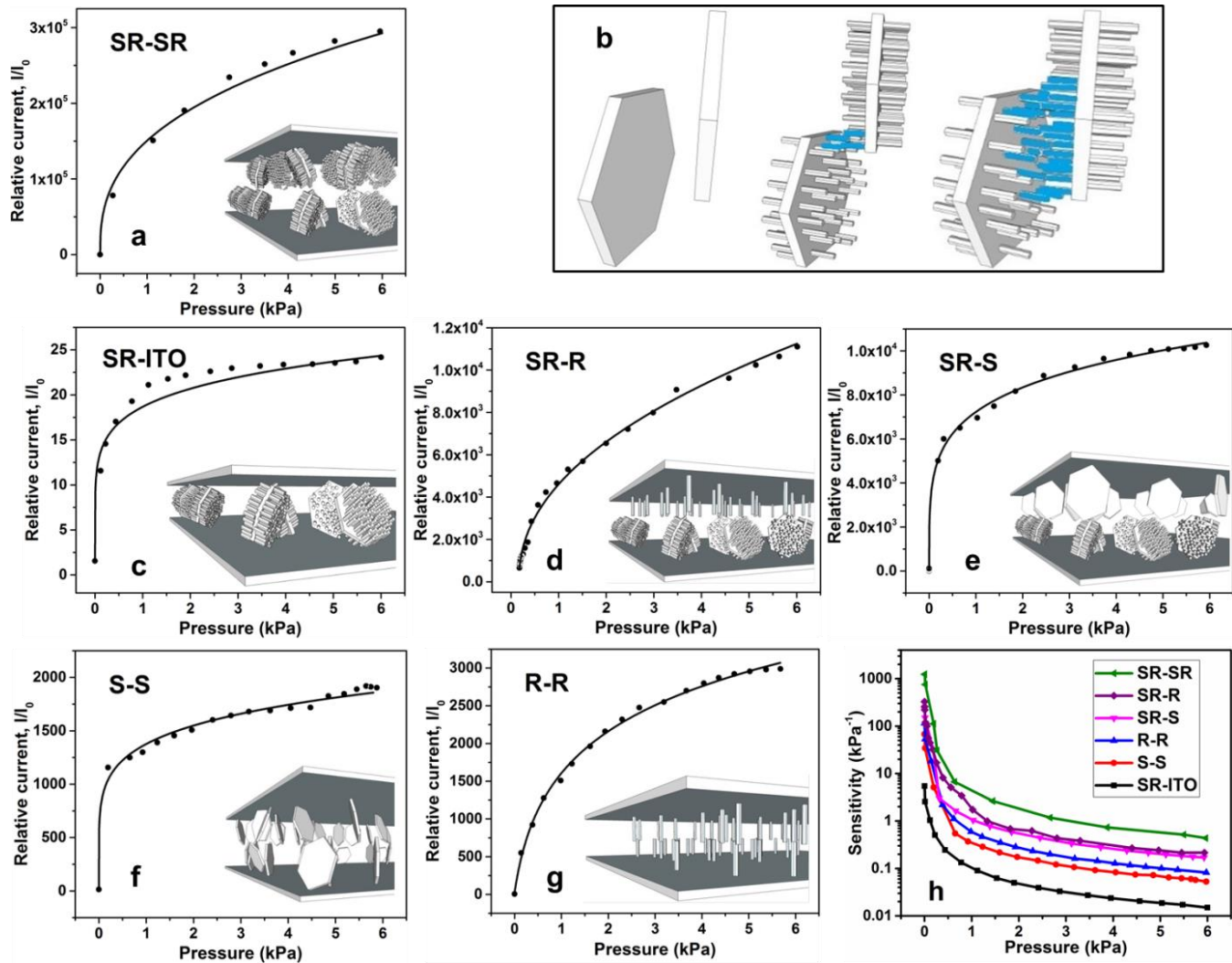
Figure 2.3. The effect of the structure morphology on the response and sensitivity of the sensor is illustrated for 6 different cases. The response from all the structures can be accurately modelled by a power law relation. The lines are the fit from the power law to the data points. (a) The SR-SR (hierarchical nanostructure-hierarchical nanostructure) structure has the highest sensitivity due to its hierarchical nature. (b) The higher sensitivity in this hierarchical structure results from its greater interaction volume and its variation with pressure compared to just the sheet structure. The response from devices made with the following morphology: (c) SR-ITO (hierarchical nanostructure-flat), (d) SR-R (hierarchical nanostructure-nanorods), (e) SR-S (hierarchical nanostructure-nanosheets), (f) S-S (nanosheets-nanosheets) and (g) R-R (nanorods-nanorods). (h) The sensitivity of all the devices, as calculated from their pressure response, shows a progressive increase with greater structuring.

Table 2.1. The value of the parameters for the power law in equation 2.1 used for modelling the response from all the different morphologies of the sensors. The model illustrates that increase in the level of structuring leads to higher sensitivity and also improves the dynamic range of the device.

Sensing materials	A (Pa$^{-\alpha}$)	α	A$\times\alpha$
3-D ZnO nanostructure and ITO (SR-ITO)	17.67	0.155	2.74
2-D ZnO nanosheets and 2-D ZnO nanosheets (S-S)	1362.35	0.172	234.32
1-D ZnO nanorods and 1-D ZnO nanorods (R-R)	1564.65	0.219	342.66
3-D ZnO nanostructure and 2-D ZnO nanosheets (SR-S)	6970	0.247	1721.60
3-D ZnO nanostructure and 1-D ZnO nanorods (SR-R)	5002	0.459	2295.92
3-D ZnO nanostructure and 3-D ZnO nanostructure (SR-SR)	150545	0.595	89574.28

Table 2.2. Comparison of reported tactile sensors with various structures.

Structure	Materials	Methods	Sensitivity (kPa^{-1})	Limit of detection (Pa)	Ref.
Hierarchical	ZnO nanostructures	Electrochemistry	1200-0.5	0.4	This work
Non-hierarchical	CNTs/Ecoflex/ PDMS	Spray coating	0.23×10^{-3}	50000	[95]
Non-hierarchical	Microstructured PDMS	Photolithography	0.15-0.55	-	[103]
Non-hierarchical	Laser-scribed graphene	Laser scribing	0.005-0.96	5000	[104]
Non-hierarchical	SWNT/PDMS	Lithography	1.8	0.6	[90]
Hierarchical	ZnO nanowires/PDMS	Photolithography	6.8	0.6	[20]
Hierarchical	CNT microyarn/ Ecoflex/PDMS	Dry CVD	0.5×10^{-3}	0.4	[105]

Combining pressure sensing with the ability to also detect temperature changes will bring electronic skin devices closer to functional capabilities of human skin. Two stimuli can be deciphered in a single sensor based on its differential sensitivity, as has been reported for decoupling shear and normal stresses in tactile sensor.[31] ZnO has a temperature sensitive response in conductivity due to its semiconducting properties and adsorption of gas molecules on surface.[38,106,107] The basis of temperature sensing is hence based on the material characteristics of the device rather than its hierarchical structure. The human perception of temperature is highly non-linear and is based

on the surface being perceived as cool, warm, hot and cold.[99,100] As a result varying degree of ease, from comfort to slight discomfort and to even pain, is perceived due to the magnitude of the temperature stimuli. The response of the hierarchical sensor to temperature is shown in Fig. 2.4a. A non-linear response is observed and the sensitivity increases with temperature, this will aid the rapid sensing of hot surfaces. Such a response similar to skin is better suited to decipher between varying degrees of temperature stimuli. As seen in Fig. 2.4b, the sensor is able to differentiate between water droplets (10 µl each) of room temperature and 50 °C. The pressure response to the two droplets is similar and can be observed in the initial spike (within 1 s) that results from dropping of the droplet on the sensor. For the droplet at 50 °C, a subsequent slow increase (~ 4-5 s) in current is observed due to the propagation of the temperature stimulus. After reaching a peak in current, a prolonged period of slow decrease in current is observed due to the cooling of the droplet to ambient temperature. To further confirm the proposed heat/energy transfer between the 50 °C water droplet and the tactie sensor, the energy required for the amplifying the current is compared with the energy release of the water droplet when cooling to ambient temperature. Under a constant power supply of 0.5 V, the absolute current change of 10 nA for a period of 10 s requires a minimum energy of 50 nJ, while the 10 µl water droplet could release approxiamte 1 mJ in energy with a temperature change of 30 °C. Such a energy difference suggests a high probability of attributing the observed current response to heat transfer between the droplet and the tactile sensor.

The sensitivity of the device to pressure is in the range of 1200-0.5 kPa^{-1}, while for temperature (298-388 K) it is in the range of 0.016-0.091 K^{-1}. This significant difference combined with the difference in response time allows the detection of both pressure and temperature stimuli. The difference in response time is also due to the faster propagation of a stress stimuli compared to a thermal stimuli based on the velocity of elastic waves in solids and the Fourier law of heat conduction.
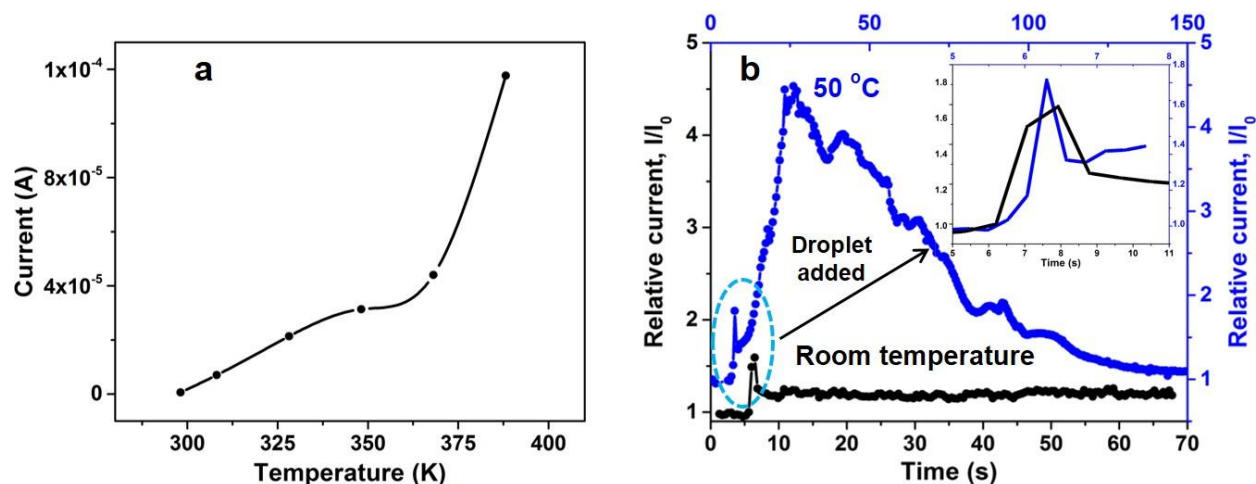
Figure 2.4. The temperature sensing ability of the device due to its ZnO structure. (a) The current across the device at a constant bias of 0.5 V under a base pressure increases monotonically within the temperature range of 298-400 K, as relevant for human skin. (b) The device is able to differentiate between two 10 µl size droplets of 298 and 323 K that are dropped on its surface. The inset shows a magnified view of this initial response.

The hierarchical sheet-rod structures are also a high surface area template. This effect is utilized for making a pseudo-capacitor by electro-depositing a thin conformal layer of MnO_2 (FESEM image of Fig. 2.5a). This pseudo capacitor structure has a pure areal capacitance of 38.7 mF cm^{-2}, which is over an order of magnitude higher than a similar capacitor made on a flat ITO (Fig. 2.5b). The structure is not a multi-layer and hence this value is considered as pure areal capacitance. Further if we convert this areal capacitance to volumetric capacitance the values will be greatly increased (~ 100 F cm^{-3}). However, similar to reporting areal capacitance for multilayer structures this is not an effective approach. The effect of the hierarchical structuring is illustrated in the cyclic voltammetry and galvanostatic charge discharge curves of Fig. 2.5b,c. We observe that the capacitance increases progressively on structuring with rods, sheets with the maximum being for the sheets-rods hierarchical assembly compared to a planar substrate. The Ragone plots of Fig. 2.5d also show that the energy density of the hierarchical structure is improved by an order of magnitude over the planar capacitor. The complete structure of the capacitor is made by electrochemical deposition without the use of any patterning process or the use of metal foam.
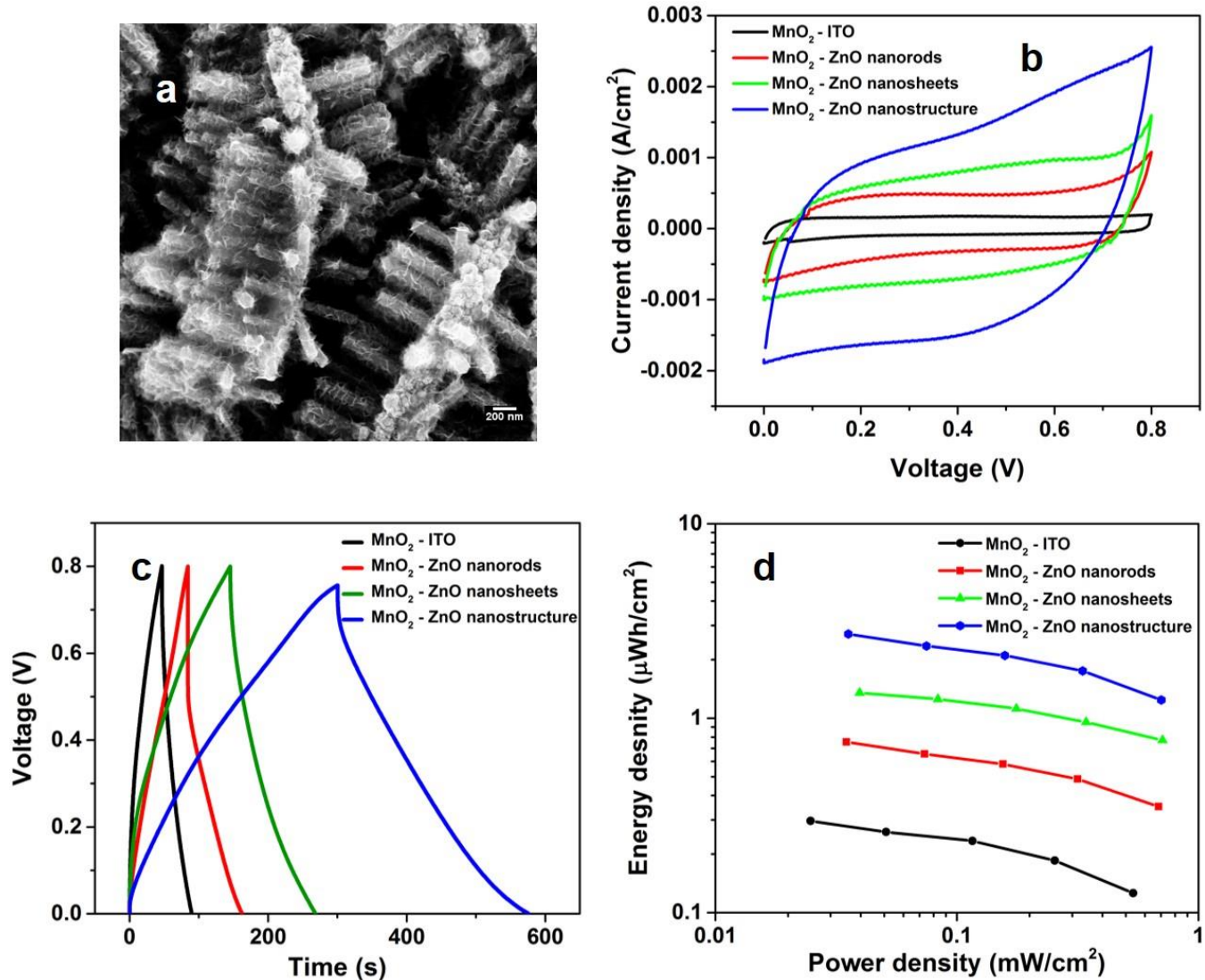
Figure 2.5. The hierarchical structure leads of a more than one order of magnitude increase in the energy storage capacity of a pseudocapacitor made with MnO_2, compared to a flat morphology. (a) In the FESEM image, the conformal coating of the MnO_2 on the nanosheet-rod structure is clearly visible. (b) CV at 50 mV s^{-1} scan rate, and (c) Galvanostatic charge-discharge curves of the different structures showing the effect of morphology. (d) The Ragone plots show the better performance of the hierarchical structure in both energy and power density.

2.4 Summary

In summary, high density hierarchical structures without any underlying pattern are used for making an interlocked, high surface area tactile device. The morphology of the structure consisting of interpenetrating ZnO 2-D sheets with 1-D rods on them serving as interconnects leads to a highly sensitive and dynamic modulation of the conductive pathways with pressure. While structuring with a single nanostructure leads to improvement in device performance, combining multiple structures in a rational way leads a significant enhancement in the device properties. The temperature sensitivity of the device is based on the properties of ZnO. The ability to sense both pressure and temperature in a single device structure with a simple fabrication procedure will bring the electronic tactile devices closer to human skin ability and at the same time make them easily accessible. The hierarchical structure presented here can also be of significance for applications in adhesives, hydrophobic surfaces and also sensing of shear stresses. Other rational combinations of nanomaterials such as 0-D on 2-D sheets or use of other morphologies such as nano-prisms can further lead to enhancement of specific properties such as array of electrodes with high electric fields[108] which will be of significance for application in electrochemical devices and sensing.

Chapter 3

A Light Harvesting, Self-Powered Monolith Tactile Sensor Based on Electric Field Induced Effects in MAPbI₃ Perovskite

3.1 Introduction

The development of material and device configurations that combine sensing and continuous energy harvesting for self-powering in a single structure significantly simplify their use by eliminating the need to develop and wire up external power sources for their operation. It also improves the seamless interfacing of such devices and sensors with the environment to act as media for information collection to drive robotics and human-artificial intelligence interactions. The challenge in such systems is to decouple the sensing of the stimuli from the energy harvesting mechanism to ensure their continuous operation irrespective of the applied stimuli and also the ability to sense both static and dynamic signals in the stimuli.[19,109–113] This has to be done while keeping the device architecture simple for ease of manufacturing and cost effectiveness. In this aspect, organolead trihalide perovskites materials, specifically methylammonium lead iodide ($MAPbI_3$) (and its other analogs such as $MAPbBr_3$ and inorganic analogs such as $CsPbI_3$), have multiple characteristics that have led to their widespread application in development of high efficiency, cost-effective solar cells and optoelectronic devices.[114–117] Recently, specifically $MAPbI_3$ has been reported as a semiconducting ferroelectric material.[118–120] Using this combination of ferroelectric and semiconducting properties in $MAPbI_3$, we demonstrate a solar powered tactile sensor by interfacing it with a nanostructured ZnO layer that acts as a pressure sensitive electron extraction layer.[121] The device has a monolith structure [122,123] while separating the energy harvesting from sensing mechanism and hence is able to sense both static and dynamic pressure stimuli.[112,113] Once poled, the device is operable for at least 72 h with just light illumination over the entire visible spectrum. The device has a pressure sensitivity of 0.57 kPa^{-1} (which is better than most of the reported transistor-based sensors), with a current density of 0.2 mA cm^{-2}. The device also has a linear response till 76 kPa, with minimum pressure sensing ability of 0.5 kPa. The linear response of the device

combined with the ease of manufacturing and being capable of power with just ambient light presents a significant advantage that could greatly simplify the application of the device as part of continuous monitoring systems for information collection.

Besides being a semiconducting ferroelectric material, MAPbI$_3$ also has ion migration effects that have been proposed to lead to the formation of reversible p-n (or p-i-n) type of structures, resulting in switchable photovoltaic effect and the anomalous photovoltaic effects (ion migration effects).[124–126] Both the ion migration effects and the ferroelectric property of MAPbI$_3$ have been reported in literature separately as distinct features of these materials.[118,119,124,125] The origin of each phenomenon is distinct, but both depend on the electric field induced changes to the material, and understanding their combined dynamics is critical to the application of these MAPbI$_3$ materials (and its analogs) in optoelectronics and to further develop it for new and improved devices. It has been proposed that ion migration (MA$^+$ and I$^-$ predominately) in MAPbI$_3$ leads to the formation of MA$^+$-rich regions (n-type) and I$^-$-rich regions (p-type), generating internal p-n junctions that aid the separation of photogenerated electron-hole pairs and hence lead to an observed anomalous photovoltaic effect.[125-127] Similarly, the tetragonal phase (stable at room temperature (RT) and till 327 K) of MAPbI$_3$ has been reported to be ferroelectric due to the light-induced ordering of polar organic cations,[128,129] MA$^+$ in MAPbI$_3$, which results in an internal electrical field originating from electrical polarization. The internal polarization developed during poling also aids the separation of the electron-hole pairs and enhances the photovoltaic efficiency of this material.[129–131] Here, we show that using planar MAPbI$_3$ device (lateral structured, Au/perovskite/Au) both of these effects are present simultaneously in MAPbI$_3$, and either can dominate based on the poling conditions. This is also of substantial interest for fabricating hybrid energy harvesting devices.[132–134] Specifically, our results show that poling done under N$_2$ atmosphere and in dark leads to domination of the proposed ion migration effects, while poling done under illumination and in an ambient atmosphere (with the presence of O$_2$) leads to ferroelectric domination. The distinction between the two effects is based on the reversal of the sign in the open-circuit voltage (V_{OC}) and the observed short-circuit current density (J_{SC}). To further ascertain the dominance of each effect, corroboration is done by studying the effect of

polarized light and phase transition from tetragonal to cubic on the poled samples. We further observe that the ferroelectric characteristics lead to a more sustained response. The J_{SC} in these devices is limited due to the high internal DC resistance of the perovskite layer. Using this limitation and the developed understanding of the ferroelectric-semiconducting properties of MAPbI$_3$, our reported tactile sensor is made by interfacing a top electrode of ZnO nanosheets with the perovskite layer. These ZnO sheets act as an electron extraction layer[121,135,136] and enhance the J_{SC} in a dynamic fashion, due to the load sensitivity of the interaction area between the sheets and the perovskite layer. Unlike other transistor based tactile sensors,[95,137–140] the combination of ferroelectric and semiconducting properties of MAPbI$_3$ allows this device to be operated with just solar/light energy.

3.2 Materials and Methods

3.2.1 Synthesis

3.2.1.1 Preparation of CH_3NH_3I Precursor

Methylammonium iodide (CH_3NH_3I) was synthesized according to a method reported elsewhere.[141] Methylamine (27.8 ml, 33 wt.% in absolute ethanol, Sigma Aldrich) was reacted with hydroiodic acid (30 ml, 57 wt.% in water, Sigma Aldrich) at 0 °C and stirred for 2 h. After stirring for 2 h, dark yellow precipitates were obtained by evaporating the solvent at 60 °C for 1 h using a rotary evaporator. The solid product was washed with diethyl ether and recrystallized from anhydrous ethanol. The resulting white precipitate was dried overnight under vacuum at 60 °C.

3.2.1.2 $MAPbI_3$ Film Preparation on Gold Chips

For lateral $MAPbI_3$ device, gold (Au) chips with an electrode spacing of 2 µm were fabricated on the top of 200 nm thick SiO_2 layer by photolithography. Gold chips were washed with Millipore water, and then sonicated in a 1:1 mixture of acetone and isopropanol for 10 minutes, followed by another 10 minutes of sonication in Millipore water. A Piranha solution was used to clean organic matter off the gold substrate. Gold chip was washed thoroughly with Millipore water after being immersed in the piranha solution for 3 minutes. The $MAPbI_3$ film was prepared on the Au chip by using solvent engineering method in one-step spin coating. In particular, 230.5 mg of lead iodide (PbI_2), 79.5 mg of CH_3NH_3I, and 39 mg of Dimethyl sulfoxide (DMSO) were mixed in 300 mg of Dimethylformamide (DMF) solution at room temperature with stirring for 1 h in order to prepare a $CH_3NH_3I \cdot PbI_2 \cdot DMSO$ adduct solution. 90 µl of this adduct solution was dropped onto the Au chip and was then spun at 8000 rpm for 30 s. After seven seconds of rotation, 0.7 ml of diethyl ether was slowly dripped onto the center of the Au chip in 10 seconds. The obtained film on the Au chip was heated at 65 °C for 2 min and 100 °C for 3 min.

3.2.1.3 Electrochemical Deposition of ZnO nanosheets

For the growth of ZnO nanosheets, SiO_2 passivated Indium tin oxide (ITO) or Au coated Kapton on one surface with a surface resistivity, R_s = 8-12 Ω/sq was used. ITO was purchased from Delta Technologies was used as a substrate. The electrochemical deposition was carried out using an Ivium CompactStat Electrochemical Analyser with a standard three-electrode setup. A Ag/AgCl electrode was used as the reference electrode, with a platinum wire as the counter electrode and a clean ITO substrate as the working electrode. A mixture of 28 mM $ZnCl_2$ and 0.1 M KCl aqueous solutions was used as the electrolyte. A beaker filled with the electrolyte solution was immersed in a silicone oil bath, which was heated on a hot plate to maintain a steady temperature of 70 °C during the deposition. A constant electric potential of -1.035 V was applied for 1 h. After the deposition, the substrate was washed with Millipore water and then annealed at 335 °C for 1 h in air.

3.2.2 Characterizations

A Zeiss Ultraplus Field-emission Scanning Electron Microscopy (FESEM) equipped with energy dispersive X-ray spectroscopy (EDS) was used to examine the morphologies of $MAPbI_3$ and ZnO nanosheets. The crystal structure was characterized by glancing incidence X-ray diffraction (GIXRD) using a PANalytical X'Pert Pro MRD diffractometer with Cu Kα radiation (λ = 1.54 Å) at an incidence angle of 0.4°. Measurements on the symmetric lateral structure cell configuration were conducted using a probing station. A two probe method was used by connecting one probe to the Au pad on the Au chip and another probe connected to the ground. A Keysight 6614C 50 Watt power supply with a maximum voltage output of 100 V was used for the poling process. The $MAPbI_3$ film was poled at different voltages for 5 min. After poling, the open circuit voltage (V_{OC}) and the short circuit current density (J_{SC}) were measured using a Keysight 3458A Digital multimeter. The film was connected in series with the multimeter and power supply to form a circuit. Electrical poling was done under N_2 atmosphere and in dark condition for the p-n effect, while for ferroelectric effect poling was done under illumination and in ambient atmosphere (with the presence of O_2). V_{OC} and J_{SC} measurements were performed under simulated air mass 1.5

global irradiation (100 mW cm^{-2}); that was generated using a Xenon-lamp based solar simulator (Newport Oriel Instrument 67005, 150 W Solar Simulator). Cyclic voltamettry (CV) measurements were done using an Ivium CompactStat Electrochemical Analyser by connecting one Au pad to working electrode and the other Au pad to counter/reference electrode. A NREL calibrated KG5 silicon reference cell was used to calibrate light intensity in order to minimize spectral mismatch. For nitrogen on test, the films were kept in a steady N$_2$ flow during the poling and measurements to prevent the absorption of oxygen and moisture. The light polarization measurements were carried out at room temperature using a 633 nm laser source, a polarizer, and a wave plate purchased from Newport. The poled MAPbI$_3$ film was illuminated with linearly polarized light to measure the variation of J_{SC} as a function of the light-polarization. UV-Visible absorption spectra were recorded using Perkin Elmer Lambda 750 spectrophotometer. For solar powered tactile sensor, ZnO nanosheets on ITO/Kapton substrate was used as the top sample and Au/MAPbI$_3$/Au lateral structure was used as the bottom sample. First, the MAPbI$_3$ film was poled under 1.0 sun illumination in ambient atmosphere and then the ZnO nanosheets were interfaced with the perovskite layer. Three probes system was used; first probe connected to Au pad, second probe connected to the Au ground electrode on Au chip, and third probe was connected to the ITO/Kapton substrate. An MFA Motorized Miniature Linear Stage was used to apply the load to the samples. A Honeywell Model 31 Miniature Load Cell was connected to the stage for measuring the load. Combined with a micro-pro series digital panel meter, we were able to read out the measurements and record the data.

3.3 Results and Discussion

The schematic in **Figure 3.1**a shows the proposed ion-migration effects in the MAPbI$_3$ film. The resulting internal field (due to the p-n junctions) will lead to separation of the charge carriers (electron-hole pairs) generated on light illumination and the resulting V_{OC} (and J_{SC}) will be of the same polarity as that of the poling field. Figure 3.1b shows that the observed V_{OC} and J_{SC} in the MAPbI$_3$ film when poled under N$_2$ in dark conditions are consistent with the proposed ion migration effects in the perovskite layer. Poling of the MAPbI$_3$ film in air and under light illumination (1.0 sun) leads to polarization of the MAPbI$_3$ film due to its ferroelectric nature (also shown in the schematic of Figure 3.1a). In this case however due to the presence of metal electrode, a charge compensating layer (due to the free electrons in the metal) is formed and the resulting V_{OC} and J_{SC} are of opposite polarity compared to the poling field direction.[130,132] Figure 3.1c shows the observed V_{OC} and J_{SC} are indeed of reverse polarity as compared to the ion migration effects. In case of ion migration, the internal electric field results from the formation of a depletion region in the material. It has been proposed that O$_2$ is adsorbed at the grain boundaries and the defects in MAPbI$_3$ which suppresses the formation of p-n junctions.[125] More detailed studies are required to ascertain the exact behavior based on the charge compensating layer in the metals electrodes and the observed V_{OC} and J_{SC} are consistent with reported experiments using ferroelectric polymers in solar cells.[130,142] Further, the domination of the ferroelectric behavior under poling with illumination is consistent with the observation that orientation of the MA$^+$ ions, which plays a critical role in ferroelectricity, is significantly enhanced under illumination (due to photoexcitation).[128] The reversal of the polarity of the V_{OC} and J_{SC} depending on the poling conditions is critical to the functioning of MAPbI$_3$ (and other similar materials)-based optoelectronic devices.
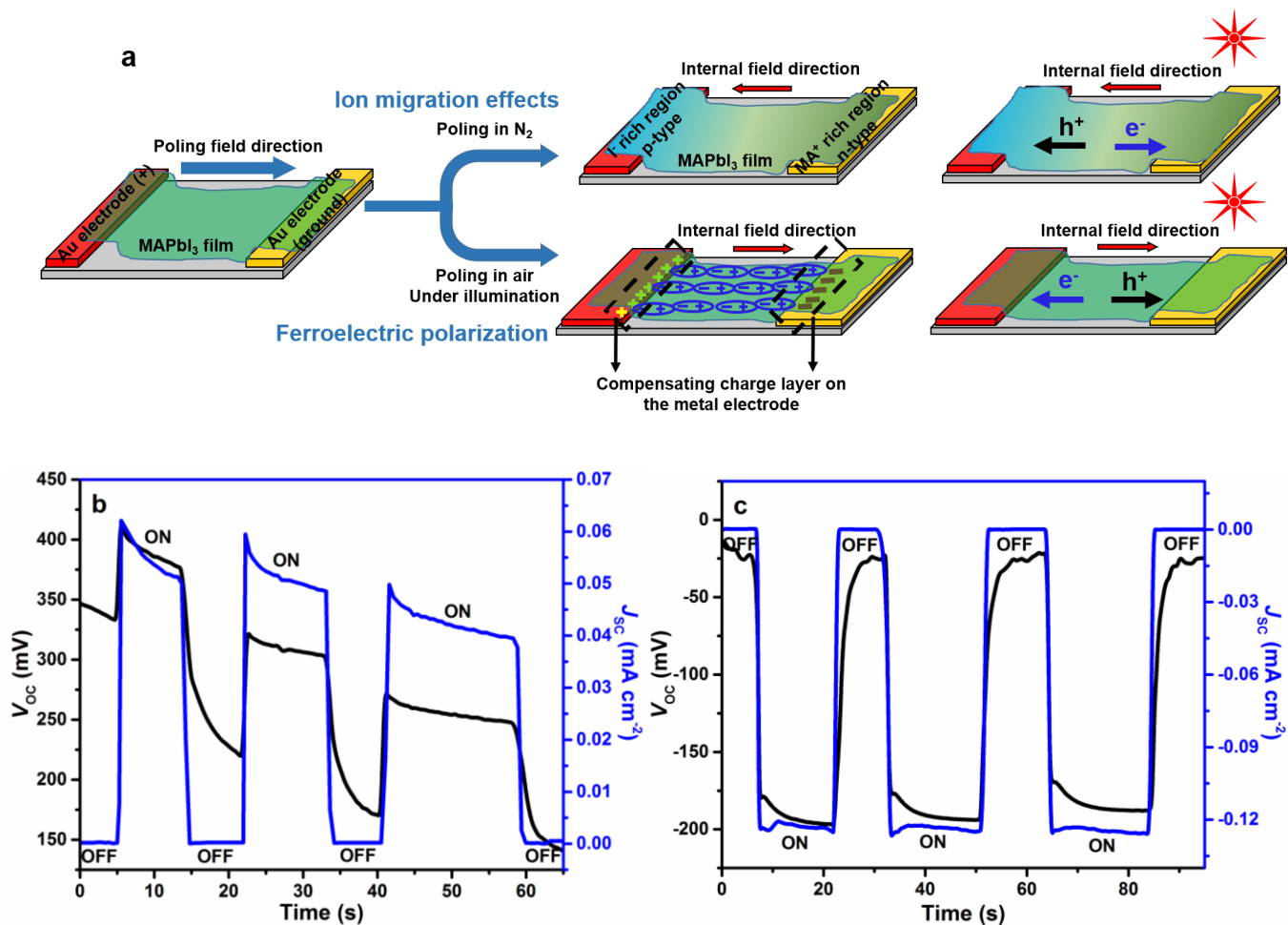
Figure 3.1. Ion migration and ferroelectric effects in Au/MAPbI$_3$/Au device. (a) Schematic showing the proposed ion migration effects (leading to p-n junctions) and ferroelectric polarization in Au/MAPbI$_3$/Au device with reversal of the internal electric field between the two cases. (b) The observed V_{OC} and J_{SC} in the MAPbI$_3$ films poled at 1.5 V μm^{-1} electric field for 5 min under N$_2$ in dark conditions show the ion migration effects, which is consistent with the model in a. (c) When poled at 1.5 V μm^{-1} electric field for 5 min in air under light illumination (1.0 sun) results in ferroelectric polarization and the observed V_{OC} and J_{SC} in the MAPbI$_3$ film are reversed. OFF refers to V_{OC} and J_{SC} measured under dark and ON refers to V_{OC} and J_{SC} measured under 1.0 sun illumination.

The ion migration effect in MAPbI$_3$ films is characterized by poling under an N$_2$ atmosphere in dark. **Figure 3.2** shows the effect of poling field on the V_{OC} and J_{SC} generated in these films due to the ion migration effects. In Figure 3.2a, b, both V_{OC} and J_{SC} show a sustained effect on illumination with 1.0 sun. The effect, however, gradually decreases over the cycles, which is consistent with the rehomogenization of the ions that were diffused due to the poling fields.[125] It should be noted that the poling field strength and time are kept limited to prevent complete

segregation of the ions, which will lead to the formation of PbI_2,[142] and the observed ion migration and ferroelectric behavior disappear (Figures A3.1a-c and A3.2a,b, Appendix). There is no electrode reaction observed during the poling process as confirmed by elemental analysis, in which no migration of element was observed (Figure A3.3, Appendix). Multiple current-voltage (*I-V*) scans done within the voltage range based on the electric field limit and at room temperature show a consistent response from the perovskite layer, which indicates that no degradation of the material is occurring (Figure A3.4, detailed discussion in Appendix). From the FESEM image, we do not observe any change in the material during the controlled poling process under N_2 (Figure A3.1d, Appendix). The V_{OC} increases monotonically with the poling field strength (Figure 3.2c), due to greater ion migration, which increases the strength of the observed effects. However, J_{SC} reaches a maximum and then reduces with poling indicative of higher film resistance. The nonferroelectric nature of this response is further confirmed by illuminating the poled $MAPbI_3$ film with linearly polarized light (using a 17 mW laser of 633 nm). As seen in Figure 3.2d, J_{SC} does not show any appreciable dependence on the relative direction of polarization of the electric field of the incident light and the film's sample plane. It is also known that $MAPbI_3$ undergoes a phase transition from tetragonal (which is ferroelectric) to cubic (which is not ferroelectric) above 327 K (also confirmed by UV-Vis absorption spectroscopy, see Figure A3.5 in Appendix).[144,145] On heating these films to 330 K and poling them, we observe that the both V_{OC} and J_{SC} rather than disappearing increase in magnitude (Figure 3.2e,f). This is consistent with increased ion migration (due to greater mobility) at higher temperatures.[126,143,146] The contribution from ion back-diffusion currents is negligible in these samples under applied conditions. This has been characterized by cyclic voltammetry (CV) using a potentiostat (see Appendix). We observe that the ion diffusion currents, which would lead to a capacitive behavior, are negligible compared to normal electronic currents.[147] Further, no J_{SC} is observed in dark (after poling; Figure A3.6, Appendix) indicating that there is no significant ion back-diffusion occurring. However, with light illumination J_{SC} is observed, attesting to the presence of internal electric filed that leads to separation of the photogenerated electron-hole pairs. Unpoled perovskite samples do not show any J_{SC} in the presence or absence of light illumination (Figure 3.2f). We believe that the absence of any ion back-diffusion

currents can be attributed to a very slow back-diffusion process, which leads to insignificant magnitude of these currents, as indicated by the presence of the J_{SC} (under illumination) even more than 6 h after the poling process in N_2. The stability of the perovskite layer against redox reaction and decomposition to products such as PbI_2 (an insulator) within the voltage and temperatures used in these experiments is also characterized (see details in Appendix). We do not observe any oxidation or reduction evidence from CV scans at room temperatures within the applied voltage magnitudes, rather a consistent current response is observed confirming that the perovskite layer is stable (Figure A3.4a and A3.7, Appendix). At higher temperatures (325 K and 350 K), we observe the evidence of redox reaction occurring from CV scans (Figure A3.7, Appendix). Following this, there is a steep drop in the current response from the sample (more than 80 time; Figure A3.8, Appendix). We believe this is due to redox decomposition of the perovskite to PbI_2, which being an insulator leads to the observed current drop. The FESEM images further confirm this, as a change in morphology and composition is observed only in the elevated temperature samples (Figure A3.9a-c and Table A3.1, Appendix). Following this change, consistent with the decomposition of the perovskite layer, the poling of the device does not lead to any observable V_{OC} or J_{SC}.
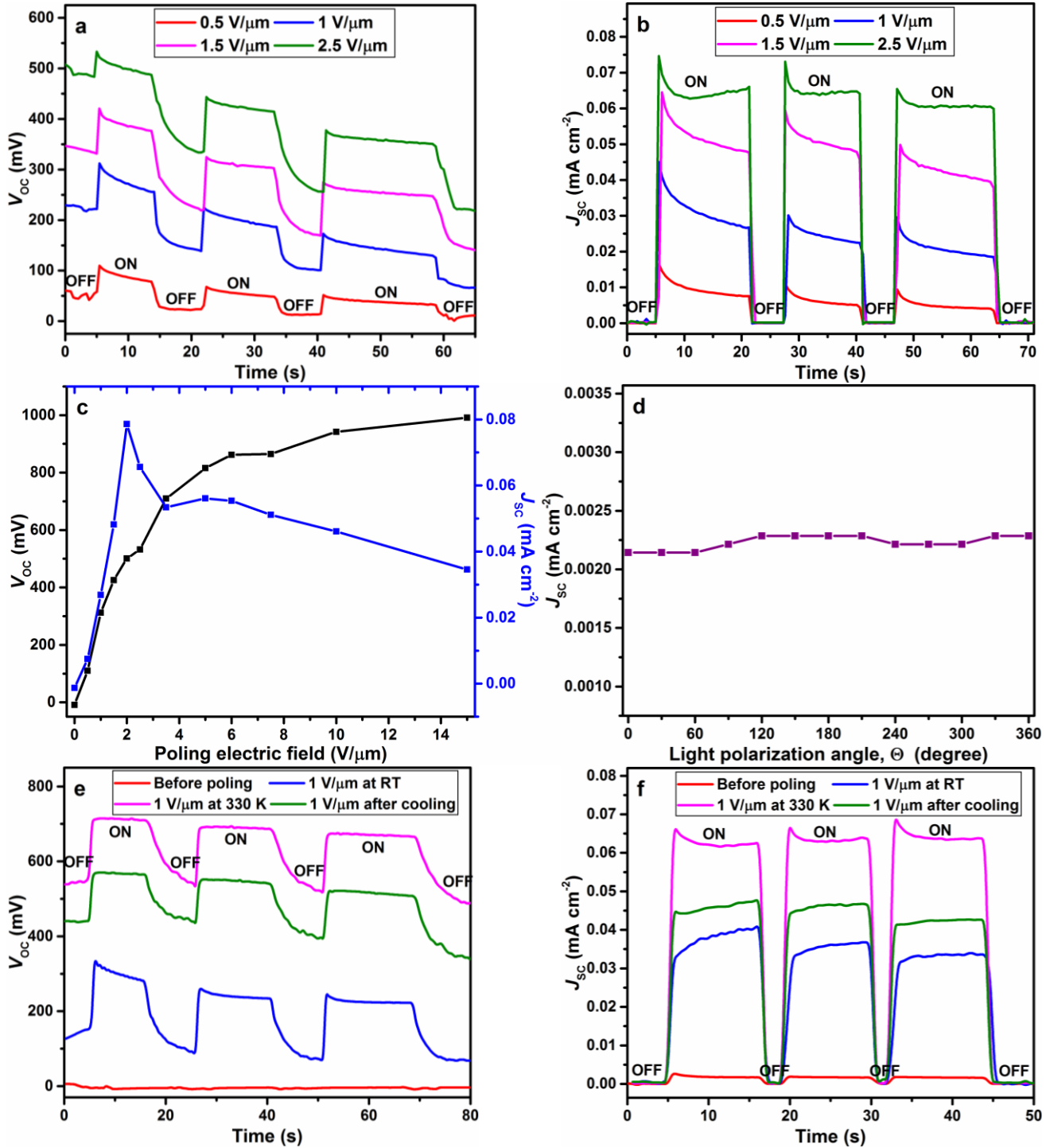
Figure 3.2. Ion migration effect in lateral MAPbI₃ device after poling under N₂ in dark condition. (a) V_{OC} and (b) J_{SC} cycles after 0.5, 1, 1.5, and 2.5 V μm⁻¹ poling for 5 min. (c) V_{OC} and J_{SC} dependence on strength of the poling electric fields, under 1.0 sun illumination. (d) J_{SC} measured as a function of polarization angle (θ) of the linearly polarized light with respect to the film plane after poling the device at 1.5 V μm⁻¹ for 5 min. (e) V_{OC} and (f) J_{SC} of the MAPbI₃ device before poling at RT and after 1 V μm⁻¹ poling for 5 min at RT, 330 K, and after cooling to RT. OFF refers to V_{OC} and J_{SC} measured under dark and ON refers to V_{OC} and J_{SC} measured under 1.0 sun illumination.

The proposed ferroelectric properties of the MAPbI$_3$ films and their effect on generating V_{OC} and J_{SC} were investigated by poling under 1.0 sun illumination and in ambient air conditions. These conditions reflect that light-stimulated ordering of MA$^+$ ions enhances the ferroelectric behavior of MAPbI$_3$, while the presence of O$_2$ will subdue the p-n junction behavior.[125,128] Further, the optical photography shows the transformation of the MAPbI$_3$ films during the controlled poling process (Photo A3.1 and A3.2, Appendix).[143] On reversing the field direction, the observed transformation also reverses its spatial orientation (Photo A3.3, Appendix). Such an effect is not observed optically when poling is conducted under the N$_2$ atmosphere (Photo A3.4, Appendix). Again here also we limit the poling field strength to prevent material decomposition. The V_{OC} and J_{SC} due to ferroelectric polarization are shown in **Figure 3.3**a and b. We observe that both are reversed in direction compared to the proposed ion migration effects, consistent with the model of Figure 3.1a; further, the response is stable with no observable decay in their magnitude. This is crucial as it infers that unlike the diffusion of ions, the polarization due to orientation of the MA$^+$ ions is sustained over longer time. We further confirm the ferroelectric nature of this process by observing (Figure 3.3c) that unlike the ion migration effects J_{SC} has a sinusoidal-like dependence on the angle (θ) between the electric field of the incident polarized light and the sample plane (the in-plane ferroelectric polarization) due to second-order optical effects.[148,149] This dependence has a periodicity of 180° with maximum response observed at $\theta = 0$, when the electric field of the incident light is along the in-plane ferroelectric polarization. By heating the films to 330 K, which leads to phase transition from tetragonal to cubic structure, we observe that both V_{OC} and J_{SC} effects disappear (Figure 3.4a,b), further confirming the proposed ferroelectric characteristic.[119,150] The effects are restored on cooling the film back to room temperatures ($\approx$ 296 K).

Figure 3.3. Ferroelectric effect in lateral MAPbI$_3$ device after poling in air under light illumination. (a) V_{OC} and (b) J_{SC} cycles after 0.5, 1, 1.5, and 2.5 V µm^{-1} poling for 5 min. (c) J_{SC} measured as a function of polarization angle (θ) of the linearly polarized light with respect to the film plane after poling the device at 1.5 V µm^{-1} for 5 min. OFF refers to V_{OC} and J_{SC} measured under dark and ON refers to V_{OC} and J_{SC} measured under 1.0 sun illumination.
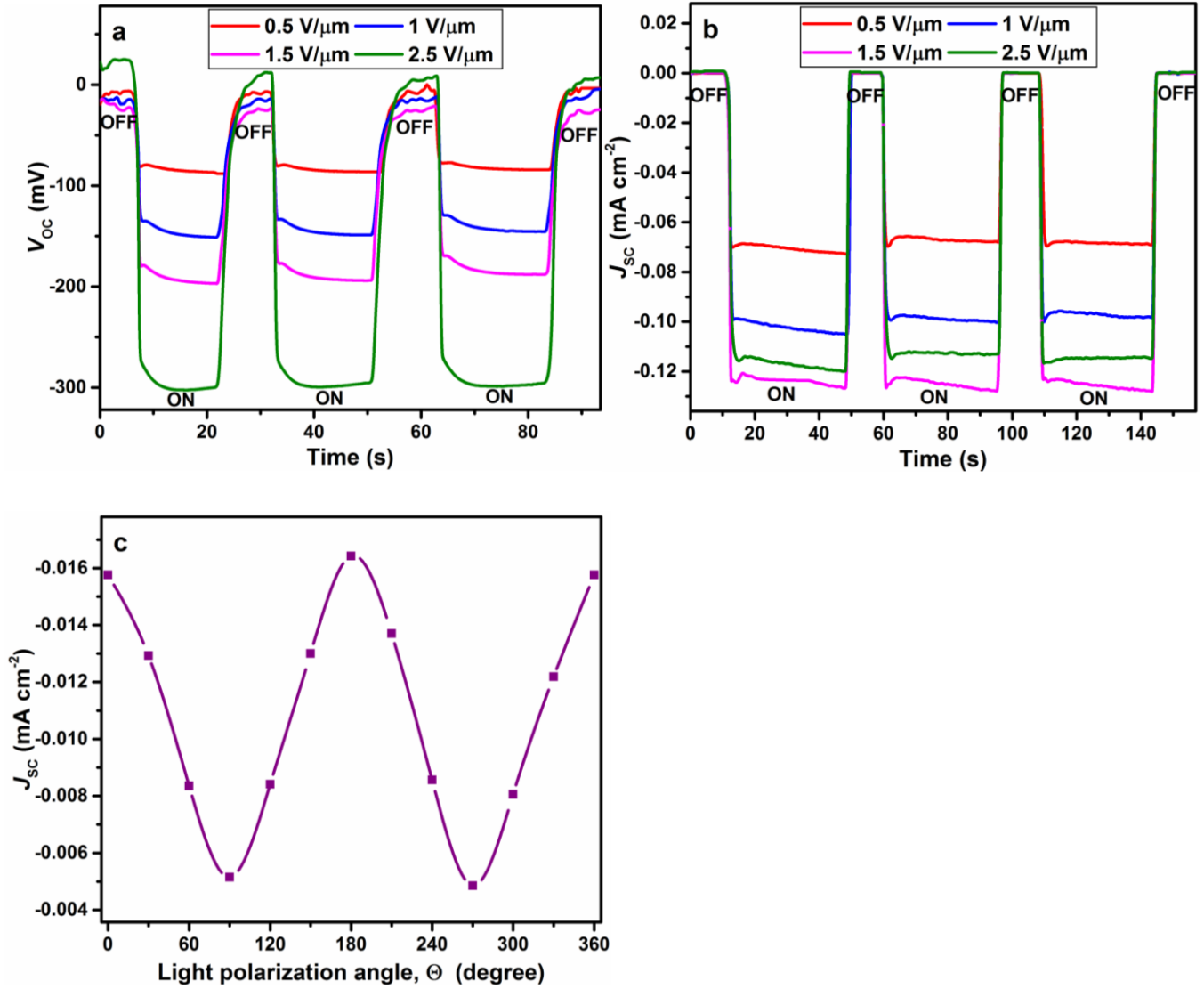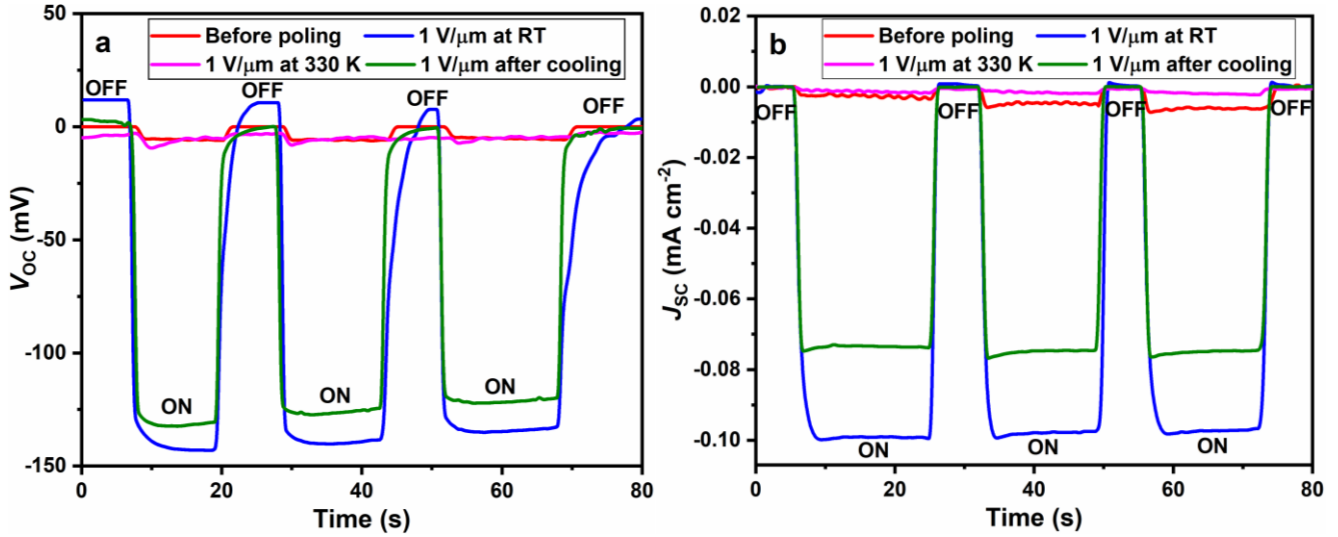
Figure 3.4. Ferroelectric effect in lateral MAPbI$_3$ device after poling in air under light illumination. (a) V_{OC} and (b) J_{SC} of the MAPbI$_3$ device before poling at RT and after 1 V μm^{-1} poling for 5 min at RT, 330 K, and after cooling to RT. OFF refers to V_{OC} and J_{SC} measured under dark and ON refers to V_{OC} and J_{SC} measured under 1.0 sun illumination.

Knowing the conditions for domination by the ferroelectric behavior, we now demonstrate a light/solar-powered tactile sensor. The MAPbI$_3$ films are poled at 0.5-1.5 V μm^{-1} in air for 5 min in these studies. The basic schematic of the sensor is presented in **Figure 3.5**a. Specifically we interface the MAPbI$_3$ film with microstructured ZnO sheets acting as a dynamic drain electrode for electron extraction. The inset of Figure 3.5a shows a FESEM image of the cross section of the device, where ZnO sheets are in direct contact with the perovskite in Figure A3.10 in Appendix). Such an electron extraction layer is required for MAPbI$_3$ films to improve their photocurrent efficiency since holes are extracted efficiently from them compared to electrons.[151] The V_{OC} generated due to ferroelectric polarization is on the order of hundreds of mV, but J_{SC} is limited to very small values of ≈ 0.1 mA cm^{-2} due to large DC resistance of these materials[118,145] and also the large path lengths that the charge carries must diffuse to reach the electrodes (on the scale of 2 - 20 µm). By interfacing ZnO sheets across the surface of the MAPbI$_3$ film, the generated charge carries (due to illumination) will separate under the polarization field and the photoelectrons should be easily collected by these sheets leading to increased J_{SC}. The band structure of the ZnO is suited for acting as an electron collector from the perovskite layer (Figure A3.11, Appendix). The ZnO sheets are

38

vertically oriented and hence have a limited area of interaction with the perovskite layer (inset of Figure 3.5a). On application of a pressure, the ZnO sheets will easily bend compared to the MAPbI$_3$ film, which is planar.[20,152] The bending of the ZnO sheets will effectively increase their interfacing area with the MAPbI$_3$ film leading to a higher charge collection and hence a pressure sensitive modulation in J_{SC} will be observed. Figure 3.5b shows that the device does indeed works as a pressure sensor and the observed J_{SC} is in step with the modulation of the applied pressure. A clear correspondence is seen in the plot of Figure 3.5c, which plots the derivative of the pressure and J_{SC} responses with respect to time. A more controlled response is shown in Figure 3.5d to pressure cycles of different magnitude and in Figure 3.5e to pressure cycles at different speeds. Both these responses show that the J_{SC} is critically dependent on bending of the ZnO sheets due to the applied pressure and the sheets are effective in their role as a dynamic drain. In the linear response range, the maximum load sensing ability of the device is 76 kPa with minimum detection of 0.5 kPa, as seen in the inset of Figure 3.5f. The linearity in response is a critical advantage for sensors to relate their measured signal to the applied stimuli. The device also shows a consistent response over 100 load cycles signifying a reliable response (Figure 3.5g). We also observe (Figure 3.5f) that the sensitivity of the device increases with the strength of the electric field used to pole the MAPbI$_3$ films. This is in line with a more effective charge separation at higher polarization of the MAPbI$_3$ films, which will improve their collection efficiency by the ZnO films making the device more sensitive to pressure modulations. The sensitivity of 0.57 kPa^{-1} observed at poling fields of 1.5 V µm^{-1} is higher than those of other tactile sensors that have been reported with a linear response as shown in Table 3.1.[26,90,91,95,105,137–138,153–155] This device also, however, does not require an active power source for operation and once poled can easily function for more than 72 h. (see Figure 3.5h) by using light/solar illumination. This limit is based on 30% decrease in the base J_{SC} (at base pressure), which relates to loss of poling (Figure A3.12, Appendix). The failure of the device occurs at pressures exceeding 500 kPa, at which the ZnO sheets fracture (Figure A3.13, Appendix). The perovskite/ZnO device is stable for more than 5 days and shows no degradation of the MAPbI$_3$ layer, which bare exposed MAPbI$_3$ degrades within a day (Figure A3.14, Appendix).

The presence of the top ZnO layer, which is also hydrophobic, minimizes direct contact of the MAPbI$_3$ layer to ambient oxygen and moisture enhancing its stability (Figure A3.15, Appendix).

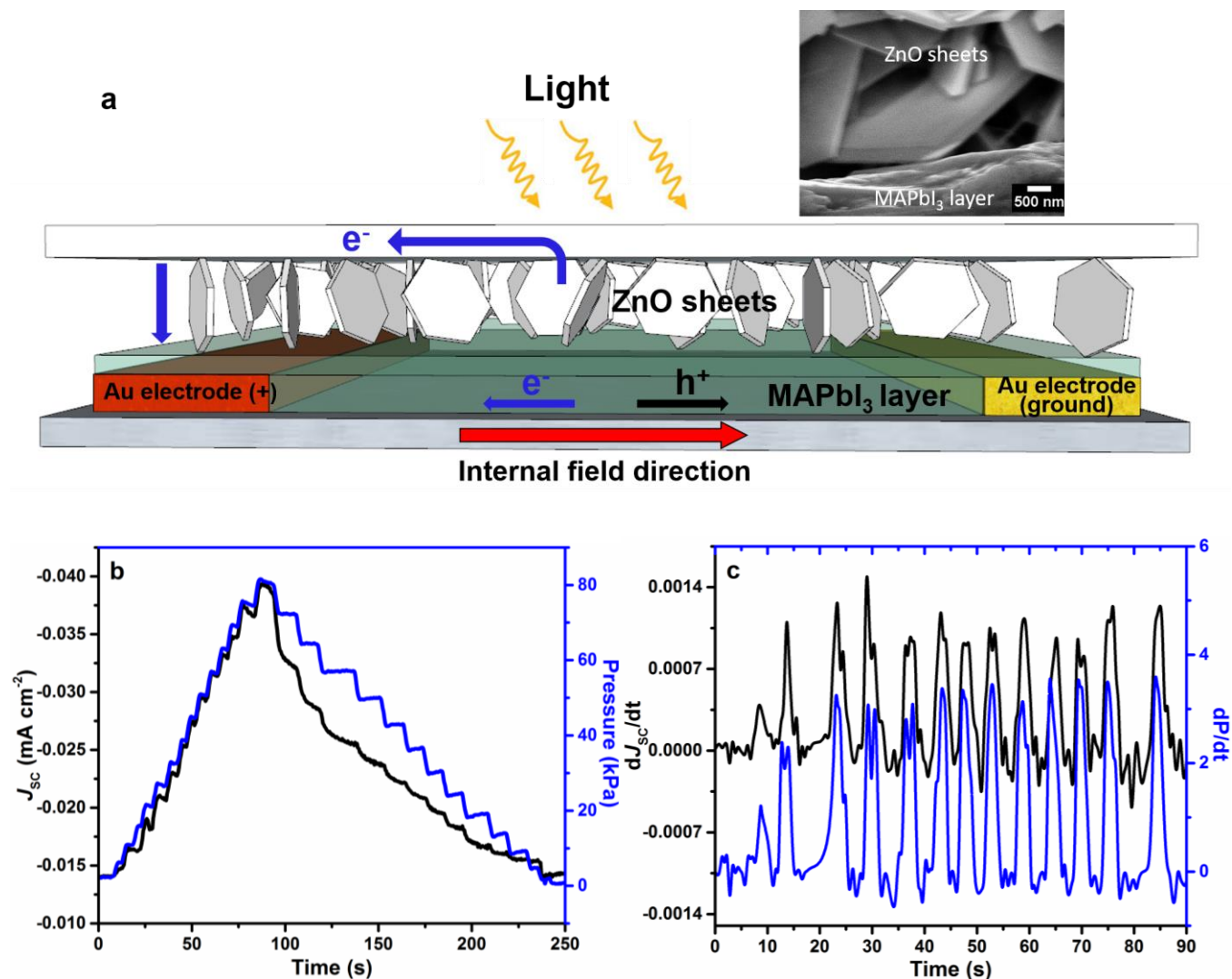**Figure 3.5A.** Characterization of a solar powered tactile sensor. (a) Schematic of the solar-powered tactile sensor where ZnO sheets are interfaced with the MAPbI$_3$ channel/film. (b) J_{SC} is in step with the modulation of the applied pressure after 0.5 V μm^{-1} poling for 5 min in air under 1.0 sun illumination. (c) The derivative of the response tracks that of the applied pressure stimuli with accuracy.
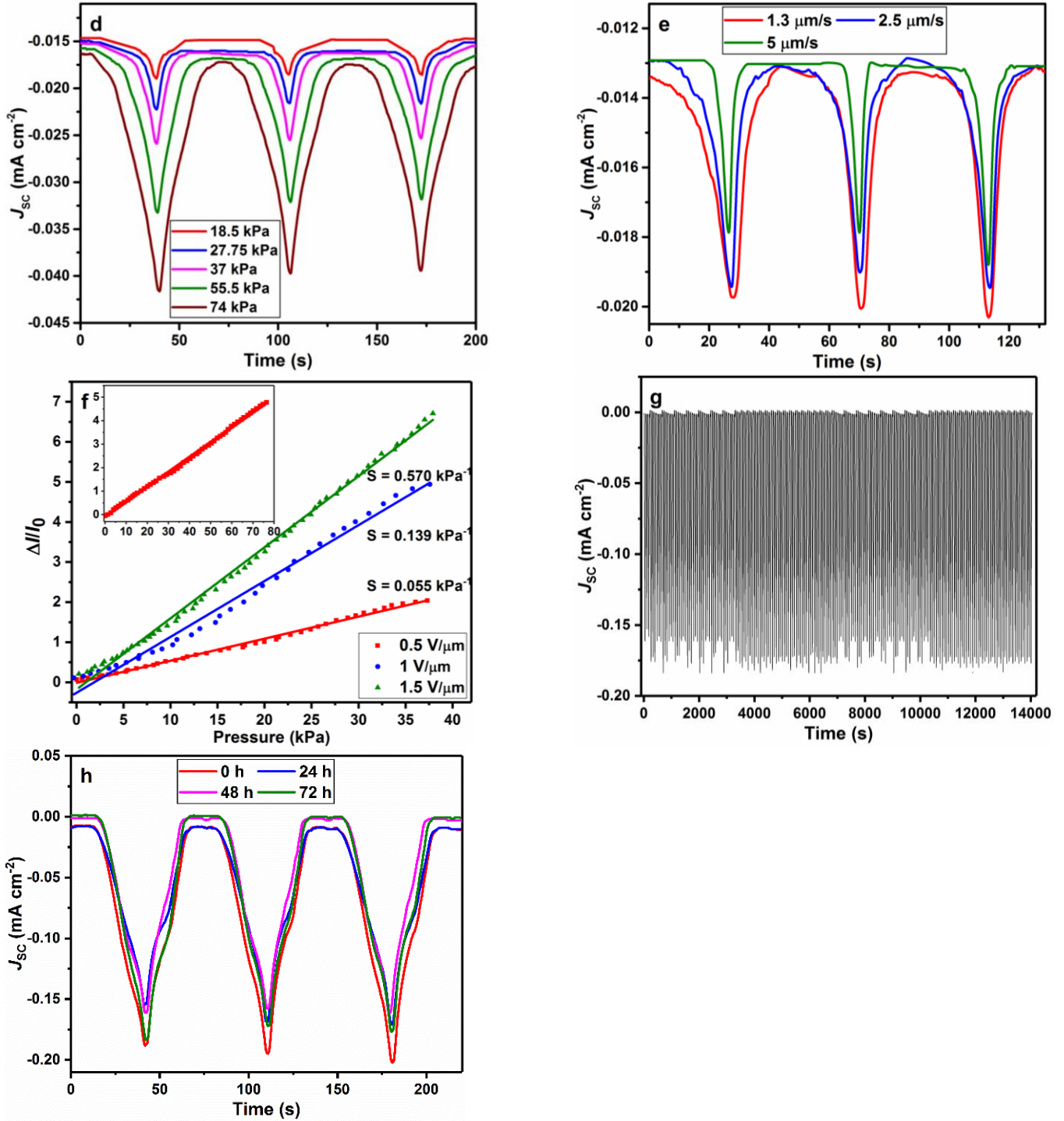
Figure 3.5B. (d) J_{SC} cycles as a function of different pressures show the reproducibility of the device. (e) J_{SC} cycles as a function of different speeds with a maximum 37 kPa pressure show that the sensor responds with little delay to the stimuli. (f) The sensitivity of the device increases with the strength of the poling electric fields. Inset shows the device has a linear response with a maximum load detection of 76 kPa and minimum detection limit is 0.5 kPa. (g) Consistent response is observed over 100 load cycles of 37 kPa. (h) J_{SC} response to load cycles of 37 kPa is maintained over 72 h in the device after initial poling at 1.5 V μm^{-1} for 5 min.

Table 3.1. Summary of materials used, operating voltage, power density, sensitivity, limit of detection, and linearity of different tactile sensors.

| Sensor type	Materials	Operating voltage /Power density	Pressure Sensitivity	Limit of Detection (kPa)	Linearity	Ref.
Transistor	ZnO nanosheets/ MAPbI$_3$	Solar driven	0.57 kPa^{-1}	0.5	Linear (0-76 kPa)	This work
Transistor	Graphene/ion gel	< 2 V/ 0.015 mWcm^{-2}	0.12 kPa^{-1}	5	Linear (0-40 kPa)	[105]
Transistor	Cu/PVDF-TrFE matrix	15 V/10.45 mWcm^{-2}	0.67×10^{-3} kPa^{-1}	200	Linear	[153]
Transistor	ITO/Au/ micropatterned PDMS/PiI2T-Si	100 V	0.38-8.4 kPa^{-1}	-	Non-linear (0-55 kPa)	[154]
Transistor	Ge/Si NW-array	3 V/0.022 mWcm^{-2}	11.5 µS kPa^{-1}	≈ 2	Linear (0-15 kPa)	[137]
Transistor	Carbon nanotube TFT active-matrix backplane	5 V/125 mWcm^{-2}	42.7 Cdm^{-2} kPa^{-1}	5	Linear (0-98 kPa)	[138]
Capacitance	CNTs/Ecoflex/ PDMS	-	0.23×10^{-3} kPa^{-1}	50	Linear (0-900 kPa)	[139]
Capacitance	CNT microyarn/ Ecoflex/PDMS	-	0.5×10^{-3} kPa^{-1}	0.0004	Linear (10-25 kPa)	[91]
Capacitance	Microstructured PDMS	80 V/0.75 mWcm^{-2}	0.15-0.55 kPa^{-1}	-	Non-linear (0-7 kPa)	[26]
Capacitance	Single-layer graphene	-	0.01 kPa^{-1}	0.11	Linear (0-20 kPa)	[155]
Piezoresistance	Graphene– Polyurethane Sponge	< 1 V/4 mWcm^{-2}	0.03-0.26 kPa^{-1}	0.009	Non-linear (0-10 kPa)	[94]
Piezoresistance	Laser-scribed graphene	-	0.005-0.96 kPa^{-1}	5	Non-linear (0-113 kPa)	[104]
Piezoresistance	SWNT/PDMS	2 V/0.007 mWcm^{-2}	1.8 kPa^{-1}	0.0006	Non-linear (0-1.2 kPa)	[90]
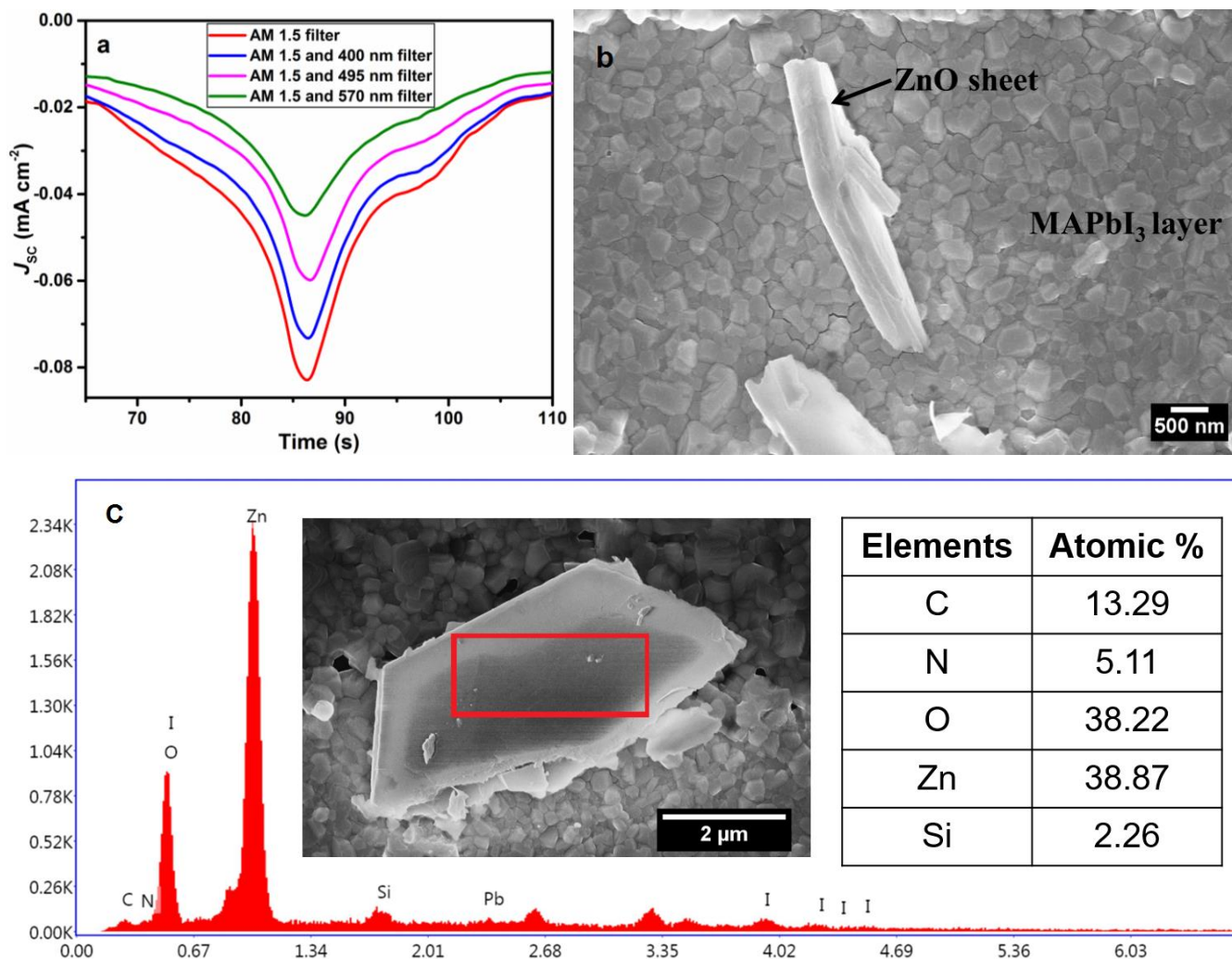
Figure 3.6. Effect of filters and confirmation of ZnO sheets on MAPbI₃ film. (a) The device response in J_{SC} to load cycles of 37 kPa gradually decreases but is sustained on progressively placing long pass filters of increasing wavelengths in the light path. The device was poled at 1 V μm⁻¹ field for 5 min. (b) FESEM image of MAPbI₃ film shows the presence of the ZnO sheet that was used to press on it as a dynamic drain. (c) EDX spectrum and elemental composition confirm the sheet fragment to be ZnO.

To ascertain that the device can function under illumination from light of different wavelengths, we modulated the light of the solar illuminator by placing longpass filters of 400, 495, and 570 nm in its path. As seen in **Figure 3.6**a, the 400 nm filter that eliminates UV light leads to a less than 10% reduction in the J_{SC} response. This also illustrates that the photoexcitation of the ZnO sheets (which have a bandgap of 3.4 eV) does not play any significant role in the functioning of the device. Placing the 495 nm filter reduced the J_{SC} response by 30% and 570 nm filter reduces it by more than 50%, which is consistent with the broad absorbance spectrum of MAPbI₃ from

300 nm to 780 nm.[146] The FESEM image of the MAPbI$_3$ film taken after multiple days of pressure measurements and removal of the ZnO electrode show the presence of the residual sheets on the MAPbI$_3$ film (Figure 3.6b). The energy dispersive X-ray spectrum of Figure 3.6c confirms the elemental composition of the sheet fragment to be ZnO. This observation further confirms the device structure and the model presented in Figure 3.6a.

3.4 Summary

Both ferroelectric and ion migration behaviors are observed in MAPbI$_3$ films based on the conditions used for poling the films. The effects are the result of the materials response to applied poling fields, with each dominating under particular conditions. Further, the ion-back diffusion effects and redox-based degradation are minimal in these devices under the operating conditions. These effects are, however, critical and can become dominating at other conditions that might be used in perovskite-based devices and need to be carefully considered. The two proposed effects are also distinguished based on the observed reversal of the polarity of the V_{OC} and J_{SC}. We also believe that more experiments need to be performed to ascertain the proposed mechanism for the observed effects and especially the role of O$_2$ adsorption and defects in MAPbI$_3$. The ferroelectric response combined with the semiconducting nature of these MAPbI$_3$ films leads to a sustained V_{OC} on the order of few hundreds of mV and a small J_{SC}. Using this ferroelectric-semiconducting nature of the MAPbI$_3$ films, we have then demonstrated a solar (light) powered tactile sensor that functions for more than 72 h after poling for just 5 min at 1.5 V μm^{-1}. The device functions by using a dynamic drain made from ZnO nanosheets whose interfacing area with the MAPbI$_3$ channel modulates in response to the applied pressure. The only electrical energy required to operate the device is during the poling process, which is $\approx$ 55 μW h cm^{-2}. Such low energy cost and solar driven devices are highly relevant for remote sensing, wearable sensors, and continuous monitoring applications. The use of ferroelectric-semiconducting nature of the MAPbI$_3$ films opens the avenue to explore these effects in other similar materials and use them for development of new low cost solar-light driven devices and sensors.

Part B

Nanostructured Materials for Catalytic Applications

Chapter 4
Gold Nanoparticle Chains Supported Platinum-Ruthenium Catalysts for Ethanol Oxidation

4.1 Introduction

With the increasing need for energy and severe ecological effects generated by the combustion of fossil fuels, energy conversion devices which can convert chemical energy to electric power in a much more environmentally favorable way, are in great demand.[1,3,43-45,156] Direct-ethanol fuel cell (DEFC) is an attractive system among various types of fuel cells, considering ethanol's low toxicity and wide availability compared to methanol. However, the performance of DEFC is limited by the lack of highly reactive and durable catalysts.[48,49,52] Numerous studies have been done on developing new catalysts to improve the kinetics by increasing the overall rate and peak current density, lowering the onset potential, and extending the life-time.[48,52,50,53,55] Depositing a thin layer of bimetallic Pt-Ru catalyst on nanoscale structures has been shown to be a successful approach to reduce the cost while maintaining the catalytic performance.[58,157,158] Additionally, the structure at nanoscale, such as spatial composition and elemental percentage of the bimetallic catalyst, play important roles in determining the catalytic performance.[60,158,159] By combining Au nanoparticles with metal cations, we report a facile and straightforward fabrication method of nanoscale PtRu catalysts. In our study, binary or ternary nanocomposite can be easily synthesized by adding one or multiple cations. Specifically, spatial elemental compositions of the nanocomposite can further be tuned by controlling the self-assembly process, owing to the facile synthesis method.

As a result of the dimethyl nature, ethanol oxidation reaction (EOR) is much more complex compared to that of a monomethyl alcohol.[49,50,53,57] Research suggests that the complete oxidation process of ethanol to carbon

dioxide to be a complex multistep reaction with a commonly accepted dual-pathway mechanism, as shown in equation 4.1 and 4.2.[53]

$$CH_3CH_2OH \xrightarrow{2\,e^-} CH_X + CO \xrightarrow{12\,e^-} CO_2 \qquad C1\ pathway \tag{4.1}$$

$$CH_3CH_2OH \xrightarrow{2\,e^-} CH_3CHO \xrightarrow{2\,e^-} CH_3COOH \qquad C2\ pathway \tag{4.2}$$

The C1 pathway represents the complete oxidation by allocating 12 electrons, while the C2 pathway is only partial oxidation to acetaldehyde or acetate by delivering 2 or 4 electrons respectively. A number of adsorbed intermediates and byproducts have been identified to form in both pathways, such as adsorbed CO, acetaldehyde and acetic acid.[46] Metallic platinum (Pt) and other noble metals have been used widely as catalytic materials owing to the distinct properties in adsorption and desorption of target molecules on these metals.[53,58,160,161] Nevertheless, bare Pt suffers from strong interactions with intermediates including CO-type species.[50,53] The intermediates will preferably bind to available sites on the Pt surface and consequently hinder the adsorption of more ethanol molecules, which in turn significantly decrease performance of Pt over time.[50,162] Research efforts have been devoted to develop binary or ternary Pt-based co-catalysts to overcome these challenges. Ru, Rh, Au, Sn, and Ni have been reported for exhibiting outstanding catalytic performance as co-catalysts with metallic Pt.[54,56,163] Apart from minimizing the use of the precious material, bimetallic catalysts have one major benefit over the metallic Pt: a bifunctional effect that increases the amount of oxygen species supplied for oxidation of adsorbed CO.[53,162] During the past decades, fabrication of Pt-based nanostructures has attracted much research attention for enhancing the catalytic properties by changing the nanoscale structure and providing more available active sites.[1,53,164] Accordingly, depositing a thin layer of Pt-based materials on nanoscale structures appears to be a successful approach to reduce the cost while maintaining the high surface area. Graphene, carbon nanotubes (CNTs), and TiO_2 matrices have been used as supporting materials for effectively dispersing the nanomaterial layers.[58,59,165]

In this study, we demonstrate a facile fabrication method of ternary Pt-Ru-Au catalysts in bulk quantities for ethanol oxidation. Pt^{4+} and Ru^{3+} ions are used as linkers to assemble the negatively charged citrate-capped Au

nanoparticles into chains through electrostatic force. A layer of Pt-Ru nanocomposite is further deposited on the nanoscale chains as shells by chemically reducing the metal cations covering on the nanoparticle surface. The atomic composition of the nanocomposite can be easily altered by varying the ratio of the cations. By controlling the self-assembly process, spatial compositions of the nanocomposite could be tailored for desirable structures. The use of chain-like Au nanostructure can be beneficial in multiple aspects. In the first place, the structure works as a supporting template to ensure the dispersion of the Pt-Ru catalysts by diminishing the agglomeration. Secondly, the Au nanoparticle chains provide sites for spatially confined fabrication of the Pt-Ru nanocomposites, which is crucial for maximizing the surface area. We find that chains with well-defined domains of Pt-Au and Ru-Au on the size of 5-10 nm show the best performance in stability and ethanol oxidation. In comparison, a homogenous mixture of Pt-Au and Ru-Au domains is 29 % less effective in performance. We also compare the performance of these systems with commercial Pt/C catalyst. The process of fabricating chain-like structure opens the use of such nanoparticle chains for many applications in which the spatial composition needs to be tuned.

4.2 Material and Methods

4.2.1 Synthesis of Gold Nanoparticle Chains

10 nm citrate capped gold nanoparticle solutions were purchased from BBI solutions. 500 µL of 5 mg ml^{-1} PtCl$_4$ was added to a glass vial which contains 3.0 ml of the 10 nm Au nanoparticle solution. Similarly, 150 µl of 2 mg mL^{-1} RuCl$_3$ was added to assemble 3.0 ml of the Au nanoparticle solution. Metal cations used for the assembly process can vary from monovalent to tetravalent. The variations in cations will lead to different amount and time required for assembly. The difference is expected to be a combined effect of the valency, electronegativity, and hydrodynamic radius of the different cations. The solutions were put on a vortex mixer for assembling of Au-nanoparticles. Assembling time varies from 8 to 24 h for different metal cations. By inter-mixing these solutions after the formation of assembled chains at varying stages, spatial control of different cations is achieved. Samples with different Pt:Ru elemental compositions: 100:0 (pure Pt), 95:5, 90:10, and 80:20 were synthesized by varying the volume of each assembled solution in the mixture solution. The final solution is well mixed for enough time to allow the assembly of the final structures, in which there are two cations adsorbed onto the Au surface with a spatial distribution. Sodium borohydride (NaBH$_4$) was then added after the assembly as a reducing agent to the solution for reduction of the metal cations to nanoparticles.

4.2.2 Characterizations

The self-assembled Au nanoparticle chains were characterized by ultraviolet-visible spectroscopy (UV-Vis), and dynamic light scattering (DLS) was used for confirming the size increase in assembled chain-like structures. X-ray photoelectron spectroscopy (XPS) technique was used to characterize the surface composition of the synthesized materials. The crystal structure was characterized by glancing incidence X-ray diffraction (GIXRD) using a PANalytical X'Pert Pro MRD diffractometer with Cu Kα radiation (λ = 1.54 Å) at an incidence angle of 0.4°. Transmission electron microscopy (TEM) was carried out to examine the morphologies and sizes of the catalysts.

4.2.3 Electrochemical Measurements

Electrochemical measurements were carried out using a CompactStat electrochemical interface & impedance analyzer at room temperature. A standard three-electrode set up has been used for all experiments. In all cases, a Ag/AgCl/Saturated KCl electrode was used as the reference electrode, and a Pt wire was used as the counter electrode. A 3 mm (diameter) glassy carbon electrode (GCE) was used as the substrate for depositing the catalyst solutions. Before each measurement, the GCE was polished using 0.05 μm alumina powder. The catalyst solutions were sonicated for 1 h, followed by immediate deposition of 5 μl of the catalyst solution onto the GCE. The working electrodes were then left for 2 h for the evaporation of electrolytes and complete deposition of catalysts.

Prior to all experiments, the GCEs were rinsed with DI water. As the pretreatment step for all samples, conditioning cycles in an acidic solution of 0.1 M $HClO_4$ for 100 cycles from -0.05 V to 0.6 V with a scan rate of 200 mV/s were done. The electrochemically active surface area measurements were then determined by integrating the hydrogen adsorption charge on the cyclic voltammetry (CV) at room temperature in nitrogen saturated 0.1 M $HClO_4$ solution with a scan rate of 50 mV/s. Electrooxidation of ethanol was performed in 0.1 M $HClO_4$ and 1 M ethanol with a scan rate of 50 mV/s. ChronoAmperometry (CA) measurements were performed at a constant voltage of 0.5 V for 45 min in the same solution, to determine the stability/life-time of the catalysts. For comparison, commercial Pt/C (20 wt. % loading, Sigma-Aldrich) was used as the baseline/control catalyst, and same procedures were conducted for all experiments.CO adsorption was done by keeping the potential at -0.20 V for 20 mins while bubbling CO through the acidic solution of 0.1 M $HClO_4$. Nitrogen was bubbled again for 10 mins to remove any of the residual CO in the electrolyte. CO stripping was then carried out by doing CV cycles in 0.1 M $HClO_4$ solution from -0.2 V to 1.2 V at 20 mV/s.
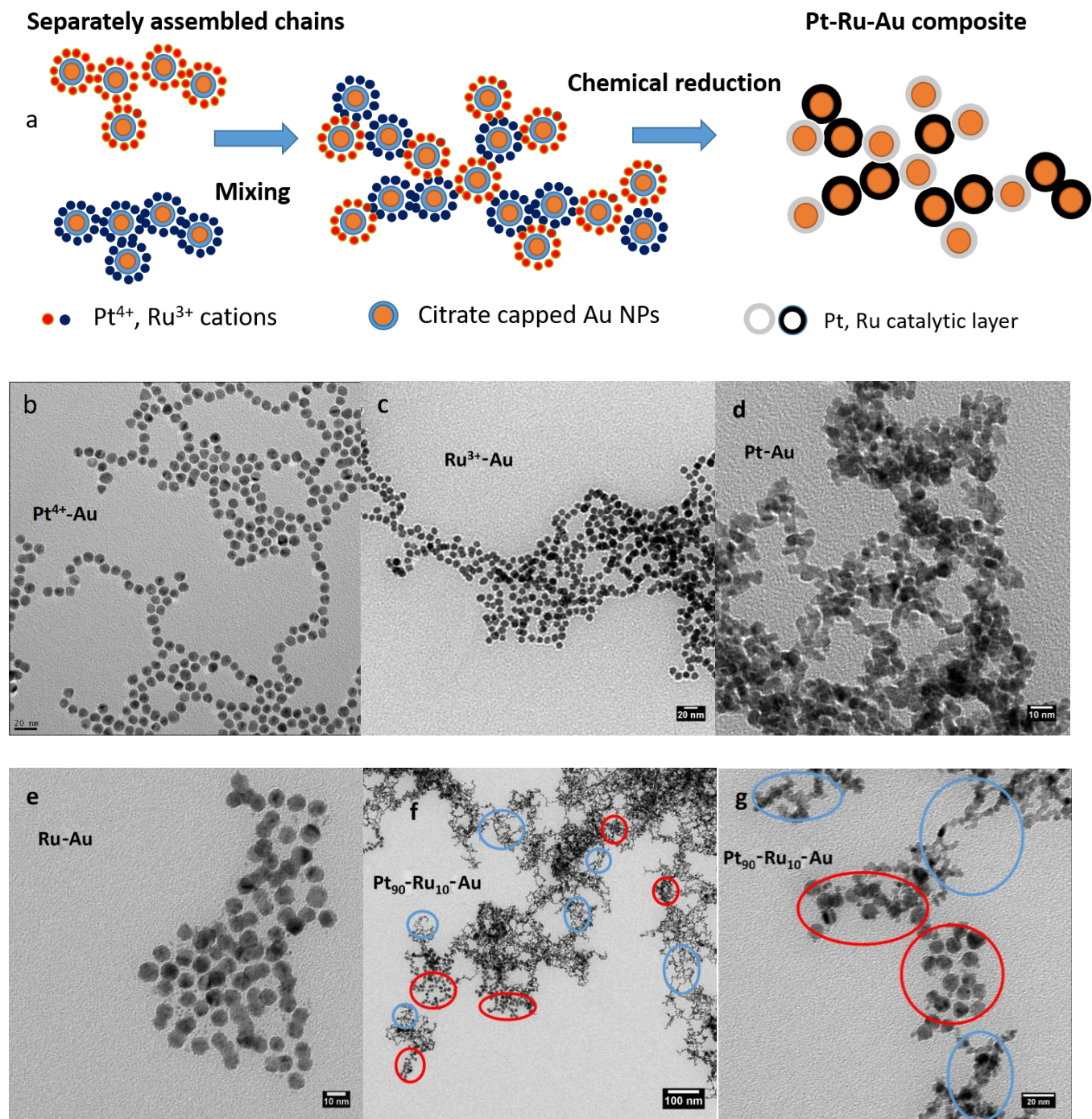
4.3 Results and Discussion

Figure 4.1. (a) Schematic of the assembly-reduction process of fabricating the nanocatalysts. TEM images of (b) Pt^{4+} assembled Au nanoparticle chains, (c) Ru^{3+} assembled Au nanoparticle chains, (d) Reduced Pt-Au nanocomposite, (e) Reduced Ru-Au nanocomposite, (f) and (g) Reduced Pt-Ru-Au nanocomposite (Pt-Au circled in blue and Ru-Au circled in red).

The schematic in Figure 4.1a shows the self-assembly process of Au nanoparticles, and subsequently the formation of the Pt-Ru layer by chemical reduction of the metal cations. We start by having Pt^{4+} and Ru^{3+} assisted nanoparticle assembly processes simultaneously going in two separate vessels. Ru^{3+} are used in order to overcome the poisoning effect associated with bare Pt catalysts, forming a ternary Pt-Ru-Au nanocomposite. The positive charge on the metal cations bring the negatively charge citrate-capped Au nanoparticles into close physical proximity. The UV-Vis (see Appendix) shows a shift in the absorbance peak from 525 to above 600 nm when particles assemble into chains. The peak at 525 nm corresponds to the surface plasmon resonance of the isolated nanoparticles, while the shift to 600 nm is primarily due to the plasmon coupling between adjacent nanoparticles, which further confirms formation of the chain-like structure in the solution phase. The solutions are put together following the formation of the chains linked by Pt^{4+} and Ru^{3+} cations. The bimetallic Pt-Ru layer on Au nanoparticles is fabricated upon the addition of the reducing agent lastly, with the atomic composition of Pt:Ru varying from 100:0 (pure Pt) to 80:20.

The self-assembled chains linked by Pt^{4+} and Ru^{3+} can be seen in the TEM images (Figure 4.1b and 4.1c). It can be seen that the assembled chains have an average size of 500 nm in length with 1-2 nm spacing between particles before the reduction of metal cations. The spacing is believed to be occupied by the citrate capping and the metal cations. The assembly is also monitored by dynamic light scattering (DLS), with a hydrodynamic radius of 220 nm in hydrodynamic radius and a zeta potential of –36 mV after assembly.(see Appendix)

It can be expected that, the metal cations in the system are either adsorbed onto the surface of the Au nanoparticles because of the electrostatic force, or diffused in the solution. To better understand the distribution of the cations, the solution is centrifuged at 14000 rpm to precipitate all nanoparticle chains after assembly. After measuring the absorbance peak of the top solution using UV-Vis, the calibration curve plot shows that 51% of the metal cations are found to suspend in solution, while the remaining cations are expected to be adsorbed onto the Au surface. In order to validate the reducing mechanism of the metal cations on nanoparticle surfaces, an approximate

ion concentration of 3.5 mM was calculated based on the ionic conductivity of 1185 µS in the Au solution. Accordingly, the Debye length, which is proportional to the square root of the ion concentration, is expected to be around 5 nm using the assumption ($\frac{1}{\kappa} = \frac{0.304}{\sqrt{I(M)}}$) in a typical NaCl solution.[166] Furthermore, the concentration of the cations adsorbed on Au surface is calculated to be 5000 times higher than that of the diffusion layer and the bulk solution, as a result of the adsorption/accumulation on the nanoparticle surfaces. Following the assembly of nanoparticle chains, NaBH$_4$ is added to the system as a reducing agent to chemically reduce the metal cations into their neutral metallic forms. Because of the concentration difference, the proposed chemical reduction of metal cations occurs predominantly on Au surface. This is based on the thermodynamics that favors the nucleation of the metals at regions of higher concentration. Rate of nucleation has been described by:

$$R_N = \left\{\frac{C_0 kT}{(3\pi\lambda^3\eta)}\right\} exp\left(\frac{-\Delta G^*}{kT}\right). \tag{4.3}$$

where C$_0$ is the concentration, λ is the diameter of the growth species, η is the viscosity of the solution, and the exponential part describes the thermodynamic fluctuation of critical free energy.[167] It can be seen from the equation that the nucleation is favored with higher concentration, thus the subsequent growth of the metal forms hence occurs preferentially on the Au chains. Additionally, the underlying Au nanoparticles work as seeds for nucleation of the metal nanoparticles, which further boosts the growth of the nanocomposite layer. The TEM image in Figure 4.1d confirms the confined the growth the only Pt layer on the Au nanoparticle chains, in which only Pt^{4+} cations are the linkers for self-assembly. The spacing between nanoparticles can no longer be seen after reduction. Instead, the separated nanoparticles are fused together to form a chain-like network. The average width of the structure is around 5 nm and the small size increases the exposed surface active sites of the Pt. Interestingly, Au nanoparticle chains do not fuse and connect each other to form continuous structures when Ru^{3+} cations are reduced, as seen in Figure 4.1e. However, it can be observed that there are small Ru nanoparticles on the scale of 1-2 nm surrounding all Au nanoparticles, which has not been seen for other samples. We believe this phenomenon can be explained by the molar ratio difference between Ru and Au: 7.4 µmol of Pt is present in the case where Pt^{4+} is the linker and the

amount is believed to be enough for covering the 0.87 µmol of Au nanoparticles; whereas the relatively low amount of 0.71 µmol Ru could not fully cover Au surfaces and the gaps. More experiments to study the complete assembly-reduction mechanism are being conducted by my colleagues in the Maheshwari Lab.

After mixing and chemical reduction of the two solutions, the chain-like structure shows distinct spatial distribution of two nanocomposites (Pt-Au and Ru-Au). Figure 4.1f shows a TEM image of the Pt-Ru-Au nanocomposite with an elemental composition of 90 to 10 after the chemical reduction at a low magnification. It can be observed that the chain-like structures are highly porous, which is crucial for improving the catalytic activity. Furthermore, the image shows well defined domains of Pt-Au (circled in blue) and Ru-Au (circled in red) with distinct spatial distribution. From the high magnification TEM image (Figure 4.1g), we can clearly see the distinguishable regions of Pt-Au and Ru-Au by their individual morphologies.

To better study the assembly-reduction process, X-ray photoelectron spectroscopy (XPS) was carried out to examine the surface composition for the assembled chains before and after adding the reducing agent. Figure 4.2a shows the XPS spectra for the Pt 4f region for the samples, in which $4f_{7/2}$ and $4f_{5/2}$ are the main peaks to study. Without adding NaBH$_4$, peaks located at 72.9 and 76 eV indicate the existence of Pt^{4+}. The binding energies of Pt $4f_{7/2}$ for the reduced Pt-Au and Pt-Ru-Au samples both locate at 71.1 eV, whereas the $4f_{5/2}$ binding energies show at 74.4 eV. The peak separation of 3.3 eV and the doublet positions are consistent with Pt being in a metallic state, which indicates the unaltered chemical state of metallic Pt in the composites. A peak shift is not observed for Au compared to the metallic Au peaks (see Appendix), which further demonstrates that there is no alloy forming in all samples. The peak for the binding energy of Ru $3d_{5/2}$ located at 281.8 eV indicates the existence of Ru^{3+} in the ruthenium assembled chains, as shown in Figure 4.2b. The peak is strongly reduced in Ru-Au and Pt-Ru-Au samples, while the peak at 285 eV confirms the formation of metallic ruthenium after the chemical reduction. As shown in Figure 4.2c, the diffraction peaks at 38.1°, 64.5°, and 77.7° can be assigned, respectively, to the Au (111), (220), and (311) planes. Similarly, (011), (002), and (200) planes for Ru are observed in the Ru-Au nanocomposite, while

(111), (200), (220), and (311) planes can be seen in the Pt-Au sample. These XRD features are consistent with the

XPS results, which reveals no alteration in the crystal structures of each component element.
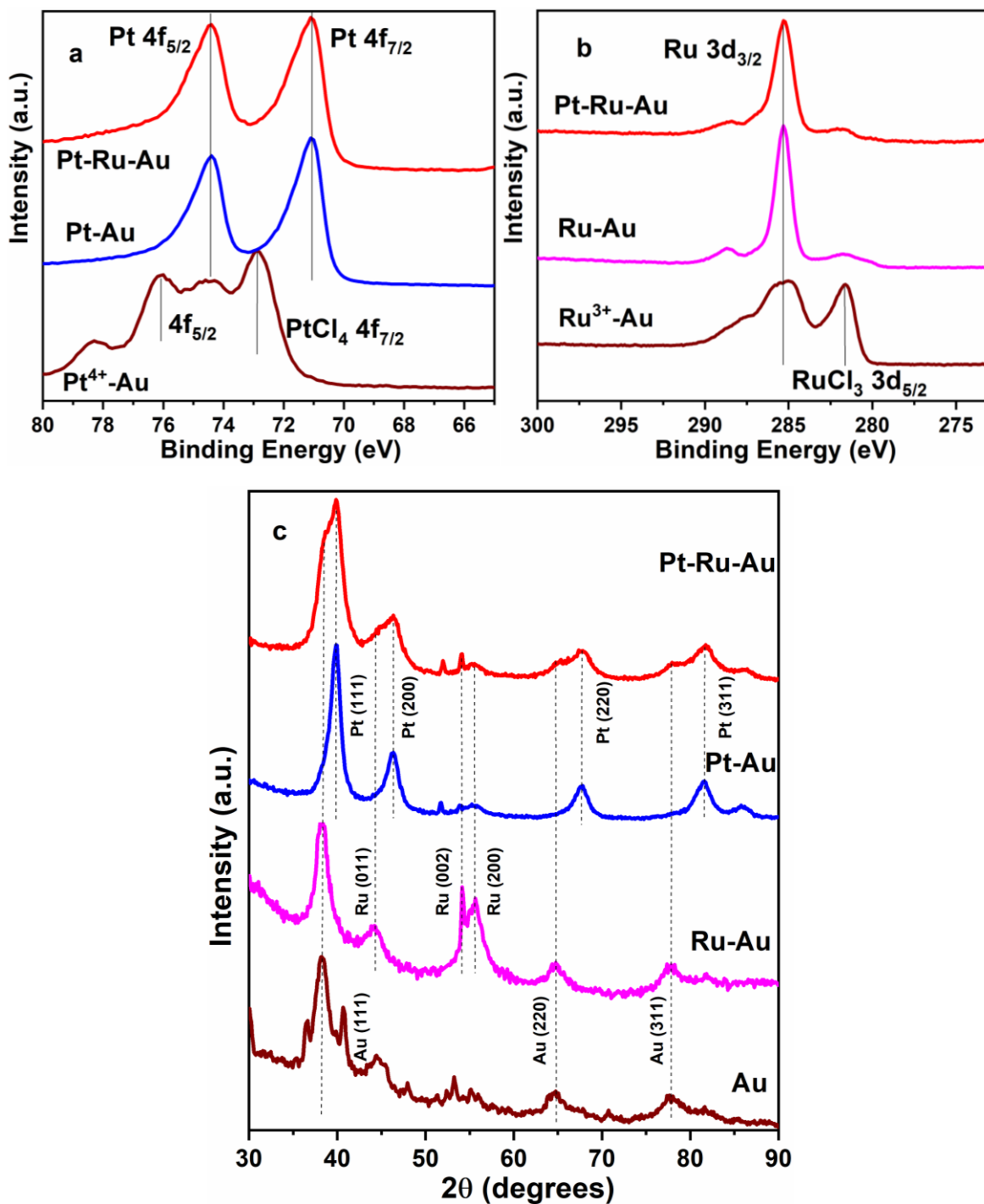

Figure 4.2. XPS (a and b) and XRD (c) spectra of plain Au nanoparticles, Pt^{4+} and Ru^{3+} assembled Au chains, Pt-Au and Ru-Au nanocomposite, and Pt-Ru-Au nanocomposite (with an Pt:Ru elemental composition of 90:10).

The nanocomposite solutions are loaded onto the surface of freshly cleaned glassy carbon electrodes (GCEs) to evaluate the EOR electrocatalytic activity of the as-prepared Pt-Ru-Au nanocomposites, with varying elemental composition. To compare, the binary Pt-Au and commercial Pt/C (20 wt. % loading) samples are tested under same conditions. Prior to all testing, the samples are activated for 100 cycles in 0.1 M HClO$_4$ to clean the catalyst surface of any surface impurities for activation of the catalysts. All electrochemical tests are reported with a normalized 1.0 µg Pt mass loading on the GCEs. The electrochemical active surface area (ECSA) is then measured in same solution of 0.1 M HClO$_4$. The values are estimated based on the underpotentionally deposited hydrogen (H$_{upd}$) in HClO$_4$ with a standard conversion factor of 210 µC cm^{-2} using the equation:

$$ECSA = \frac{Q}{210} \mu C \ cm_{Pt}^{-2} \tag{4.4}$$

Where Q is the charge associated with the adsorption of a hydrogen atom monolayer, which can be determined experimentally by integrating the charges.[168] The specific value of 210 µC cm^{-2} is used as the standard conversion factor, which can be derived by e × d$_m$ (charge of an electron × surface metal atom density of Pt: 1.3×10^{15} cm^{-2}).

As shown in Figure 4.3a and 4.3b, the synthesized Pt-Au nanocomposite exhibits a value of 26.2 m^2 g$_{Pt}^{-1}$, whereas the commercial Pt/C has a highest ECSA of 36 m^2 g$_{Pt}^{-1}$. The difference can be explained by the small Pt nanoparticles (≤ 5 nm) loading on graphitized carbon in the commercial sample, which is beneficial for dispersion and exposing Pt. However, the comparable values of Pt-Au and Pt-Ru-Au samples indicate the effective dispersion of Pt materials on the Au nanoparticle chains. As can be seen, the ECSA decreases from 26.2 to 15.7 m^2 g$_{Pt}^{-1}$ as the elemental composition of Pt decreases from 100 to 80%. The decline in surface area is in good agreement with the reported mechanism in which hydrogen molecules are mostly adsorbed on the Pt surface.

CV measurements are carried out in 0.1 M HClO$_4$ and 1 M ethanol to address the catalytic performance of the nanocomposites towards EOR. In our study, the specific activity on a mass basis, which is more economically relevant, is reported for all samples. The EOR curves of the binary Pt-Au and ternary Pt-Ru-Au with varied elemental ratios are compared to commercial Pt/C in Figure 4.3c. The onset oxidation potential and the peak current

density are two major parameters to evaluate the electrocatalytic activity of the catalysts. Typically, in a diffusion-limited reaction, a peak of electrical current appears in a CV cycle when the rate of reaction is limited by the mass transfer process. As a result of the diffusion process, the peak current increases with the square root of the scan rate.[169] Nevertheless, the electrooxidation of ethanol in acidic medium at Pt surface is believed to be a complex process with multiple steps. It is commonly accepted that, acetaldehyde (CH_3CHO) is the primary intermediate during the forward scan of EOR at Pt catalysts, instead of the complete oxidation to CO_2.[53] Therefore, instead of reaching the bottleneck of mass transfer, the oxidation peak during the forward scan occurs owing to the formation of intermediates that hinder the adsorption of ethanol molecules. The anodic peak during the reverse scan is generally considered the oxidation of multiple species, including the adsorbed intermediate formed during forward scan, and other carbonaceous species ($-CH_X$).[52] As a result, a low oxidation peak for the reverse scan is an evidence of less adsorbates accumulation during the forward scan. The ratio of the current peak value during forward scan to reverse scan I_f/I_r can be used to describe the catalyst's tolerance to CO-like species. As seen in Figure 4.3c, the forward current peak of the Pt_{90}-Ru_{10}-Au sample at ≈ 0.65 V is about 1.1 mA, which is 3.07 times that of commercial Pt/C (0.36 mA) and 1.68 times that of the binary Pt-Au (0.63 mA). The onset potential of the Pt_{90}-Ru_{10}-Au catalyst is 0.39 V, which is much lower than that of Pt-Au and commercial Pt/C. Among all catalysts, Pt_{80}-Ru_{20}-Au showed the most negative onset potential of 0.31 V. However, the catalytic activity is strongly reduced compared to Pt_{90}-Ru_{10}-Au as Ru content increases. It has been reported that atomic ratio of Ru higher than 20% in Pt-Ru catalysts significantly decreases the electrocatalytic activity. This phenomenon can be explained by not having enough Pt active sites, which is capable of breaking the C-C bond in ethanol, while Ru itself is not suitable for EOR.[53] Figure 4.3d shows the bar diagram of the peak current density of each sample, with error bars denoted in grey. In addition to the highest current density and second lowest onset potential of the Pt_{90}-Ru_{10}-Au, it also shows a higher I_f/I_r ratio of 1.17 compared to commercial Pt/C (0.99), and Pt-Au (1.05). The higher value is expected as the Pt_{90}-Ru_{10}-Au nanocomposite is more intermediate-tolerated by Ru inducing the oxidative removal of the species, and eventually leading to a more complete EOR to CO_2. The surface Ru atoms are believed to readily form Ru-OXO or Ru-OH

species, which will enhance the oxidative removal of adsorbates by donating the hydroxyl groups.[59,170] Similarly, it is observed that higher amount of Ru in Pt_{80}-Ru_{20}-Au increases the I_f/I_r ratio to 1.25. Control samples are also tested to verify the importance of underlying Au nanoparticle chains, as well as the EOR activity of plain Au nanoparticles and Ru-Au nanocomposites. As expected, Au nanoparticle itself the shows no ethanol oxidation behavior in the CV cycles. It has been also confirmed that, without the presence of Au nanoparticles, no chain-like structure is formed and the catalytic activity of reduced Pt^{4+} is relatively low (83 mA mg_{Pt}^{-1}) compared to the commercial Pt/C catalyst (see Appendix). Accordingly, the observed high activity in Pt-Ru-Au sample can be attributed to the porous chain-like Pt-Au composites.

58
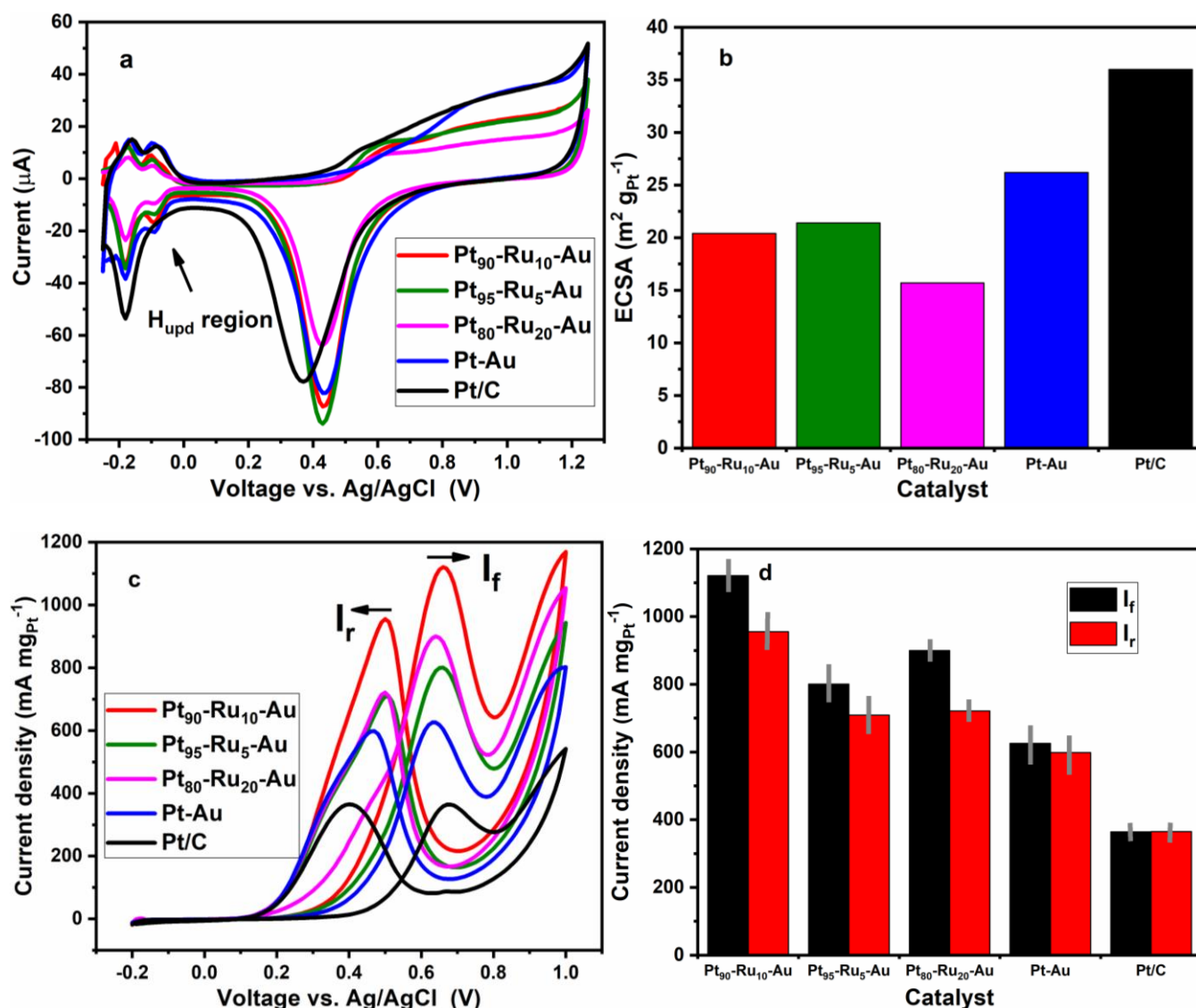
Figure 4.3. Electrochemical characterizations of the Pt-Ru-Au catalysts with a varying elemental composition of Pt:Ru. Commercial Pt/C (20 wt. % loading on graphitized carbon) is tested under same conditions for reference. (a) CVs of ECSA measurements in 0.1 M HClO$_4$ at 50 mV s^{-1}. (b) Bar diagram showing the calculated ECSA for each catalyst. (c) CVs of EOR measurements in 0.1 M HClO$_4$ and 1 M ethanol at 50 mV s^{-1}. (d) Bar diagram showing the current density and I$_f$/I$_r$ ratio of each catalyst.

For fuel cells based on small organic molecule, CO-tolerance of the catalyst is an important criterion as CO is the main poisoning intermediate formed during oxidation. Therefore, CO stripping has been done as a diagnostic tool to provide insights about the CO poisoning tolerance. CO adsorption is done by polarizing the GCEs at -0.20 V for 20 mins while bubbling CO through a 0.1 M HClO$_4$ solution. Nitrogen is bubbled again to make sure that there is no CO is adsorbed in the electrolyte. Figure 4.3f shows the CO stripping CVs of the catalysts, in which the oxidation current exhibits the oxidative detachment of monolayer adsorbed CO on the catalyst surface. Compared to the CO oxidation peak of commercial Pt/C (0.47 V), the peak potential shifted to a low value of 0.43 V for Pt-Au. The potential further shifts to 0.38 V when the elemental composition of Ru increases to 10%, which is a result of the hydroxyl groups on Ru promoting the oxidation of CO to CO$_2$ on the Pt surface.[170] A lowest onset potential of 0.28 V is achieved with a 20% Ru composition, indicating an increase in CO-tolerance. However, high amount of Ru in the Pt$_{80}$-Ru$_{20}$-Au sample does not necessarily improve the activity towards CO oxidation.

The durability/stability of the catalysts is another critical factor for their practical applications. In this regard, 5000 consecutive CV cycles are carried out as an effective method to evaluate both the stability of the nanocomposites. Figure 4.4b shows the peak current densities of the catalysts in 1 M HClO$_4$ and 1 M ethanol with a scan rate of 50 mV. As shown in figure, the decay in current density in all samples is believed to be the formation of reactive intermediates such as CO, acetate, and acetaldehyde during the EOR. It is noteworthy that the Pt$_{90}$-Ru$_{10}$-Au catalyst shows the highest initial value and attains a peak current value of 397 mA mg$_{pt}^{-1}$ after three days (5000 cycles). Ru has been reported to improve Pt's stability against deactivation by providing oxygenated surface species without compromising the adsorption of ethanol on Pt sites. Compared to the Pt-Au catalyst, which maintains a 9.5% activity, the Pt$_{90}$-Ru$_{10}$-Au catalyst shows a much less attenuation after 5000 CV cycles. Activity of the commercial

Pt/C The results further demonstrate that Pt$_{90}$-Ru10-Au exhibit higher electrocatalytic activity and stability towards

EOR, which are consistent with the CV results. Table 4.1 summarizes the key electrocatalytic parameters for each

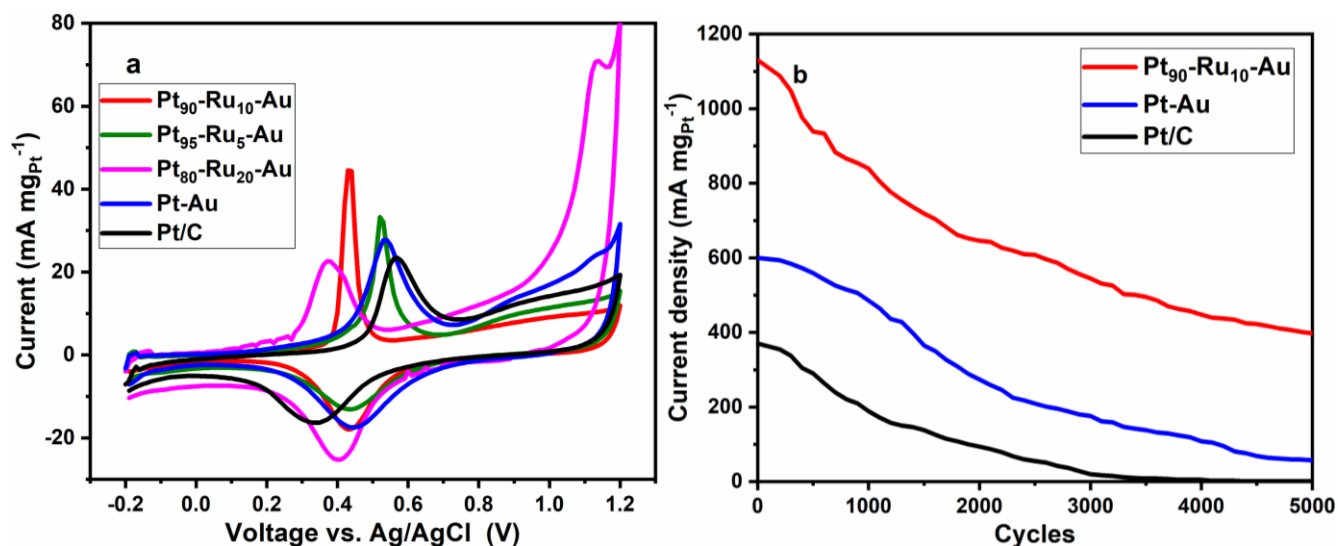synthesized catalyst and multiple reported Pt-based catalysts.

Figure 4.4. (a) CO oxidation/stripping CVs of each catalyst in 0.1 M HClO$_4$ solution. (b) Peak current density of 5000 cycles of three catalysts in 0.1 M HClO$_4$ and 1 M ethanol.

Table 4.1. Comparison of the performance of the catalysts with varied elemental compositions of Pt:Ru.

Catalyst	Peak current density (mA mg$_{Pt}^{-1}$)	EOR onset potential (V)	CO oxidation onset potential (V)	Activity after 5000 cycles (%)	Ref.
Pt$_{90}$-Ru$_{10}$-Au	1120.1	0.39	0.38	35.2	This work
Pt$_{95}$-Ru$_5$-Au	800.1	0.43	0.43	-	
Pt$_{80}$-Ru$_{20}$-Au	899.7	0.31	0.28	-	
Pt-Au	625.6	0.45	0.43	9.5	
Pt-NiO/C	644	0.49	0.32	-	171
PtRu/FLG	970	0.48	-	75 after 2000 s	172
PtRh/TiO$_2$-C	1039	0.62	0.35	76 after 3600 s	173
PtRu/ C core-shell	811	0.45	-	50 after 1800 s	174
PtRh NW/GNs	1000	0.30	-	85 after 2000 cycles	175
Pt/C	364.6	0.49	0.47	0.27	-

In addition to varying the elemental composition of Pt:Ru, the timing of mixing the two Pt^{4+}-Au and Ru^{3+}-Au solutions is also studied to see its effect on the electrocatalytic activity while keeping the atomic ratio of Pt:Ru at 90:10. Instead of mixing the fully assembled solutions, new samples are made by mixing at halfway of the assembly process (denoted by Pt-Ru-Au$_{inter.}$) and at the beginning without formation of the assembled chains (denoted by Pt-Ru-Au$_{beg.}$). As seen in the TEM images in Figure 4.5a and b, Pt-Au and Ru-Au nanoparticles are well mixed together to form a relatively homogenous structure without clear boundaries of each domain. It can be observed in Figure 4.5b that there are Pt-Au between/surrounding Ru-Au nanoparticles, and vice versa. Similar phenomenon has been observed previously by mixing assembled 10 nm and 100 nm Au nanoparticles at different stages. The distinct morphology difference clearly exhibits the impact of mixing time, as seen in Appendix.
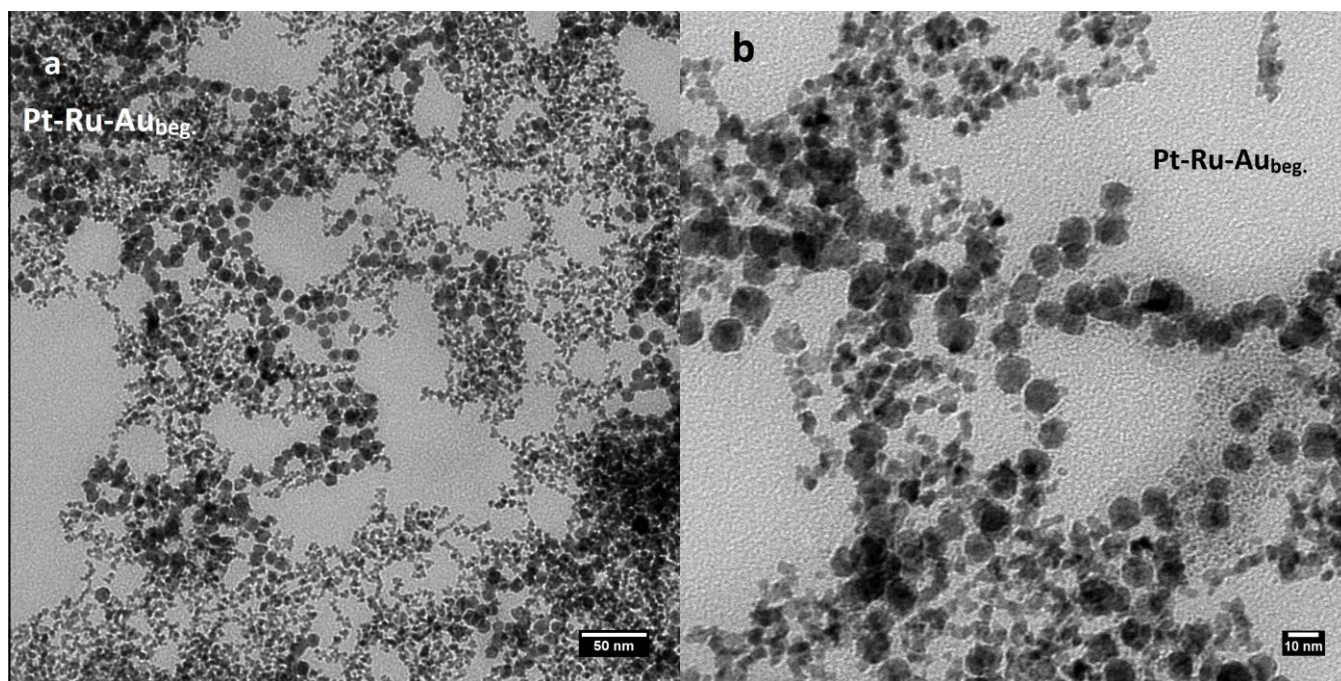
Figure 4.5. TEM images of Pt-Ru-Au$_{beg.}$ catalyst at different magnifications.
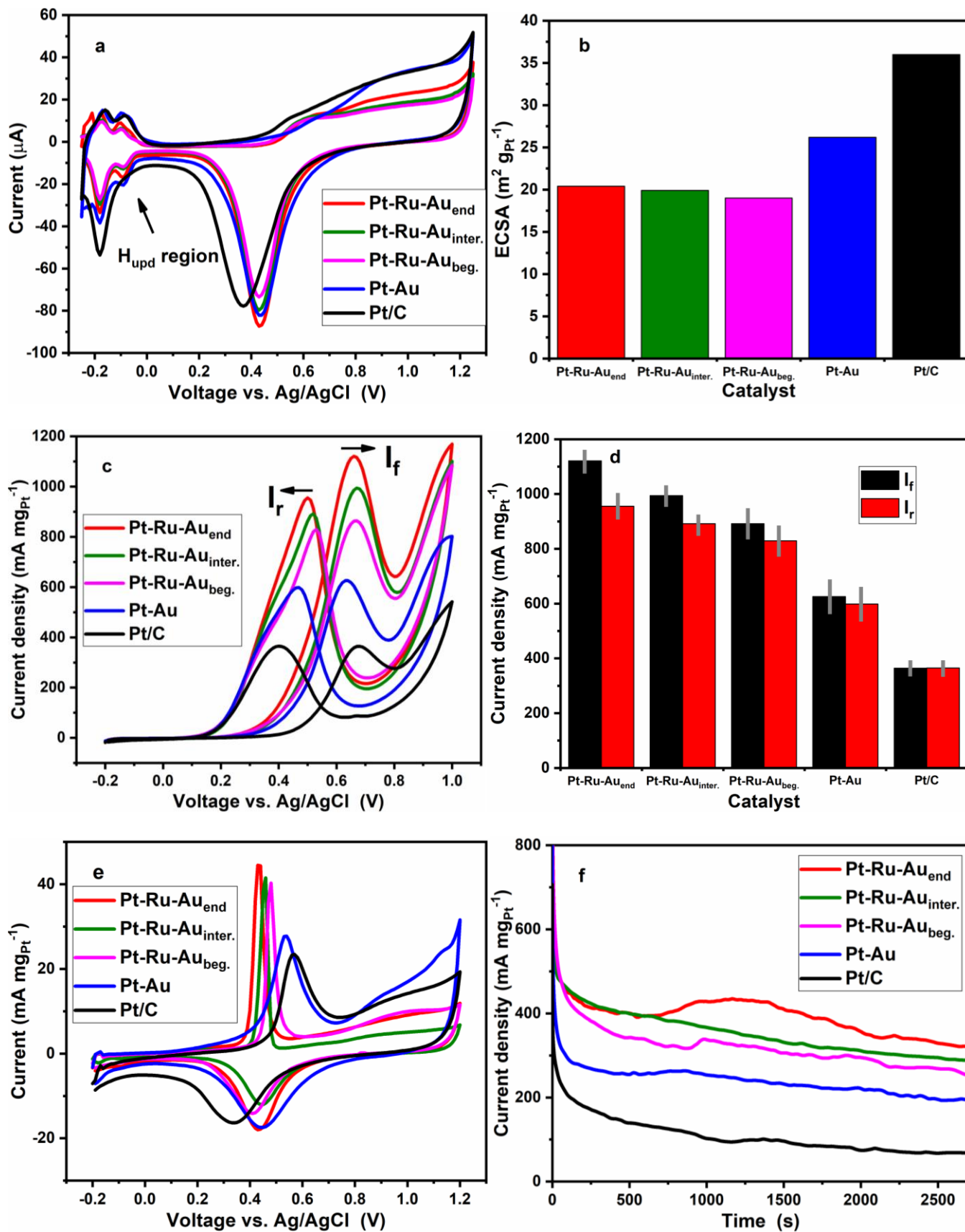
Figure 4.6. Electrochemical characterizations of the Pt-Ru-Au catalysts with varying mixing timing of Pt^{4+}-Au and Ru^{3+}-Au solutions. Commercial Pt/C (20 wt. % loading on graphitized carbon) is tested under same conditions for reference. a) CVs of ECSA measurements in 0.1 M $HClO_4$ at 50 mV s^{-1}. b) Bar diagram showing the calculated ECSA for each catalyst. c) CVs of EOR measurements in 0.1 M $HClO_4$ and 1 M ethanol at 50 mV s^{-1}. d) Bar diagram showing the current density and I_f/I_r ratio of each catalyst. e) CA measurements of each catalyst at 0.5 V in 0.1 M $HClO_4$ and 1 M ethanol. f) CO oxidation/stripping CVs of each catalyst in 0.1 M $HClO_4$ solution.

It has been reported that the electrocatalytic activity is also governed by the relative placement of their constituting elements with respect to each other.[159,176-178] This is based on the fact that the reactants, their intermediates and products will be adsorbed on the catalyst surface and the diffusion of these species on the surface with transfer between the catalyst and co-catalyst sites is required for effective reaction.[50,56] Therefore, more experiments are conducted to investigate the difference in electrocatalytic activities due to the difference in morphologies of the Pt-Ru-Au catalysts. The catalysts are tested and compared to Pt-Au and commercial Pt/C under same conditions for all electrochemical characterizations. As shown in Figure 4.6a and b, there is a gradual increase in ECSA with the delay in mixing timing. Pt-Ru-Au catalyst mixed at the end of assembly shows a 7.4 % increase of the ECSA compared to the sample mixed in the absence of assembled chains, yet the two catalysts have the same amount of Pt and Pt:Ru elemental composition. The Pt-Ru-Au catalyst mixed after assembly of chains also exhibited a higher electrocatalytic activity for EOR. It can be seen in Figure 4.6c that the peak current density of Pt-Ru-Au$_{end}$ is 29 % higher than the homogenous Pt-Ru-Au$_{beg.}$, while Pt-Ru-Au$_{inter.}$ shows a current density value in between of the two extremes. The mixing timing also shifts the EOR onset potential from 0.43 to 0.38 V, with a corresponding I_f/I_r value from 1.04 to 1.17. The catalyst mixed after assembly of chains also exhibits the best CO-tolerance by having the lowest CO oxidation peak of 0.38 V (Figure 4.6e). In CA tests shown in Figure 4.6f, Pt-Ru-Au$_{beg.}$ and Pt-Ru-Au$_{inter.}$ catalysts both show a higher attenuation of 25 %, whereas the current density of Pt-Ru-Au$_{end}$ reduces for only 20 % after 2700 s at 0.5 V. The lowest onset potentials and attenuation, highest I_f/I_r value and current density indicate the best electrocatalytic activity of Pt-Ru-Au$_{end}$ catalyst among all samples owing to its morphology with well-defined domains of Pt and Ru. The difference in the performance as a result of the morphology difference can be explained by the previously reported dilution of catalytic Pt surface sites.[157] It has been proposed that several

63

neighboring Pt sites are required in order to effectively oxidize molecules, while isolated surface Pt clusters are less

capable to decompose the target molecules.[179,180] Table 4.2 summarizes the key electrocatalytic parameters for

each catalyst with varying mixing stages.

Table 4.2. Comparison of the performance of the Pt_{90}-Ru_{10}-Au catalysts with varied mixing stages.

Catalyst	ECSA (m^2 g_{Pt}^{-1})	Peak current density (mA mg_{Pt}^{-1})	EOR onset potential (V)	CO oxidation onset potential (V)	Reduction in activity after 2700 s
Pt-Ru-Au$_{end}$	20.4	1120.1	0.39	0.38	20
Pt-Ru-Au$_{inter.}$	19.9	994.1	0.43	0.41	25
Pt-Ru-Au$_{beg.}$	19	864.1	0.45	0.43	25
Pt-Au	26.2	625.6	0.45	0.43	24
Pt/C	36	364.6	0.49	0.47	52

4.4 Summary

We have developed a facile approach to synthesis of highly porous, high surface area chain-like nanostructured materials using self-assembled Au nanoparticle chains linked by Pt^{4+} and Ru^{3+} cations. The easy fabrication process allows the optimization of the relative amounts and placement of each component with respect to each other in the catalyst. By inter-mixing the chains at different stages of assembly, spatial control of distinguishable domains of Pt-Au and Ru-Au on the size of 5-10 nm is achieved. The prepared Pt-Ru-Au catalyst with well-defined domains shows an electrocatalytic activity which is 3.1 times that of commercial Pt/C. Apart from the high current density, the Pt-Ru-Au catalyst also exhibits a much less attenuation and a higher CO-tolerance. Furthermore, in contrast to the homogenous structure, the morphology with distinct domains significantly enhance the EOR performance (29 % increase in current density) of the catalyst by providing neighboring Pt sites. Yet more research needs to be done to fully understand the proposed mechanism, the simple fabrication procedures provide insight for synthesis of similar materials with outstanding properties which can be used in various new-generation electronics.

Chapter 5

Conclusions and Future Work

5.1 Summary of Contributions

Synthesis of nanostructured materials with novel performance has been essential for developing a wide range of new-generation electronics. However, complex lithography or patterning processes are involved in fabrication of nanostructured materials, which hinder the commercialization and use of these materials in practical applications. Inspired by many biological materials, the research is undertaken to design facile fabrication methods for nanostructured material and evaluate their use for various applications.

The study has identified that without using lithography or patterning process, 3-D ZnO nanostructures can be prepared using a cost-effective electrochemical method. In Chapter 2, this high density hierarchical structures are used for making an interlocked, high surface area tactile sensor which can sense pressures as low as 0.4 Pa with a response time in milliseconds. Further, the nanostructures can also detect temperature changes with a non-linear response in the 298-400 K range, which is similar to skins perception of thermal stimuli. Combining both the temperature and pressure sensitivities, the nanostructured material synthesized with a simple procedure can be of significance for applications in e-skin, adhesive and hydrophobic surfaces. Similarly, other rational combinations of nanomaterials of different morphologies can lead to enhancement of specific properties which will be of importance for applications in electrochemical devices and sensing.

In Chapter 3, the ZnO nanosheets are used as a dynamic drain of a $MAPbI_3$ film that changes its interfacing area in response to applied pressure. By studying both the ferroelectric and semiconducting properties in $MAPbI_3$, a solar-powered tactile sensor is made by interfacing ZnO nanostructure on the perovskite film. The sensor is able to operate continuously for more than 72 h after consuming 55 μW h cm^{-2} energy as the energy harvesting mechanism is decoupled from its pressure sensing mechanism. It exhibits a sensitivity of 0.57 kPa^{-1}, which can be

modulated by the strength of the poling field. The use of the ferroelectric-semiconducting nature of the $MAPbI_3$ film provides insights for development of low-cost solar-driven sensors with other similar materials.

This research has also shown that highly porous chain-like structures can be fabricated using self-assembled Au nanoparticle chains in Chapter 4. By simply adding metal cations (Pt^{4+} and Ru^{3+}) to Au nanoparticle solutions and inter-mixing the solutions at different stages of assembly, catalysts with a peak current density of 1.1 A mg_{Pt}^{-1} for EOR are synthesized. Compared to commercial Pt/C, the catalyst shows a much higher current density (3.1 times) with a less attenuation at a constant voltage and a higher CO-tolerance. Furthermore, the facile assembly process enables the control over the spatial distribution of multiple catalysts. Distinguishable domains of Pt and Ru notably increase the current density by 29 % in contrast to the homogenously mixed structure.

Overall, the research provides insights for synthesis of similar materials and contributes to existing knowledge of nanostructured materials fabrication. The findings of this research support the idea that nanostructured materials with novel properties can be synthesized using facile methods without lithography or patterning process. The ease of fabrication greatly benefits the commercialization of the nanostructured materials while keeping the unprecedented performance associated with these materials.

5.2 Future Work

As discussed in Chapter 2, more experiments need to be done to for evaluate the ability of the interlocked nanostructure to detect shear and torsion forces. In context with the practical application of tactile sensors in e-skins, shear and torsion detections are the crucial criteria and challenges for mimicking the performance of human skin. For the hierarchical ZnO structures, various responses will be generated as a result of the different changes in the current pathways under various external stimuli. Therefore, more research on differentiation between stimuli, including dynamic/static press, shear and torsion, will significantly advance the application of the electrochemically synthesized ZnO nanostructures. Furthermore, transferring the nanostructures onto or growing them directly on flexible substrates is also beneficial for the development of future wearable devices. Additionally, the temperature response of the tactile sensor needs to be further studied and modelled using known laws in order to better differentiate between pressure and temperature changes. Using similar fabrication methods, higher-order hierarchical structures of ZnO can be explored for providing more surface area which is crucial for many applications.

Regarding the self-powered tactile sensor, more research is needed to better understand the proposed mechanism for the observed ion migration effect and especially the role of O_2 adsorption and defects in perovskite materials. The phenomena of ion-migration and ferroelectric dominating were observed, but the origin of such a difference under different conditions remains unclear. 3-D ZnO nanostructures can also be interfaced on the perovskite material for higher sensitivity as complex structure induces more contact area changes upon applied pressure.

In regards to the self-assembled chains, it is suggested that further experimental investigations be undertaken for complete understanding of the cation-induced Au nanoparticle assembly. A design of experiments (DOE) is being conducting currently in the Maheshwari Lab, in which the electron density, dissociation constant, and hydrated radius of the cation linkers are altered by using different metal ions. Temperature, pH, and the extent of

agitation of the assembly process are also being studied as external parameters which will affect the assembly. Placement dependence of the bimetallic nanocomposite catalyst should also be studied systematically to understand the effect of the size and dispersion of each component. Lastly, research on the electron transfer and mass transfer on the catalyst surface using a rotating disk electrode would significantly enhance our understanding of the overall ethanol oxidation reaction mechanism.

Letter of Copyright Permission

License Number	4294090206493
License date	Feb 22, 2018
Licensed Content Publisher	John Wiley and Sons
Licensed Content Publication	Advanced Materials
Licensed Content Title	A Light Harvesting, Self-Powered Monolith Tactile Sensor Based on Electric Field Induced Effects in MAPbI3 Perovskite
Licensed Content Author	Rohit Saraf,Long Pu,Vivek Maheshwari
Licensed Content Date	Jan 15, 2018
Licensed Content Pages	1
Type of use	Dissertation/Thesis
Requestor type	Author of this Wiley article
Format	Print and electronic
Portion	Full article
Will you be translating?	No
Title of your thesis / dissertation	Nanostructured materials for tactile sensing and catalytic applications
Expected completion date	Jun 2018
Expected size (number of pages)	1
Requestor Location	Long Pu 200 University Ave W
	Waterloo, ON N2L 3G1 Canada Attn: Long Pu
Publisher Tax ID	EU826007151
Total	0.00 USD
Terms and Conditions	

References

1. Y.-G. Guo, J.-S. Hu, L.-J. Wan, *Adv. Mater.* **2008**, *20*, 2878.

2. N. Zhao, Z. Wang, C. Cai, H. Shen, F. Liang, D. Wang, C. Wang, T. Zhu, J. Guo, Y. Wang, X. Liu, C. Duan, H. Wang, Y. Mao, X. Jia, H. Dong, X. Zhang, J. Xu, *Adv. Mater.* **2014**, *26*, 6994.

3. A. S. Aricò, P. Bruce, B. Scrosati, J.-M. Tarascon, W. van Schalkwijk, *Nat. Mater.* **2005**, *4*, 366.

4. P. Fratzl, *J. R. Soc. Interface* **2007**, *4*, 637.

5. J. Peng, Q. Cheng, *Adv. Mater.* **2017**, *29*, 1702959.

6. M. A. Meyers, P.-Y. Chen, A. Y.-M. Lin, Y. Seki, *Prog. Mater. Sci.* **2008**, *53*, 1.

7. M. L. Seol, J. H. Woo, D. Il Lee, H. Im, J. Hur, Y. K. Choi, *Small* **2014**, *10*, 3887.

8. W. Barthlott, M. Mail, B. Bhushan, K. Koch, *Nano-Micro Lett.* **2017**, *9*, 23.

9. M. Darnell, D. J. Mooney, *Nat. Mater.* **2017**, *16*, 1178.

10. A. L. M. Reddy, S. R. Gowda, M. M. Shaijumon, P. M. Ajayan, *Adv. Mater.* **2012**, *24*, 5045.

11. H. Gleiter, *Acta Mater.* **2000**, *48*, 1.

12. L. Loh, S. Dunn, *J. Nanosci. Nanotechnol.* **2012**, *12*, 8215.

13. P. Y. Chen, A. Y. M. Lin, Y. S. Lin, Y. Seki, A. G. Stokes, J. Peyras, E. A. Olevsky, M. A. Meyers, J. McKittrick, *J. Mech. Behav. Biomed. Mater.* **2008**, *1*, 208.

14. J. Yu, S. Chary, S. Das, J. Tamelier, N. S. Pesika, K. L. Turner, J. N. Israelachvili, *Adv. Funct. Mater.* **2011**, *21*, 3010.

15. Y. Y. Yan, N. Gao, W. Barthlott, *Adv. Colloid Interface Sci.* **2011**, *169*, 80.

16. L. F. Boesel, C. Cremer, E. Arzt, A. Del Campo, *Adv. Mater.* **2010**, *22*, 2125.

17. P. Fratzl, R. Weinkamer, *Prog. Mater. Sci.* **2007**, *52*, 1263.

18. H. Wu, Y. Huang, F. Xu, Y. Duan, Z. Yin, *Adv. Mater.* **2016**, *28*, 9881.

19. J. Park, Y. Lee, M. Ha, S. Cho, H. Ko, *J. Mater. Chem. B* **2016**, *4*, 2999.

20. M. Ha, S. Lim, J. Park, D. S. Um, Y. Lee, H. Ko, *Adv. Funct. Mater.* **2015**, *25*, 2841.

21. F. McGlone, D. Reilly, *Neurosci. Biobehav. Rev.* **2010**, *34*, 148.

22. V. Maheshwari, R. Saraf, *Angew. Chemie Int. Ed.* **2008**, *47*, 7808.

23. W. Zeng, L. Shu, Q. Li, S. Chen, F. Wang, X. M. Tao, *Adv. Mater.* **2014**, *26*, 5310.

24. S. Gong, W. Schwalb, Y. Wang, Y. Chen, Y. Tang, J. Si, B. Shirinzadeh, W. Cheng, *Nat. Commun.* **2014**, *5*, 3132.

25. J. Park, M. Kim, Y. Lee, H. S. Lee, H. Ko, *Sci. Adv.* **2015**, *1*, e1500661.

26. S. C. B. Mannsfeld, B. C. K. Tee, R. M. Stoltenberg, C. V. H. H. Chen, S. Barman, B. V. O. Muir, A. N. Sokolov, C. Reese, Z. Bao, *Nat. Mater.* **2010**, *9*, 859.

27. L. Viry, A. Levi, M. Totaro, A. Mondini, V. Mattoli, B. Mazzolai, L. Beccai, *Adv. Mater.* **2014**, *26*, 2659.

28. K. Takei, Z. Yu, M. Zheng, H. Ota, T. Takahashi, A. Javey, *Proc. Natl. Acad. Sci. U. S. A.* **2014**, *111*, 1703.

29. J. Park, Y. Lee, J. Hong, M. Ha, Y. Do Jung, H. Lim, S. Y. Kim, H. Ko, *ACS Nano* **2014**, *8*, 4689.

30. S. Chen, Z. Lou, D. Chen, Z. Chen, K. Jiang, G. Shen, *Sci. China Mater.* **2016**, *59*, 173.

31. C. Pang, G. Y. Lee, T. Il Kim, S. M. Kim, H. N. Kim, S. H. Ahn, K. Y. Suh, *Nat. Mater.* **2012**, *11*, 795.

32. W. Zhong, Q. Liu, Y. Wu, Y. Wang, X. Qing, M. Li, K. Liu, W. Wang, D. Wang, *Nanoscale* **2016**, *8*, 12105.

33. C. Pang, T. Il Kim, W. G. Bae, D. Kang, S. M. Kim, K. Y. Suh, *Adv. Mater.* **2012**, *24*, 475.

34. H. Guo, M. H. Yeh, Y. C. Lai, Y. Zi, C. Wu, Z. Wen, C. Hu, Z. L. Wang, *ACS Nano* **2016**, *10*, 10580.

35.   A. Kołodziejczak-Radzimska, T. Jesionowski, *Materials (Basel).* **2014**, *7*, 2833.

36.   Ü. Özgür, Y. I. Alivov, C. Liu, a. Teke, M. a. Reshchikov, S. Doğan, V. Avrutin, S. J. Cho, H. Morkọ, *J. Appl. Phys.* **2005**, *98*, 1.

37.   Z. Fan, J. G. Lu, *J. Nanosci. Nanotechnol.* **2005**, *5*, 1561.

38.   A. Janotti, C. G. Van De Walle, *Reports Prog. Phys.* **2009**, *72*, 126501.

39.   M. Vaseem, A. Umar, Y. Hahn, *ZnO Nanoparticles: Growth, Properties, and Applications*, **2010**.

40.   L. Xu, Q. Chen, D. Xu, *J. Phys. Chem. C* **2007**, *111*, 11560.

41.   J. Y. Lao, J. G. Wen, Z. F. Ren, *Nano Lett.* **2002**, *2*, 1287.

42.   M. Abd-Ellah, N. Moghimi, L. Zhang, N. F. Heinig, L. Zhao, J. P. Thomas, K. T. Leung, *J. Phys. Chem. C* **2013**, *117*, 6794.

43.   J. R. Miller, P. Simon, *Science (80-.).* **2008**, *321*, 651.

44.   C. Liu, F. Li, L.-P. Ma, H.-M. Cheng, *Adv. Mater.* **2010**, *22*, E28.

45.   M. Winter, R. J. Brodd, *Chem. Rev.* **2004**, *104*, 4245.

46.   S. P. S. Badwal, S. Giddey, A. Kulkarni, J. Goel, S. Basu, *Appl. Energy* **2015**, *145*, 80.

47.   S. Sharma, B. G. Pollet, *J. Power Sources* **2012**, *208*, 96.

48.   B. C. Ong, S. K. Kamarudin, S. Basri, *Int. J. Hydrogen Energy* **2017**, *42*, 10142.

49.   M. Z. F. Kamarudin, S. K. Kamarudin, M. S. Masdar, W. R. W. Daud, *Int. J. Hydrogen Energy* **2013**, *38*, 9438.

50.   F. Vigier, C. Coutanceau, F. Hahn, E. M. Belgsir, C. Lamy, *J. Electroanal. Chem.* **2004**, *563*, 81.

51.   F. Colmati, E. Antolini, E. R. Gonzalez, *J. Power Sources* **2006**, *157*, 98.

52.   M. A. F. Akhairi, S. K. Kamarudin, *Int. J. Hydrogen Energy* **2016**, *41*, 4214.

53.   Y. Wang, S. Zou, W.-B. Cai, *Catalysts* **2015**, *5*, 1507.

54.   E. Antolini, *Energies* **2017**, *10*, 42.

55.   A. Sayadi, P. G. Pickup, *Electrochim. Acta* **2016**, *215*, 84.

56.   R. Rizo, D. Sebastián, M. J. Lázaro, E. Pastor, *Appl. Catal. B Environ.* **2017**, *200*, 246.

57.   E. . Spinacé, A. . Neto, M. Linardi, *J. Power Sources* **2004**, *129*, 121.

58.   L. Dong, R. R. S. Gari, Z. Li, M. M. Craig, S. Hou, *Carbon N. Y.* **2010**, *48*, 781.

59.   I. a. Rutkowska, P. J. Kulesza, *J. Electrochem. Soc.* **2016**, *163*, H3052.

60.   S. T. Hunt, M. Milina, A. C. Alba-Rubio, C. H. Hendon, J. A. Dumesic, Y. Roman-Leshkov, *Science (80-.).* **2016**, *352*, 974.

61.   R. W. Murray, *Chem. Rev.* **2008**, *108*, 2688.

62.   R. J. Barsotti, M. D. Vahey, R. Wartena, Y. M. Chiang, J. Voldman, F. Stellacci, *Small* **2007**, *3*, 488.

63.   K. Saha, S. Agasti, C. Kim, X. Li, V. Rotello, *Chem. Rev.* **2012**, *112*, 2739.

64.   M.-C. Daniel, D. Astruc, *Chem. Rev.* **2004**, *104*, 293.

65.   S. Zeng, K.-T. Yong, I. Roy, X.-Q. Dinh, X. Yu, F. Luan, *Plasmonics* **2011**, *6*, 491.

66.   C. Leiterer, S. Berg, A.-P. Eskelinen, A. Csaki, M. Urban, P. Törmä, W. Fritzsche, *Sensors Actuators B Chem.* **2012**, *176*, 368.

67.   L. Pu, M. Baig, V. Maheshwari, *Anal. Bioanal. Chem.* **2016**, *408*, 2697.

68.   L. Pu, A. S. Abbas, V. Maheshwari, *Adv. Mater.* **2014**, *26*, 6491.

69.   A. R. Bielinski, M. Boban, Y. He, E. Kazyak, D. H. Lee, C. Wang, A. Tuteja, N. P. Dasgupta, *ACS Nano* **2017**, *11*, 478.

70.   M. Ge, C. Cao, J. Huang, S. Li, Z. Chen, K.-Q. Zhang, S. S. Al-Deyab, Y. Lai, *J. Mater. Chem. A* **2016**, *4*, 6772.

71.   W. J. Crookes-Goodson, J. M. Slocik, R. R. Naik, *Chem. Soc. Rev.* **2008**, *37*, 2403.

72.   B. Liu, J. Zhang, X. Wang, G. Chen, D. Chen, C. Zhou, G. Shen, *Nano Lett.* **2012**, *12*, 3005.

73.   K. Luo, M. R. Roberts, R. Hao, N. Guerrini, E. Liberti, C. S. Allen, A. I. Kirkland, P. G. Bruce, *Nano Lett.* **2016**, *16*, 7503.

74.   J. Cheng, Y. Lu, K. Qiu, H. Yan, J. Xu, L. Han, X. Liu, J. Luo, J.-K. Kim, Y. Luo, *Sci. Rep.* **2015**, *5*, 12099.

75.   W.-Q. Wu, H.-S. Rao, Y.-F. Xu, Y.-F. Wang, C.-Y. Su, D.-B. Kuang, *Sci. Rep.* **2013**, *3*, 1892.

76.   Z. Zheng, W. Xie, Z. S. Lim, L. You, J. Wang, *Sci. Rep.* **2015**, *4*, 5721.

77.   C. X. Guo, C. M. Li, *Energy Environ. Sci.* **2011**, *4*, 4504.

78.   S. Bag, C. R. Raj, *J. Mater. Chem. A* **2016**, *4*, 587.

79.   D. Brodoceanu, C. T. Bauer, E. Kroner, E. Arzt, T. Kraus, *Bioinspiration Biomim.* **2016**, *11*, 51001.

80.   K. Autumn, Y. A. Liang, S. T. Hsieh, W. Zesch, W. P. Chan, T. W. Kenny, R. Fearing, R. J. Full, *Nature* **2000**, *405*, 681.

81.   L. Feng, S. Li, Y. Li, H. Li, L. Zhang, J. Zhai, Y. Song, B. Liu, L. Jiang, D. Zhu, *Adv. Mater.* **2002**, *14*, 1857.

82.   R. Blossey, *Nat. Mater.* **2003**, *2*, 301.

83.   Y. Tomoyasu, Y. Arakane, K. J. Kramer, R. E. Denell, *Curr. Biol.* **2009**, *19*, 2057.

84.   J. Sun, B. Bhushan, *RSC Adv.* **2012**, *2*, 7617.

85.   S. N. Gorb, *Int. J. Insect Morphol. Embryol.* **1998**, *27*, 205.

86.   J. Kim, M. Lee, H. J. Shim, R. Ghaffari, H. R. Cho, D. Son, Y. H. Jung, M. Soh, C. Choi, S. Jung, K. Chu, D. Jeon, S.-T. Lee, J. H. Kim, S. H. Choi, T. Hyeon, D.-H. Kim, *Nat. Commun.* **2014**, *5*, 5747.

87.   R. S. Dahiya, G. Metta, M. Valle, G. Sandini, *IEEE Trans. Robot.* **2010**, *26*, 1.

88.   C. M. Mate, R. W. Carpick, *Nature* **2011**, *480*, 189.

89.   B. U. Hwang, J. H. Lee, T. Q. Trung, E. Roh, D. Il Kim, S. W. Kim, N. E. Lee, *ACS Nano* **2015**, *9*, 8801.

90.   X. Wang, Y. Gu, Z. Xiong, Z. Cui, T. Zhang, *Adv. Mater.* **2014**, *26*, 1336.

91.   S. Y. Kim, S. Park, H. W. Park, D. H. Park, Y. Jeong, D. H. Kim, *Adv. Mater.* **2015**, *27*, 4178.

92.   I. Kang, M. J. Schulz, J. H. Kim, V. Shanov, D. Shi, *Smart Mater. Struct.* **2006**, *15*, 737.

93.   Y. Wang, L. Wang, T. Yang, X. Li, X. Zang, M. Zhu, K. Wang, D. Wu, H. Zhu, *Adv. Funct. Mater.* **2014**, *24*, 4666.

94.   H. Bin Yao, J. Ge, C. F. Wang, X. Wang, W. Hu, Z. J. Zheng, Y. Ni, S. H. Yu, *Adv. Mater.* **2013**, *25*, 6692.

95.   D. J. Lipomi, M. Vosgueritchian, B. C. K. Tee, S. L. Hellstrom, J. A. Lee, C. H. Fox, Z. Bao, *Nat. Nanotechnol.* **2011**, *6*, 788.

96.   L. Pan, A. Chortos, G. Yu, Y. Wang, S. Isaacson, R. Allen, Y. Shi, R. Dauskardt, Z. Bao, *Nat. Commun.* **2014**, *5*, 3002.

97.   S. Kirkpatrick, *Rev. Mod. Phys.* **1973**, *45*, 574.

98.   Z. Lou, S. Chen, L. Wang, K. Jiang, G. Shen, *Nano Energy* **2016**, *23*, 7.

99.   P. J. Dyck, I. R. Zimmerman, D. M. Johnson, D. Gillen, J. L. Hokanson, J. L. Karnes, G. Gruener, P. C. O'Brien, *J. Neurol. Sci.* **1996**, *136*, 54.

100.   Y. J. Zhu, T. J. Lu, *Philos. Trans. R. Soc. A Math. Phys. Eng. Sci.* **2010**, *368*, 521.

101.   D. Pradhan, K. T. Leung, *Langmuir* **2008**, *24*, 9707.

102.   S. I. White, R. M. Mutiso, P. M. Vora, D. Jahnke, S. Hsu, J. M. Kikkawa, J. Li, J. E. Fischer, K. I. Winey, *Adv. Funct. Mater.* **2010**, *20*, 2709.

103.   N. Sato, K. Machida, H. Morimura, S. Shigematsu, K. Kudou, M. Yano, H. Kyuragi, *IEEE Trans. Electron Devices* **2003**, *50*, 1109.

104.   H. Tian, Y. Shu, X. F. Wang, M. A. Mohammad, Z. Bie, Q. Y. Xie, C. Li, W. T. Mi, Y. Yang, T. L. Ren, *Sci. Rep.* **2015**, *5*, 8603.

105.   Q. Sun, D. H. Kim, S. S. Park, N. Y. Lee, Y. Zhang, J. H. Lee, K. Cho, J. H. Cho, *Adv. Mater.* **2014**, *26*, 4735.

106.   Q. H. Li, Q. Wan, Y. X. Liang, T. H. Wang, *Appl. Phys. Lett.* **2004**, *84*, 4556.

107.   Y. W. Heo, D. P. Norton, L. C. Tien, Y. Kwon, B. S. Kang, F. Ren, S. J. Pearton, J. R. Laroche, *Mater. Sci. Eng. R Reports* **2004**, *47*, 1.

108.   M. Liu, Y. Pang, B. Zhang, P. De Luna, O. Voznyy, J. Xu, X. Zheng, C. T. Dinh, F. Fan, C. Cao, F. P. G. De Arquer, T. S. Safaei, A. Mepham, A. Klinkova, E. Kumacheva, T. Filleter, D. Sinton, S. O. Kelley, E. H. Sargent, *Nature* **2016**, *537*, 382.

109.   Y. Zi, L. Lin, J. Wang, S. Wang, J. Chen, X. Fan, P. K. Yang, F. Yi, Z. L. Wang, *Adv. Mater.* **2015**, *27*, 2340.

110. Y. C. Mao, P. Zhao, G. McConohy, H. Yang, Y. X. Tong, X. D. Wang, *Adv. Energy Mater.* **2014**, *4*, 1301624.

111. Y. Yang, H. Zhang, Z.-H. Lin, Y. S. Zhou, Q. Jing, Y. Su, J. Yang, J. Chen, C. Hu, Z. L. Wang, *ACS Nano* **2013**, *7*, 9213.

112. L. Lin, Y. Xie, S. Wang, W. Wu, S. Niu, X. Wen, Z. L. Wang, *ACS Nano* **2013**, *7*, 8266.

113. G. Zhu, W. Q. Yang, T. Zhang, Q. Jing, J. Chen, Y. S. Zhou, P. Bai, Z. L. Wang, *Nano Lett.* **2014**, *14*, 3208.

114. G. Hodes, *Science* **2013**, *342*, 317.

115. M. M. Lee, J. Teuscher, T. Miyasaka, T. N. Murakami, H. J. Snaith, *Science* **2012**, *338*, 643.

116. N. G. Park, J. Phys. *Chem. Lett.* **2013**, 4, 2423.

117. J. Burschka, N. Pellet, S. J. Moon, R. Humphry-Baker, P. Gao, M. K. Nazeeruddin, M. Grätzel, *Nature* **2013**, *499*, 316.

118. Y. Rakita, O. Bar-Elli, E. Meirzadeh, H. Kaslasi, Y. Peleg, G. Hodes, I. Lubomirsky, D. Oron, D. Ehre, D. Cahen, *Proc. Natl. Acad. Sci. U.S.A.* **2017**, *114*, E5504.

119. A. Stroppa, C. Quarti, F. De Angelis, S. Picozzi, *J. Phys. Chem. Lett.* **2015**, *6*, 2223.

120. Y. Kutes, L. Ye, Y. Zhou, S. Pang, B. D. Huey, N. P. Padture, *J. Phys. Chem. Lett.* **2014**, *5*, 3335.

121. J. You, L. Meng, T. B. Song, T. F. Guo, Y. M. Yang, W. H. Chang, Z. Hong, H. Chen, H. Zhou, Q. Chen, *Nat. Nanotechnol.* **2016**, *11*, 75.

122. J. B. Han, F. R. Fan, C. Xu, S. S. Lin, M. Wei, X. Duan, Z. L. Wang, *Nanotechnology* **2010**, *21*, 405203.

123. W. Peng, R. Yu, X. Wang, Z. Wang, H. Zou, Y. He, Z. L. Wang, *Nano Res.* **2016**, *9*, 3695.

124. Z. Xiao, Y. Yuan, Y. Shao, Q. Wang, Q. Dong, C. Bi, P. Sharma, A. Gruverman, J. Huang, *Nat. Mater.* **2015**, *14*, 193.

125.   Y. Yuan, T. Li, Q. Wang, J. Xing, A. Gruverman, J. Huang, *Sci. Adv.* **2017**, *3*, e1602164.

126.   Y. Yuan, J. Chae, Y. Shao, Q. Wang, Z. Xiao, A. Centrone, J. Huang, *Adv. Energy Mater.* **2015**, *5*, 1500615.

127.   Q. Wang, Y. Shao, H. Xie, L. Lyu, X. Liu, Y. Gao, J. Huang, *Appl. Phys. Lett.* **2014**, *105*, 163508.

128.   S. Liu, F. Zheng, I. Grinberg, A. M. Rappe, *J. Phys. Chem. Lett.* **2016**, *7*, 1460.

129.   C. Quarti, F. Mosconi, F. De Angelis, *Chem. Mater.* **2014**, *26*, 6557.

130.   Y. Yuan, T. J. Reece, P. Sharma, S. Poddar, S. Ducharme, A. Gruverman, Y. Yang, J. Huang, *Nat. Mater.* **2011**, *10*, 296.

131.   S. Y. Yang, J. Seidel, S. J. Byrnes, P. Shafer, C. H. Yang, M. D. Rossell, P. Yu, Y. H. Chu, J. F. Scott, J. W. Ager, L. W. Martin, R. Ramesh, *Nat. Nanotechnol.* **2010**, *5*, 143.

132.   H. W. Chen, N. Sakai, M. Ikegami, T. Miyasaka, *J. Phys. Chem. Lett.* **2014**, *6*, 164.

133.   Y. Yuan, Z. Xiao, B. Yang, J. Huang, *J. Mater. Chem. A* **2014**, *2*, 6027.

134.   H. S. Kim, I. Mora-Sero, V. Gonzalez-Pedro, F. Fabregat-Santiago, E. J. Juarez-Perez, N. G. Park, J. Bisquert, *Nat. Commun.* **2013**, *4*, 2242.

135.   K. Mahmood, B. S. Swain, A. Amassian, *Nanoscale* **2014**, *6*, 14674.

136.   J. Zhang, P. Barboux, T. Pauporté, *Adv. Energy Mater.* **2014**, *4*, 1400932.

137.   K. Takei, T. Takahashi, J. C. Ho, H. Ko, A. G. Gillies, P. W. Leu, R. S. Fearing, A. Javey, *Nat. Mater.* **2010**, *9*, 821.

138.   C. Wang, D. Hwang, Z. Yu, K. Takei, J. Park, T. Chen, B. Ma, A. Javey, *Nat. Mater.* **2013**, *12*, 899.

139.   M. Kaltenbrunner, T. Sekitani, J. Reeder, T. Yokota, K. Kuribara, T. Tokuhara, M. Drack, R. Schwodiauer, I. Graz, S. Bauer-Gogonea, S. Bauer, T. Someya, *Nature* **2013**, *499*, 458.

140.   W. Wu, X. Wen, Z. L. Wang, *Science* **2013**, *340*, 952.

141.   J. H. Im, C. R. Lee, J. W. Lee, S. W. Park, N. G. Park, *Nanoscale* **2011**, *3*, 4088.

142.   R. R. Mehta, B. D. Silverman, J. T. Jacobs, *J. Appl. Phys.* **1973**, *44*, 3379.

143.   Y. C. Zhao, W. K. Zhou, X. Zhou, K. H. Liu, D. P. Yu, Q. Zhao, *Light Sci. Appl.* **2017**, *6*, e16243.

144.   T. Baikie, Y. Fang, J. M. Kadro, M. Schreyer, F. Wei, S. G. Mhaisalkar, M. Graetzel, T. J. White, *J. Mater. Chem. A* **2013**, *1*, 5628.

145.   C. C. Stoumpos, C. D. Malliakas, M. G. Kanatzidis, *Inorg. Chem.* **2013**, *52*, 9019.

146.   J. Mizusaki, K. Arai, K. Fueki, *Solid State Ionics* **1983**, *11*, 203.

147.   X. Wang, B. Liu, R. Liu, Q. Wang, X. Hou, D. Chen, R. Wang, G. Shen, *Angew. Chem.* **2014**, *126*, 1880.

148.   M. Bass, P. A. Franken, J. F. Ward, G. Weinreich, *Phys. Rev. Lett.* **1962**, *9*, 446.

149.   A. Rice, Y. Jin, X. F. Ma, X. C. Zhang, D. Bliss, J. Larkin, M. Alexander, *Appl. Phys. Lett.* **1994**, *64*, 1324.

150.   M. T. Weller, O. J. Weber, P. F. Henry, A. M. Di Pumpo, T. C. Hansen, *Chem. Commun.* **2015**, *51*, 4180.

151.   E. Edri, S. Kirmayer, A. Henning, S. Mukhopadhyay, K. Gartsman, Y. Rosenwaks, G. Hodes, D. Cahen, *Nano Lett.* **2014**, *14*, 1000.

152.   L. Pu, R. Saraf, V. Maheshwari, *Sci. Rep.* **2017**, *7*, 5834.

153.   I. Graz, M. Krause, S. Bauer-Gogonea, S. Bauer, S. P. Lacour, B. Ploss, M. Zirkl, B. Stadlober, S. Wagner, *J. Appl. Phys.* **2009**, *106*, 034503.

154.   G. Schwartz, B. C. K. Tee, J. Mei, A. L. Appleton, D. H. Kim, H. Wang, Z. Bao, *Nat. Commun.* **2013**, *4*, 1859.

155.　 C. G. Núñez, W. T. Navaraj, E. O. Polat, R. Dahiya, *Adv. Funct. Mater.* **2017**, *27*, 1606287.

156.　 F. Meng, Y. Ding, *Adv. Mater.* **2011**, *23*, 4098.

157.　 Z. Jusys, J. Kaiser, R. J. Behm, *Electrochim. Acta* **2002**, *47*, 3693.

158.　 C. Xu, L. Wang, X. Mu, Y. Ding, *Langmuir* **2010**, *26*, 7437.

159.　 M. K. Min, J. Cho, K. Cho, H. Kim, *Electrochim. Acta* **2000**, *45*, 4211.

160.　 L. Chen, L. Lu, H. Zhu, Y. Chen, Y. Huang, Y. Li, L. Wang, *Nat. Commun.* **2017**, *8*, 14136.

161.　 M. Shao, Q. Chang, J.-P. Dodelet, R. Chenitz, *Chem. Rev.* **2016**, *116*, 3594.

162.　 M. J. Lee, J. S. Kang, Y. S. Kang, D. Y. Chung, H. Shin, C.-Y. Ahn, S. Park, M.-J. Kim, S. Kim, K.-S. Lee, Y.-E. Sung, *ACS Catal.* **2016**, *6*, 2398.

163.　 C. Du, X. Gao, Z. Zhuang, C. Cheng, F. Zheng, X. Li, W. Chen, *Electrochim. Acta* **2017**, *238*, 263.

164.　 U. A. Paulus, A. Wokaun, G. G. Scherer, T. J. Schmidt, V. Stamenkovic, N. M. Markovic, P. N. Ross, *Electrochim. Acta* **2002**, *47*, 3787.

165.　 A. Tabet-Aoul, H. Wang, Y. Wang, M. Mohamedi, *J. Electrochem. Soc.* **2017**, *164*, 685.

166.　 J. N. Israelachvili, *Intermolecular and Surface Forces.*, Academic Press Inc., **1985**.

167.　 R. P. Sear, *J. Phys. Condens. Matter* **2007**, *19*, 33101.

168.　 W. Vielstich, A. Lamm, H. A. Gasteiger, H. Yokokawa, *Handbook of Fuel Cells: Fundamentals, Technology, and Applications*, Wiley, **2003**.

169.　 A. J. Bard, L. R. Faulkner, *Electrochemical Methods: Fundamentals and Applications*, Wiley, **2001**.

170.　 P. Ochal, J. L. Gomez de la Fuente, M. Tsypkin, F. Seland, S. Sunde, N. Muthuswamy, M. Rønning, D. Chen, S. Garcia, S. Alayoglu, B. Eichhorn, *J. Electroanal. Chem.* **2011**, *655*, 140.

171.   V. Comignani, J. M. Sieben, M. E. Brigante, M. M. E. Duarte, *J. Power Sources* **2015**, *278*, 119.

172.   Y. Shen, K. Xiao, J. Xi, X. Qiu, *J. Power Sources* **2015**, *278*, 235.

173.   P. Wang, Y. Wen, S. Yin, N. Wang, P. K. Shen, *Int. J. Hydrogen Energy* **2017**, *42*, 24689.

174.   Y. Hu, A. Zhu, Q. Zhang, Q. Liu, *Int. J. Hydrogen Energy* **2016**, *41*, 11359.

175.   Y. Shen, B. Gong, K. Xiao, L. Wang, *ACS Appl. Mater. Interfaces* **2017**, *9*, 3535.

176.   B. Gurau, R. Viswanathan, R. Liu, T. J. Lafrenz, K. L. Ley, E. S. Smotkin, E. Reddington, A. Sapienza, B. C. Chan, T. E. Mallouk, S. Sarangapani, *J. Phys. Chem. B* **1998**, *102*, 9997.

177.   Z. Peng, H. Yang, *Nano Today* **2009**, *4*, 143.

178.   X. Liu, Y. Zhang, M. Gong, Y. Tang, T. Lu, Y. Chen, J.-M. Lee, *J. Mater. Chem. A* **2014**, *2*, 13840.

179.   T. Iwasita, *Electrochim. Acta* **2002**, *47*, 3663.

180.   B. Du, Y. Tong, *J. Phys. Chem. B* **2005**, *109*, 17775.

Appendix
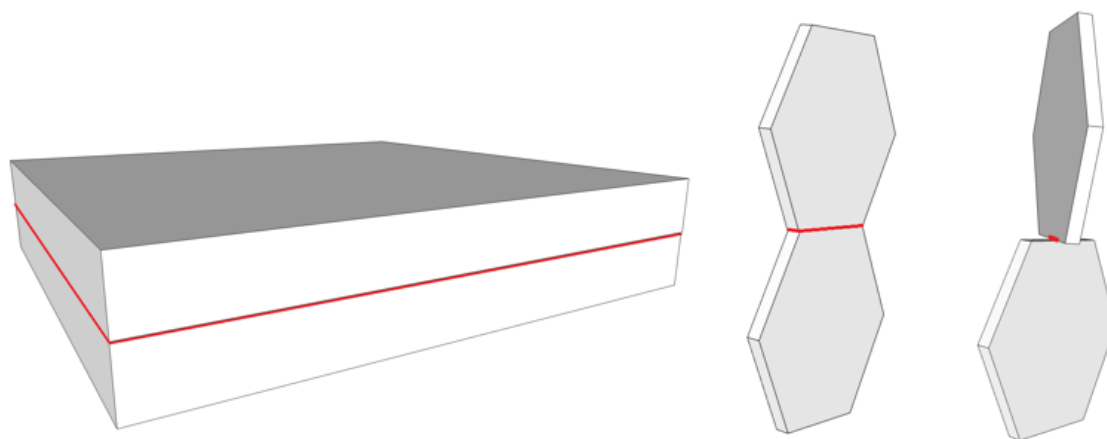
Figure A2.1. A schematic of how the ZnO structure intensifies the applied pressure at the contact points (contact area is noted by the red line).
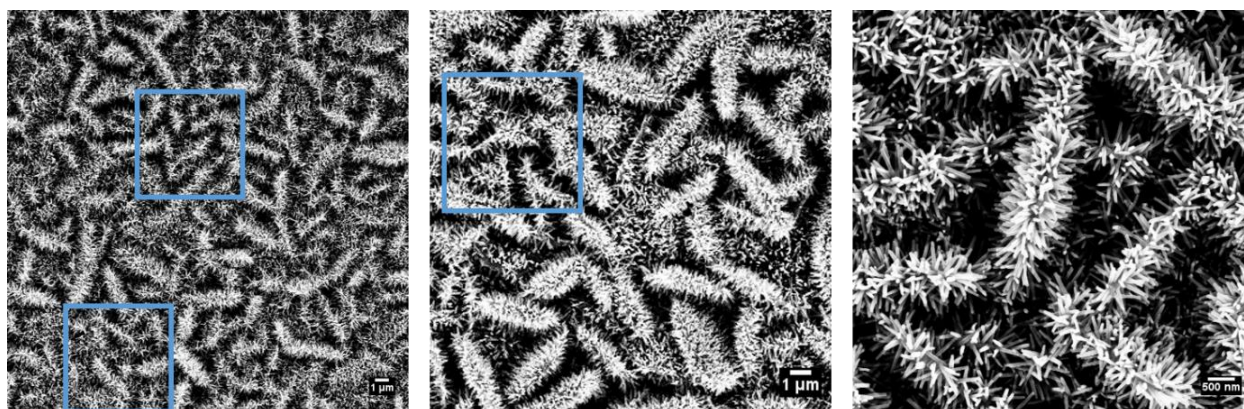
Figure A2.2. FESEM images of ZnO nanostructure at different magnifications (5 µm by 5 µm areas are denoted in blue squares).

By analyzing the FESEM images, the average diameter of ZnO nanosheets was measured to be around 3 µm with an average thickness of around 100 nm. In a typical 5 µm by 5 µm area, there are approximately 9-12 nanosheets which cover 10.8-14.4% of the total area. The decrease in contact area will increase the pressure experienced by the sheets edges by 7-9 times. The random orientation of nanosheets also plays an important role by further decreasing the contact area to a very small fraction on the edge, eventually increasing the effective pressure.
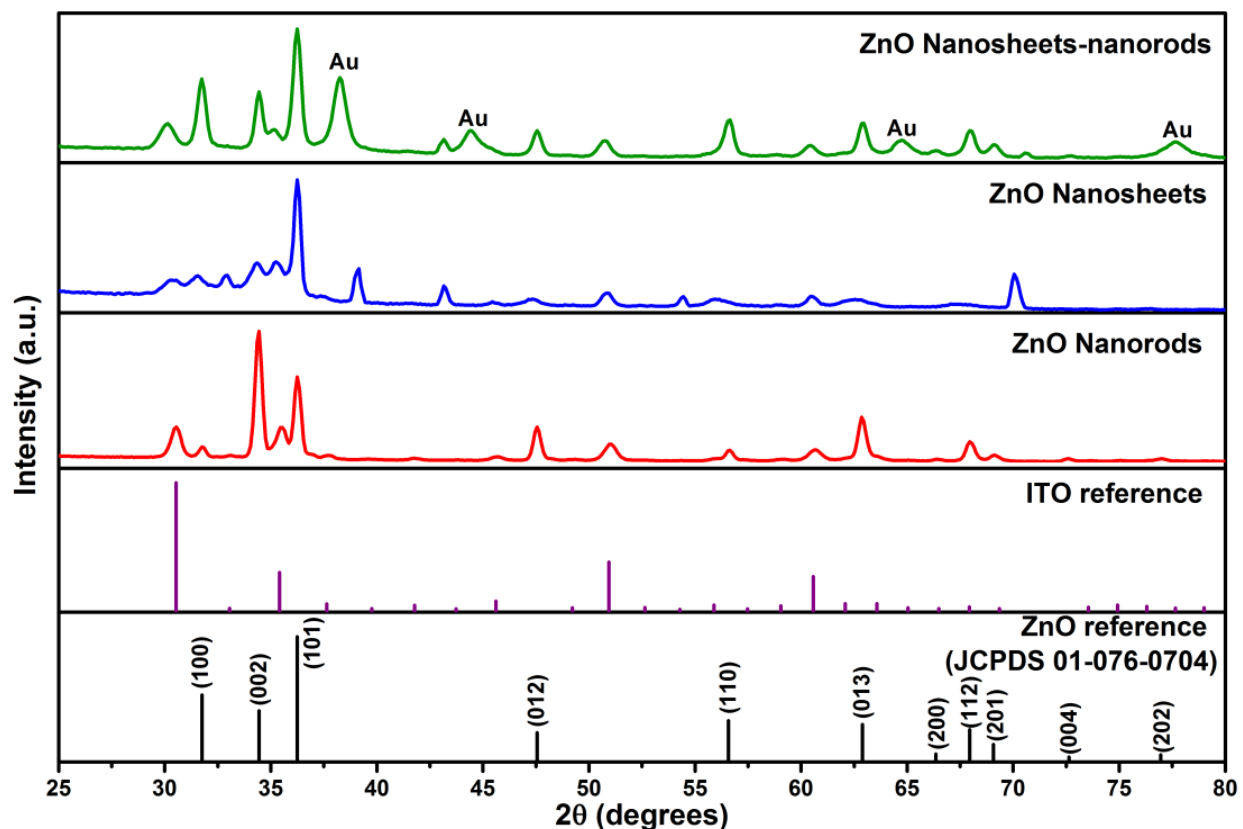
Figure A2.3. GIXRD patterns of ZnO nanorods, nanosheets, and nanosheets-nanorods, along with the standard ITO glass substrate and a powder ZnO reference sample.

Figure A2.3 shows the intense XRD peaks from the ZnO and the weaker diffraction features due to the ITO substrate. These XRD features are consistent with the hexagonal wurzite structure in the reference pattern for ZnO powder (JCPDS 01-076-0704). In particular, the features at 31.7°, 34.4°, and 36.2° are assigned, respectively, to the ZnO (100), (002), and (101) planes, consistent with the most prominent XRD features in the reference powder spectrum. Among the three aforementioned ZnO features, the diffraction in (002) [or (0001)] plane is strongest for the nanorods, while the (101) [or (10$\bar{1}$0)] plane is dominating for the nanosheets. The diffraction features from the (100), (002), and (101) planes indicating the preferential growth directions of ZnO nanosheets-nanorods.
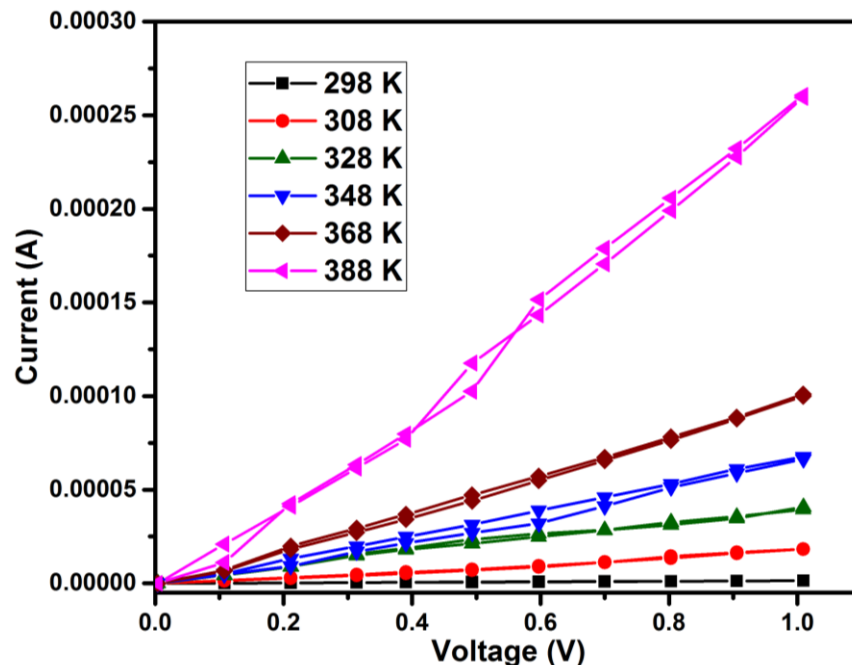
Figure A2.4. Current-voltage curves of ZnO hierarchical sensor at different temperatures.

Elements	Atomic %
O	51.11
Zn	35.35
Mn	8.72
Au	1.83
Si	2.99

Lsec: 30.0 0 Cnts 0.000 keV Det: Apollo XL-SDD Det
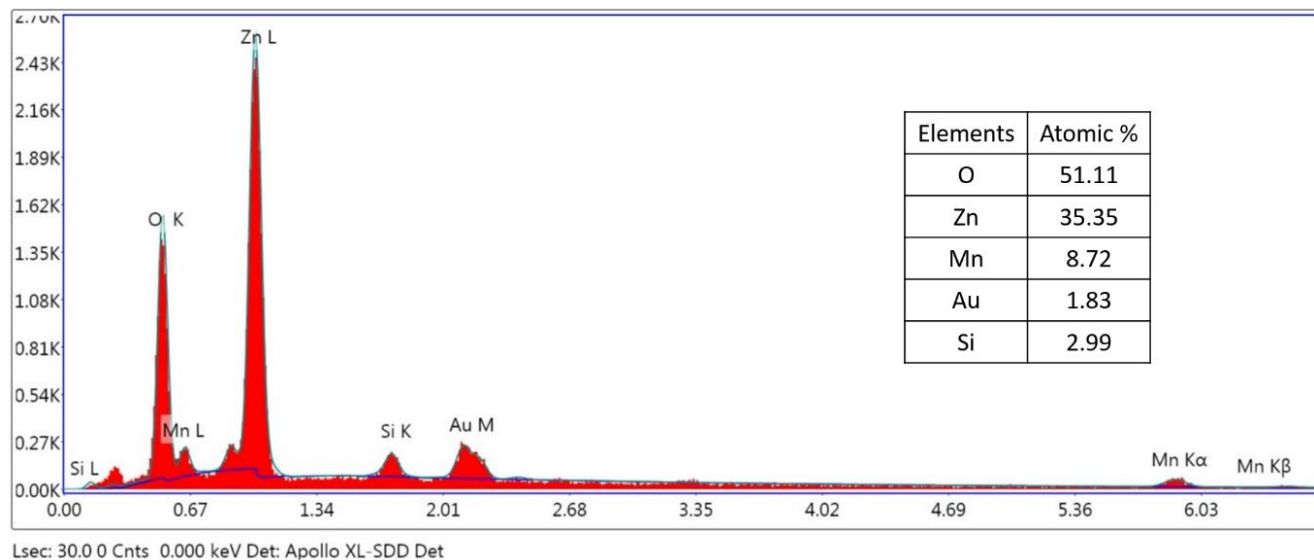
Figure A2.5. EDX spectrum and elemental composition of electrochemically deposited MnO_2 layer on ZnO structure.

EDX spectrum shows the presence of Zn, O, Mn, Au, and Si elements, the Si peak is due to the silicon detector. The sample possesses good stoichiometry in agreement with the chemical composition of the respective elements.
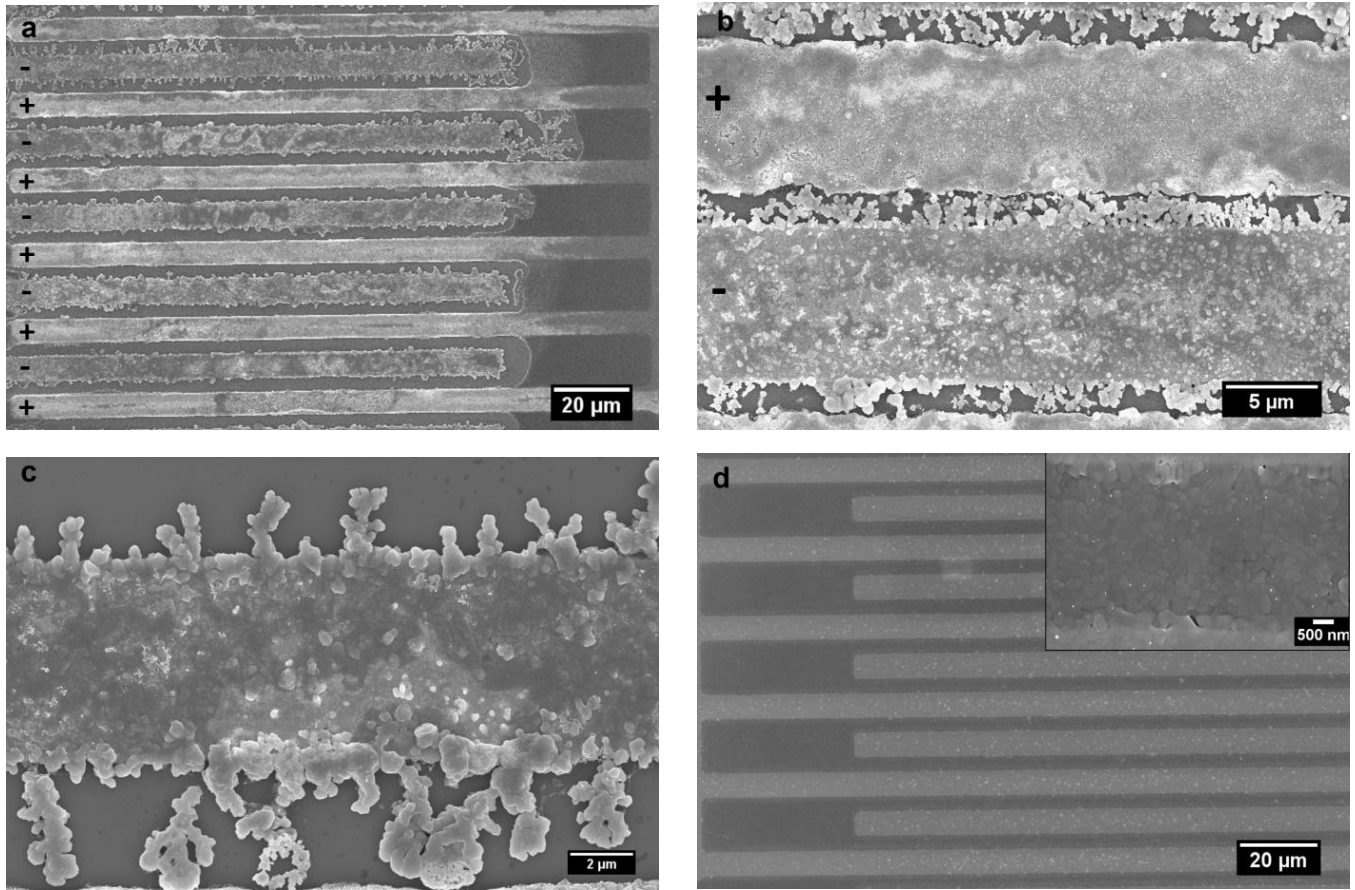
Figure A3.1. FESEM images of MAPbI$_3$ film after high poling field. (a-c) After poling at 5 V µm^{-1} for 5 min in air under light illumination showing the segregation of the ions which leads to formation of PbI$_2$ and the observed ferroelectric behavior disappears. (d) After poling at 5 V µm^{-1} for 5 min under N$_2$ in dark condition showing no change in the material.
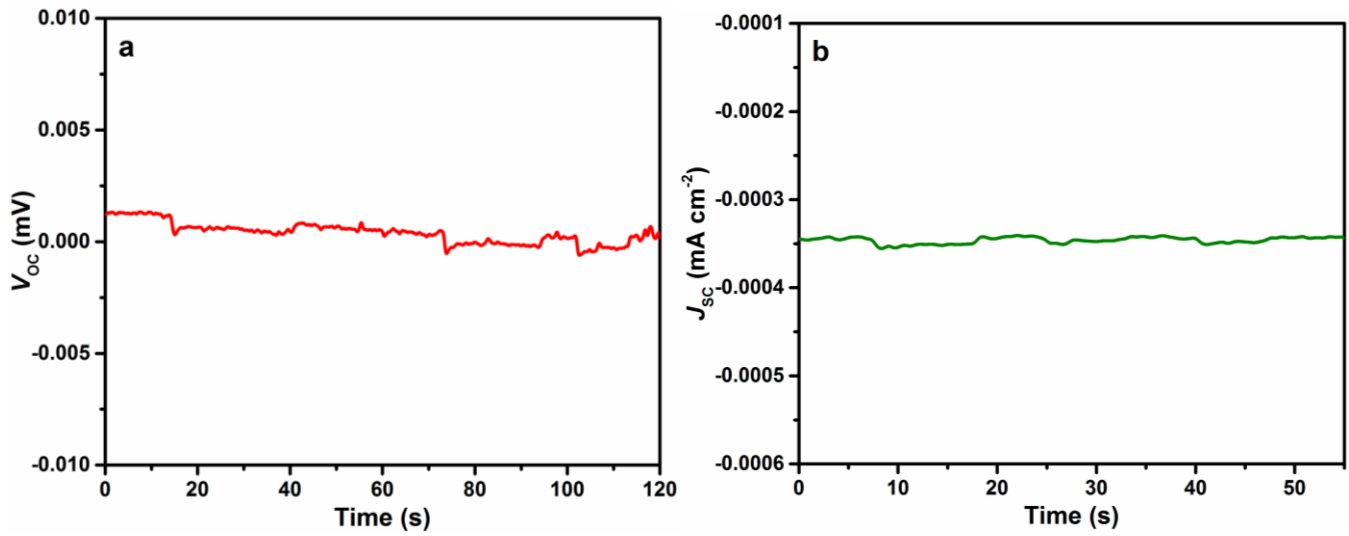
Figure A3.2. Effect of high poling field on the ferroelectric behavior. (a) V_{OC} and (b) J_{SC} disappeared after poling at 5 V μm^{-1} for 5 min in air under light illumination due to the complete separation of the ions which will lead to formation of PbI$_2$.
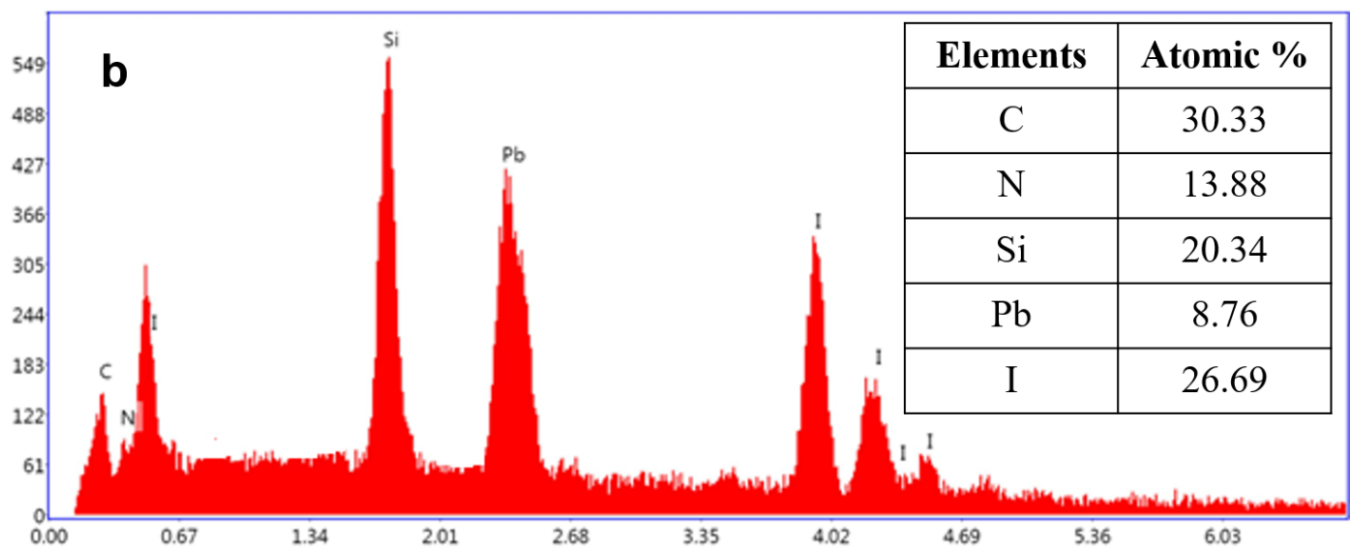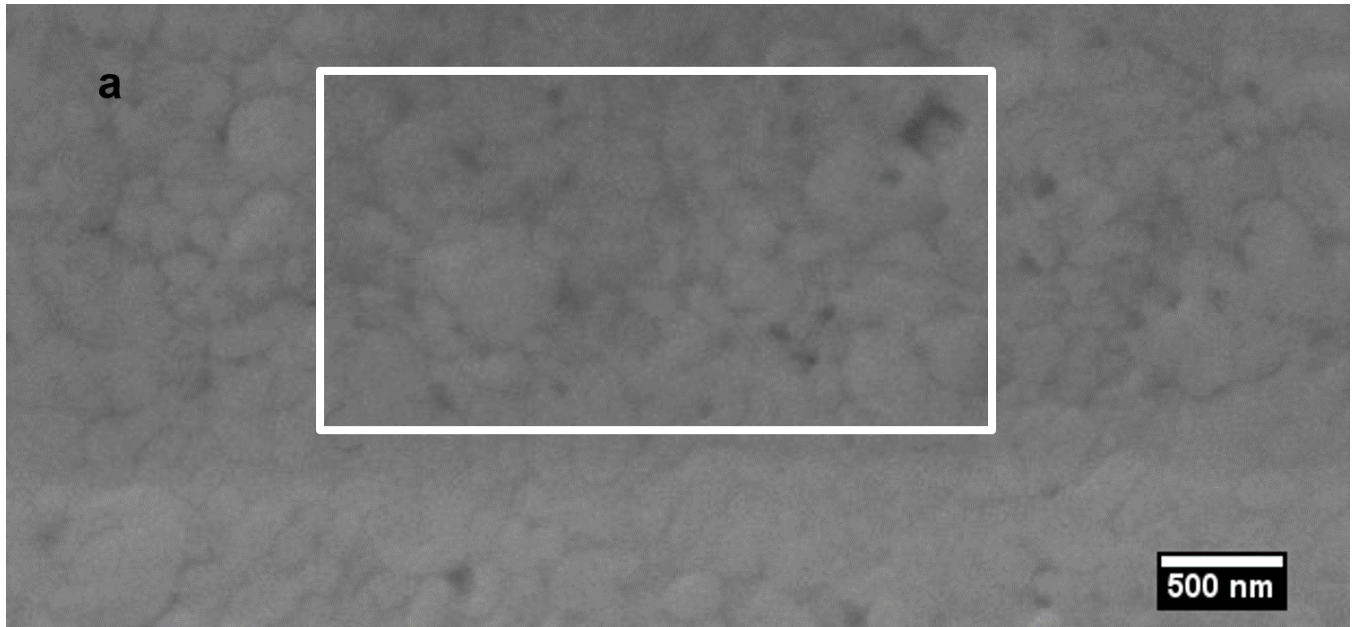
Figure A3.3. (a) FESEM image of MAPbI$_3$ film after the poling process. (b) EDX spectrum and elemental composition of the selected area showing no electrode migration.

The characterization of the device is conducted in FESEM after multiple cycles of measurements. From the elemental analysis, we can see that no Au migration is observed in the perovskite layer. This is consistent with the reports that the presence of a Cr adhesion layer with Au electrodes and restricting the device operation to room temperature limits Au migration.
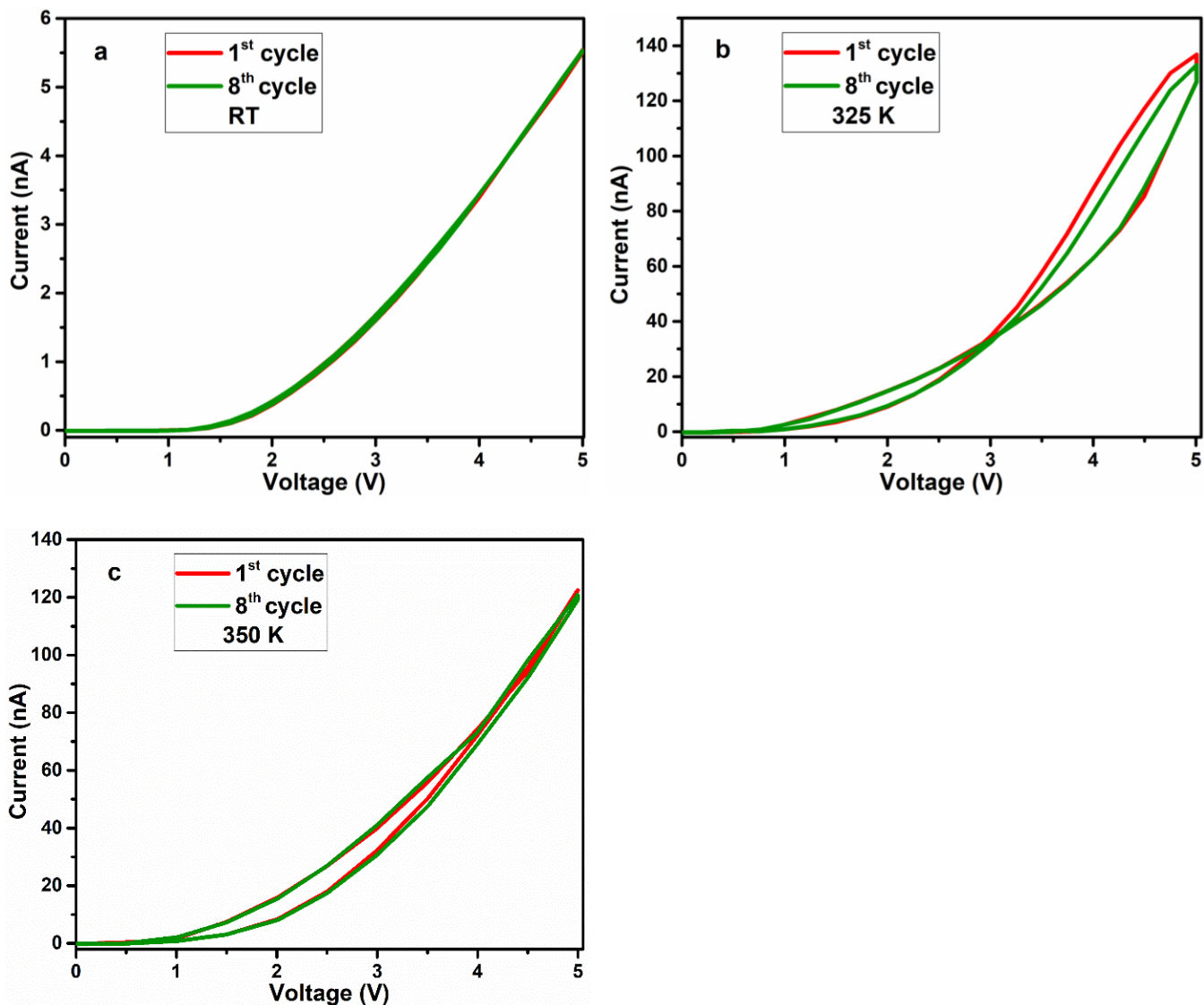
Figure A3.4. Current-voltage (*I-V*) scans from 0-5 V at (a) room temperature (RT), (b) 325 K and (c) 350 K.

The stability of the perovskite layer against any redox reactions within the voltage ranges used in the device operation is characterized in multiple ways. First multiple cycles of *I-V* are conducted by going up and down in voltage. Degradation of the perovskite due to a redox reaction leads to the possible formation of PbI_2, an insulator, with oxidation of iodide ions to I_2 (g), reaction detailed below. As seen in Figure A3.4a, the current voltage characteristics remain consistent which shows that no degradation of the perovskite layer is occurring. Further, we do not observe any hysteresis between going up and down in voltage which indicative of the capacitive behavior due to the ion diffusion current and corresponding electric field, illustrates that these effects are minimal at the

90

applied conditions in this device. The hysteresis in current voltage characteristics is observed only at higher temperatures (325 and 350 K), as seen in Figure A3.4b,c. This ion separation leads to the development of an opposing internal field and a charge compensating layer in the material similar to a capacitive response. The CV analysis present in the next section further shows that the capacitive response from the device is minimal at room temperature and redox reaction are not observed at these conditions.
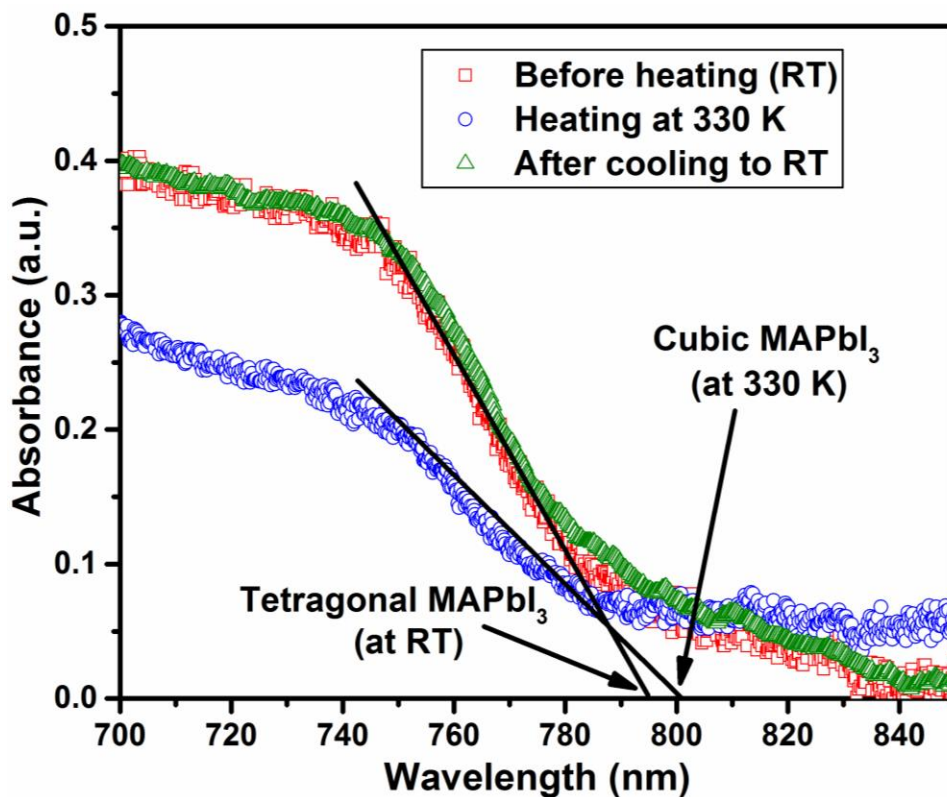
Figure A3.5. UV-Visible absorption spectrum of MAPbI$_3$ film at room temperature (RT), 330 K, and after cooling to RT.

It is known that tetragonal phase of MAPbI$_3$ is stable at room temperature (~ 296 K) and it undergoes transformation from tetragonal to the cubic phase at 327 K. The UV-Vis absorption spectrum of a tetragonal MAPbI$_3$ presents a steep absorption edge at 794 nm. The optical band gap energy (E_g) was calculated by Planck relation, $E = hc/\lambda$ where h is Planck constant (6.626×10^{-34} J.s), c is speed of light (3×10^8 m s^{-1}), and λ is the cut off wavelength. The extrapolation gives band gap value of 1.562 eV for a tetragonal MAPbI$_3$. After heating the MAPbI$_3$ film at 330 K, the cubic MAPbI$_3$ shows an absorption edge at 800 nm with a band gap of 1.55 eV. Further, the band gap is restored on cooling the film back to room temperature. This confirms that there is a phase transition from tetragonal to cubic, when the MAPbI$_3$ film is heated at 330 K.
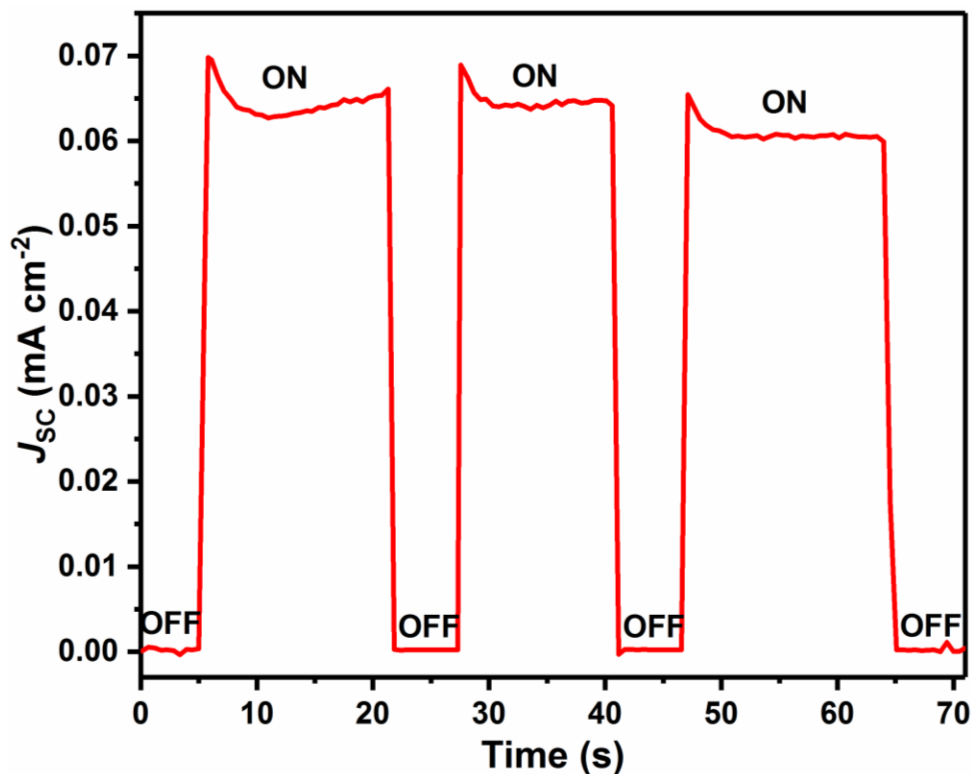
Figure A3.6. J_{SC} response showing no observable ion back diffusion current in dark. OFF refers to J_{SC} measured under dark and ON refers to J_{SC} measured under 1.0 sun illumination.

The short circuit current density (J_{SC}) response is shown for a typical device poled under the p-n conditions. As seen in Figure A3.6, we note that under dark no observable J_{SC} is recorded, which illustrates the absence of any ion back diffusion current, hence correspondingly there cannot be any internal electric field due to ion separation. On illuminating the sample, a significant J_{SC} is observed which indicates that the photo generated electron-hole pairs are being separated in the poled sample hence there is an internal electric field present in the sample and should be the result of the formation of internal p-n junction from electric field induced poling. It should be noted that an unpoled perovskite film does not show any J_{SC} on illumination.

Redox reaction in the perovskite layer

Anode process:

$$2\,(PbI_2)^*I^- \rightarrow 2\,PbI_2 + I_2 + 2\,e^- \tag{A3.1}$$

Cathode process:

$$2\,(CH_3NH_2)^*H^+ + 2\,e^- \rightarrow H_2 + 2\,CH_3NH_2 \tag{A3.2}$$

Overall reaction:

$$2\,CH_3NH_3PbI_3 \xrightarrow{electrolysis} I_2 + H_2 + 2\,PbI_2 + 2\,CH_3NH_2 \tag{A3.3}$$
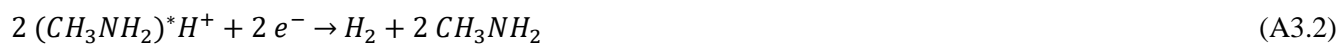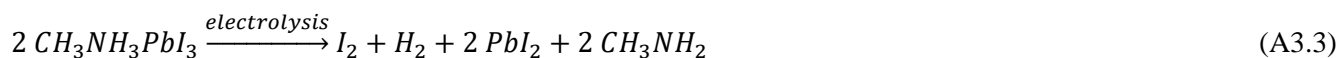
The degradation of the perovskite layer as illustrated by the equations above has been reported. As with any redox active species such oxidation and/or reduction reactions occurs only above an energy threshold that will enable an electron transfer between the redox active species and the electrode. The occurrence of the redox reaction is hence dependent on the applied bias to the electrode where the reaction occurs (working electrode in electrochemical terms) and also the temperature.
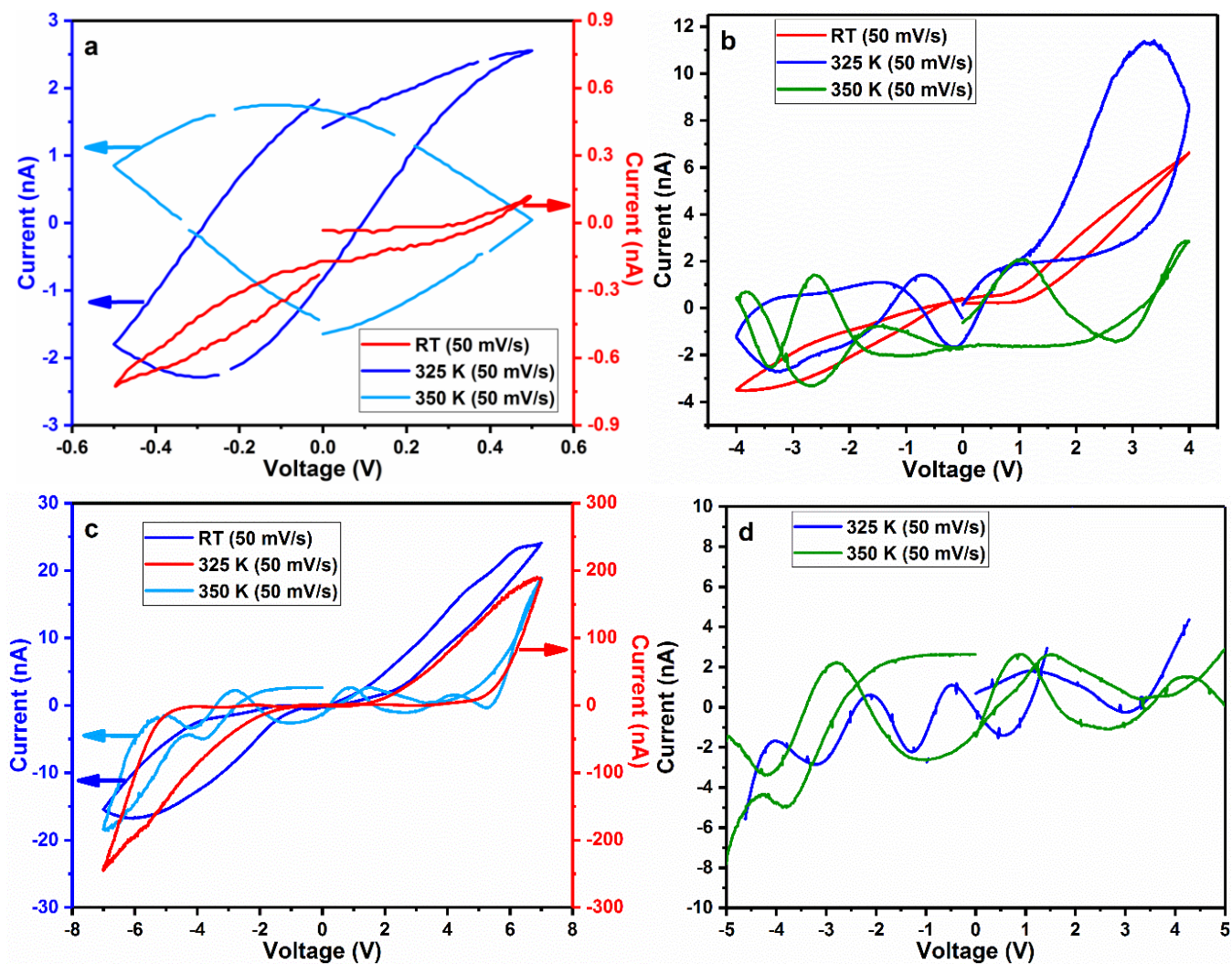
Figure A3.7. Cyclic voltammetry (CV) scans of (a) ±0.5, (b) ±4, c) ±7 V at room temperature, 325, and 350 K. (d) Magnified CV scans at 325 and 350 K.

Under the conditions used in these devices for poling and operation we do not observe any redox based degradation of the perovskite occurring. The repeated current voltage measurements shown above show that the perovskite layer is not changing in performance. To further corroborate this result, CV was done on the device with a two-electrode setup. The CVs were done for different voltage ranges and at different temperatures. At room temperature the CVs for voltage ranges of ± 0.5V, ± 4V and ± 7 V at scan speeds of 50 mV sec⁻¹ do not show any observable redox associated peak or a sudden increase in current indicating the start of a redox process. Further we do not observe any significant capacitive currents that would indicate the presence of ion diffusion and back

95

diffusion currents. On increasing the temperature to 325 K, we observe that the currents in the CV's increase and the capacitive nature of the device, as illustrated by increased hysteresis, is also amplified due to increased mobility of the ions. We start to observe redox signature in the scans. At 350 K at lower voltages (± 0.5V) a much higher capacitive behavior is observed from the greater hysteresis in the current response. At higher voltages (± 4, ± 7) we start to see the appearance of maxima's and minima's in the current indicating the start of redox processes.
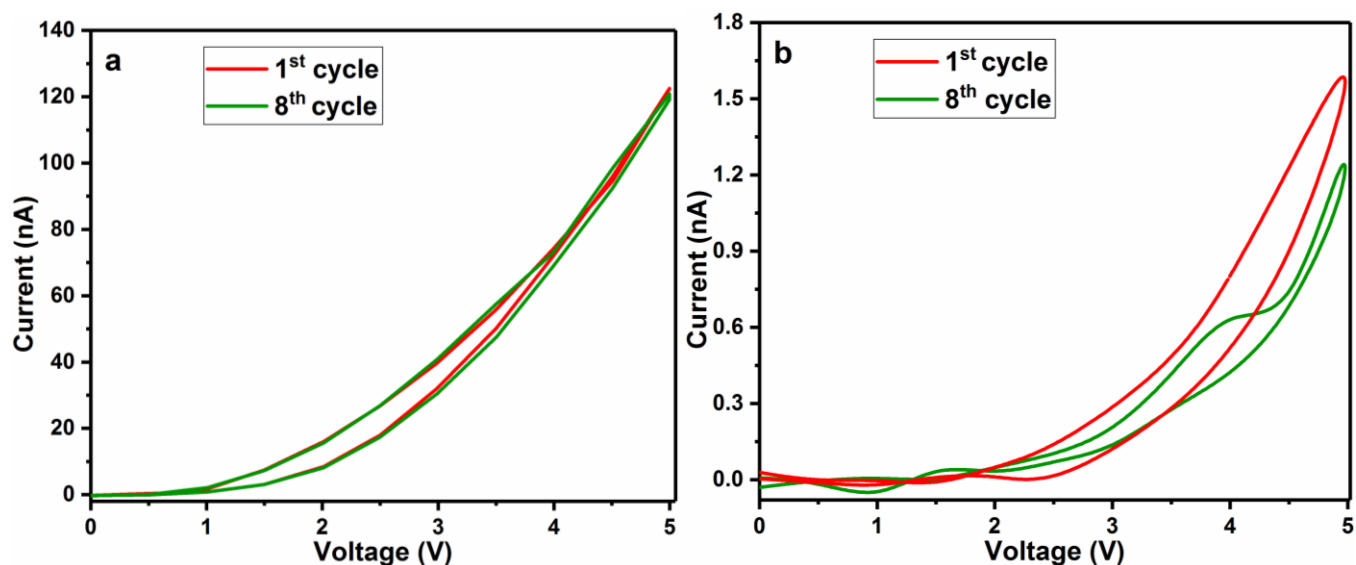
Figure A3.8. *I-V* scans (a) before and (b) after redox CV cycles at 350 K.

The current decreases substantially following these redox processes indicating the formation of PbI_2. We confirm this by conducting a *I-V* scan on the device following the observation of the redox peak, compared to a device exposed to only room temperature processing we observe that the current has decreased substantially. On poling this device under the p-n conditions we do not observed any J_{SC} or V_{OC}.
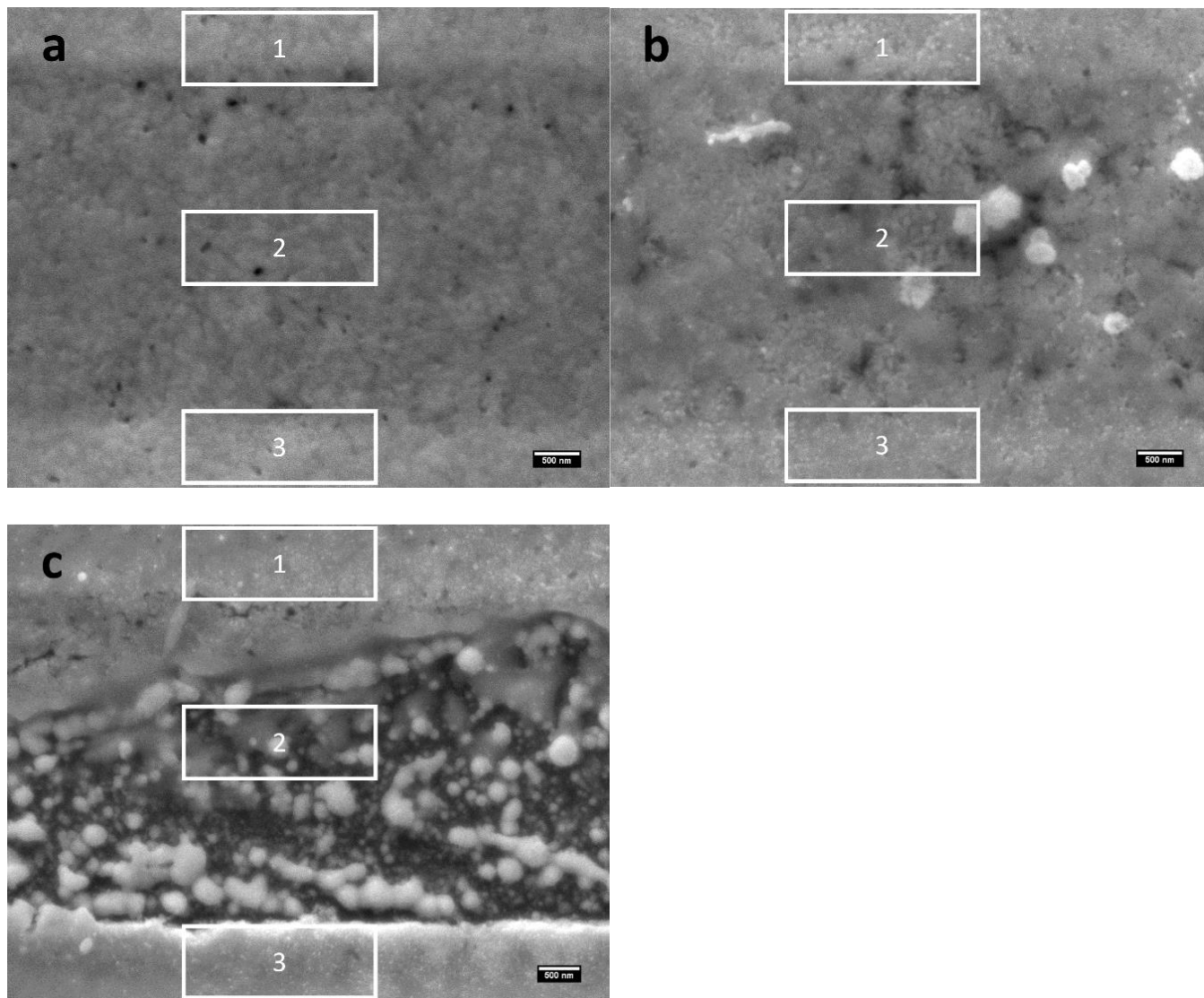
Figure A3.9. FESEM images of the device at (a) room temperature (RT), (b) 350 K after 8 CV cycles and (c) 350 K after processing at 70 V.

Table A3.1. Summary of atomic percentage ratio of the device under three different conditions.

I/Pb (Atomic percentage ratio)	Region 1	Region 2	Region 3
After processing at 7 V (RT)	3.12	3.04	3.07
After 8 CV cycles at 7 V (350 K)	2.23	3.10	2.83
After processing at 70 V (350 K)	2.04	1.46	2.55

FESEM images of the devices after CV scans at room temperature does not shown any change but at 350 K (after 8 CV cycles and after processing at 70 V) we observe that the morphology of the perovskite layer has changed. The elemental analysis (EDX) (Table A3.1) also shows that the ratio of I:Pb is close to 3:1 in the device processed at room temperature (corresponding to $MAPbI_3$), while in the 350 K devices it progressively changes to closer to 2:1, indicating the formation of PbI_2. These results confirm that redox processes do lead to degradation of the perovskite layer to PbI_2 at higher temperature and applied bias. The conditions used for our device operation do not lead to any observable degradation of the perovskite layer and any appreciable ion diffusion current.
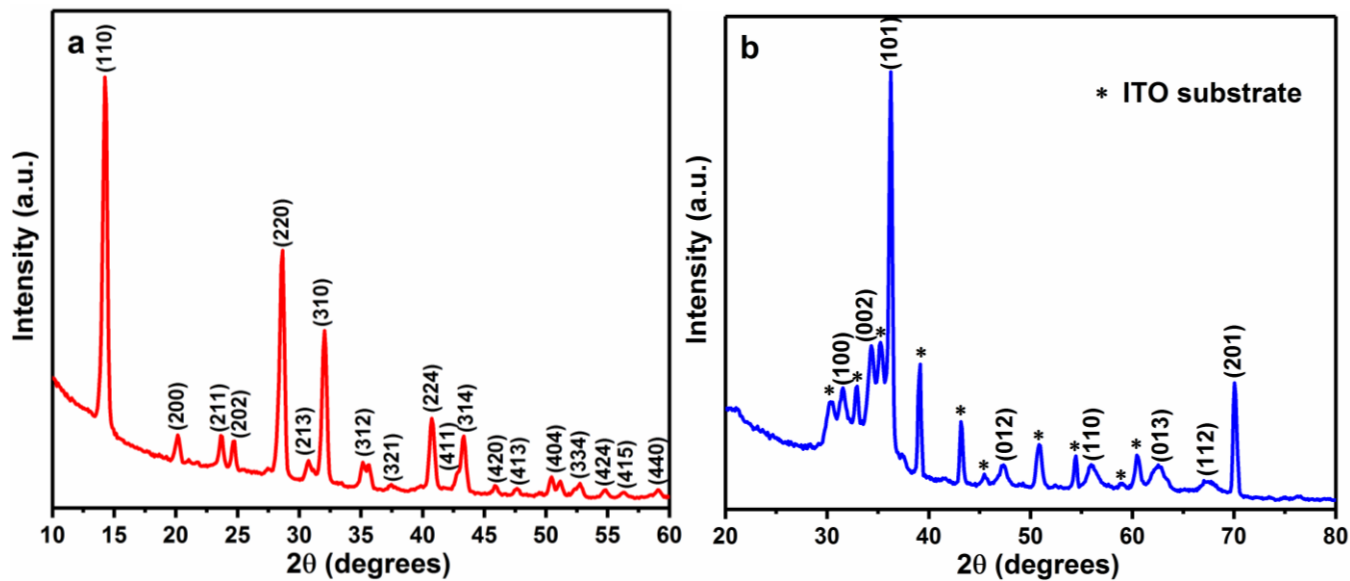
Figure A3.10. Indexed X-ray diffraction patterns of (a) MAPbI₃ film with tetragonal structure and (b) ZnO nanosheets on ITO substrate. Both XRD patterns are measured at room temperature.

The sharp intense peak in Figure A3.10a reveals the crystalline nature of MAPbI₃. The MAPbI₃ film gives diffraction peaks at 14.22, 28.66, 32.13, 40.59 and 43.21°, which can be assigned to the (110), (220), (310), (224) and (314) planes of the tetragonal perovskite structure with $a = 8.874$ Å and $c = 12.671$ Å. It exhibits tetragonal symmetry with *I*4/*mcm* space group. The XRD pattern of the ZnO sheets (Figure A3.10b) shows that they are oriented along the (101) [or (10$\bar{1}$0)] plane and highly crystalline.
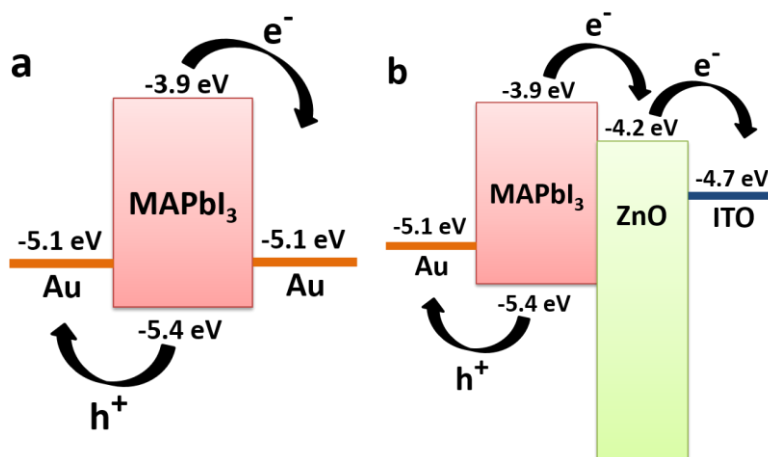
Figure A3.11. Energy level diagram of the (a) Au/MAPbI₃/Au and (b) Au/MAPbI₃/ZnO devices.
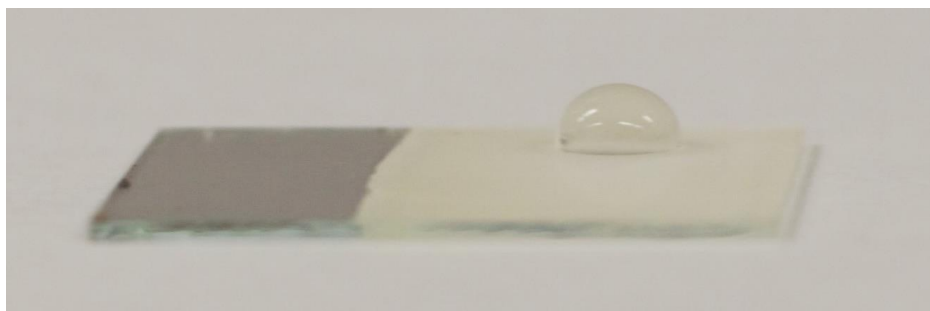
Figure A3.12. Optical image showing the hydrophobicity of ZnO nanostructure.

The degradation of the perovskite layer due to interaction with ambient oxygen and moisture is well known. In these devices since the perovskite layer is interfaced with ZnO sheets we observe no degradation even after 5 days. This is attributed to the fact that the ZnO layer limits the direct interaction between the perovskite and ambient species. Also ZnO sheets are hydrophobic in nature and hence repel moisture, further limiting the degradation of the perovskite layer. The optical images below (Figure A3.13) show that the perovskite region covered with ZnO (Figure A3.13a) shows no color change even after 5 days while exposed perovskite has changed to yellow color within 1 day signifying its degradation to PbI_2. The device after 5 days is still operable though there is some loss in J_{SC}, which is recovered by repoling.
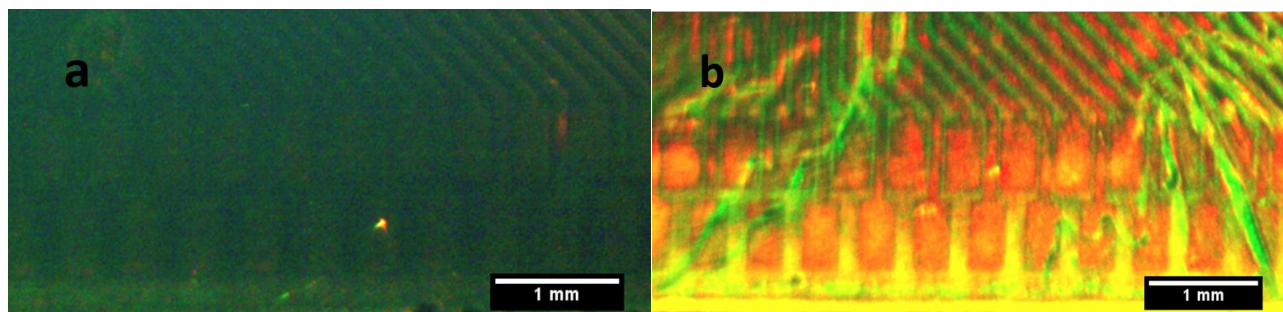
Figure A3.13. Optical images of (a) ZnO covered $MAPbI_3$ on Au chip and (b) exposed region showing degradation after 5 days.
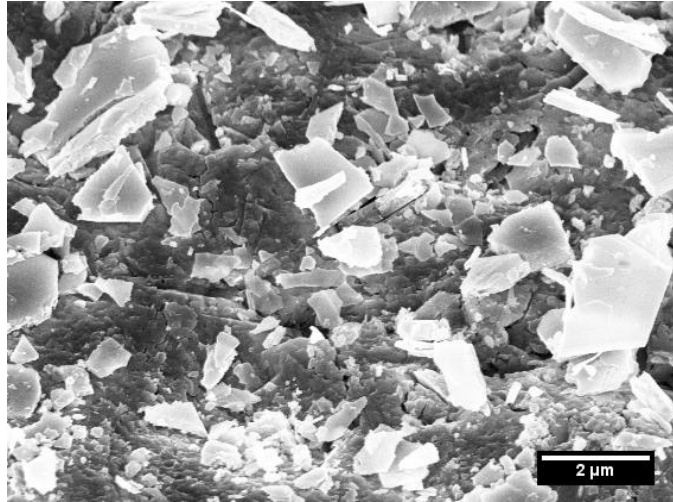
Figure A3.14. FESEM image showing the broken ZnO sheet fragments on perovskite layer after applying high pressure (500 kPa).

The device failure occurs at pressures exceeding 500 kPa due to the breakage of the ZnO sheets. FESEM images of such as device clearly show multiple ZnO sheet fragments on the perovskite layer indicating the failure of the ZnO sheets.
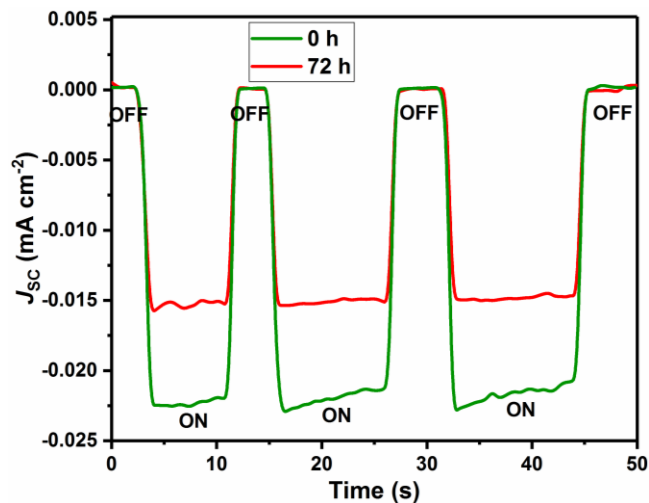

Figure A3.15. Loss in base Jsc of the device after 72 hours.

The time-based mode of failure is due to the loss of poling effect. The base J_{SC} (at base pressure) as seen decreases by 30% which we consider as the limit for stable operation. On repoling the device though the performance is recovered.
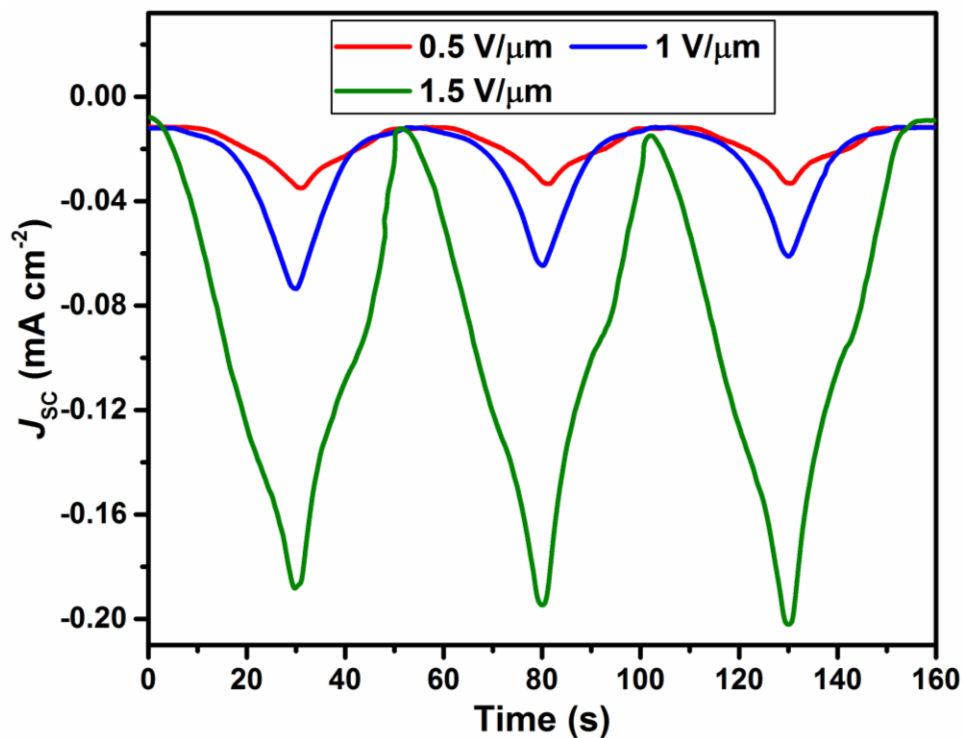
Figure A3.16. J_{SC} cycles of the tactile sensor (ZnO sheets and ferroelectric-semiconducting nature of MAPbI$_3$) for different poling electric fields in air under 1.0 sun illumination with a maximum 37 kPa pressure.

It is observed that the J_{SC} response is dependent on the poling field strength and is increasing with the increase in the poling field strength. With the increase in the pressure from 0 to 37 kPa, the interfacing area between the ZnO sheets and MAPbI$_3$ film will effectively increase which will lead to a higher charge collection resulting in increased J_{SC}.
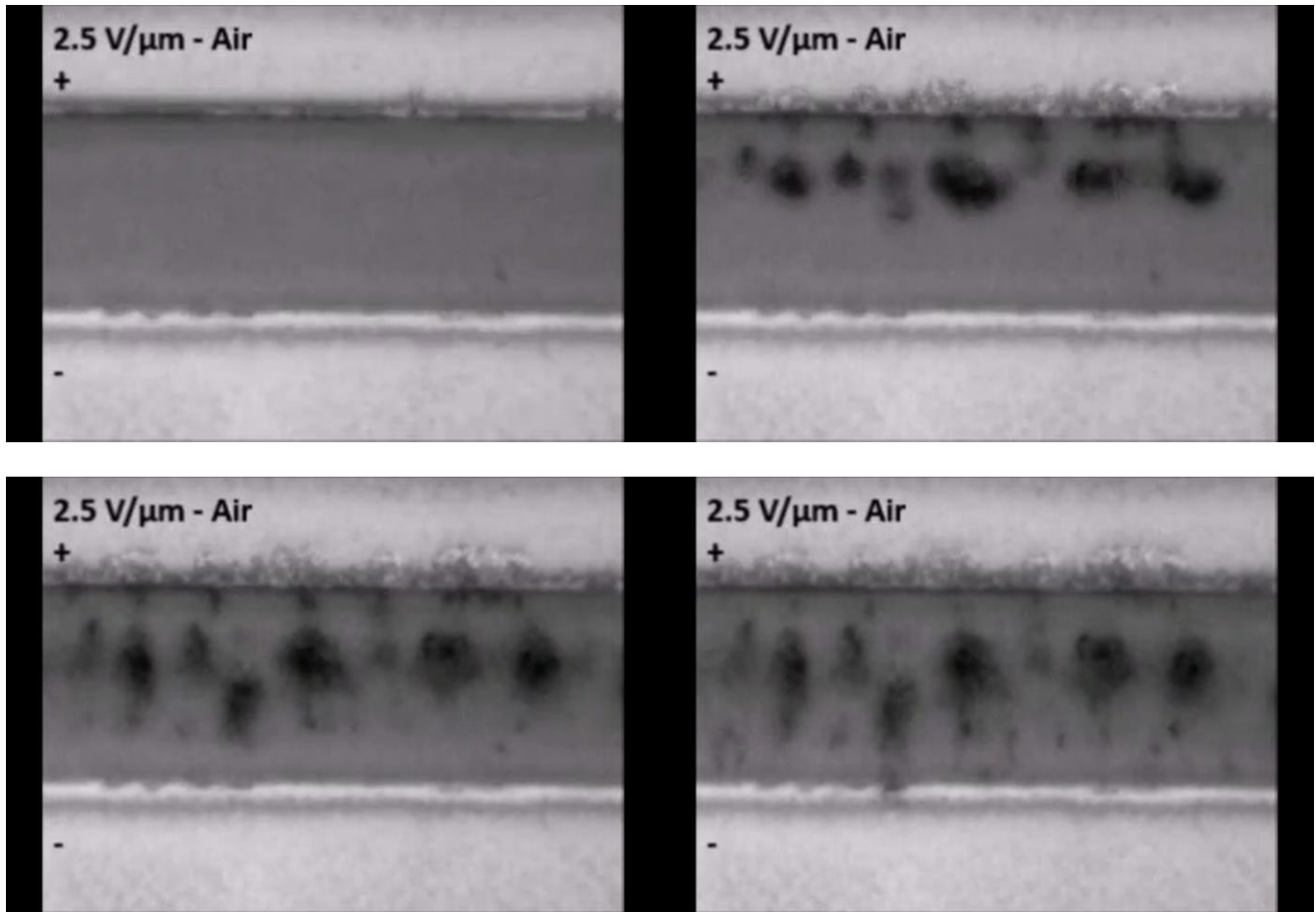
Photo A3.1. Constant poling voltage at 2.5 V µm^{-1} in air (images taken every 3 s).
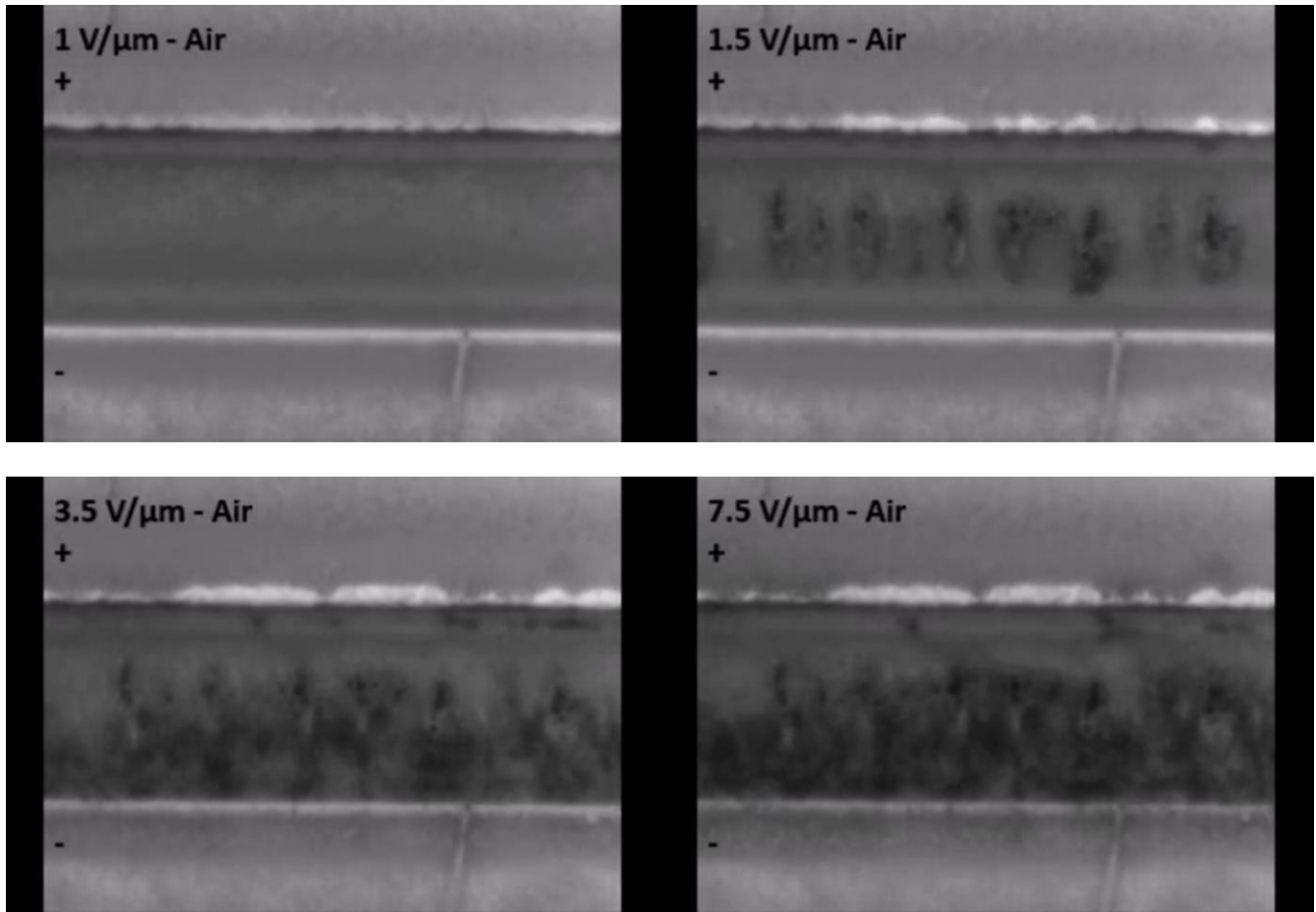
Photo A3.2. Increasing poling voltage from 0 to 7.5 V µm^{-1} in air (images taken every 10 s).

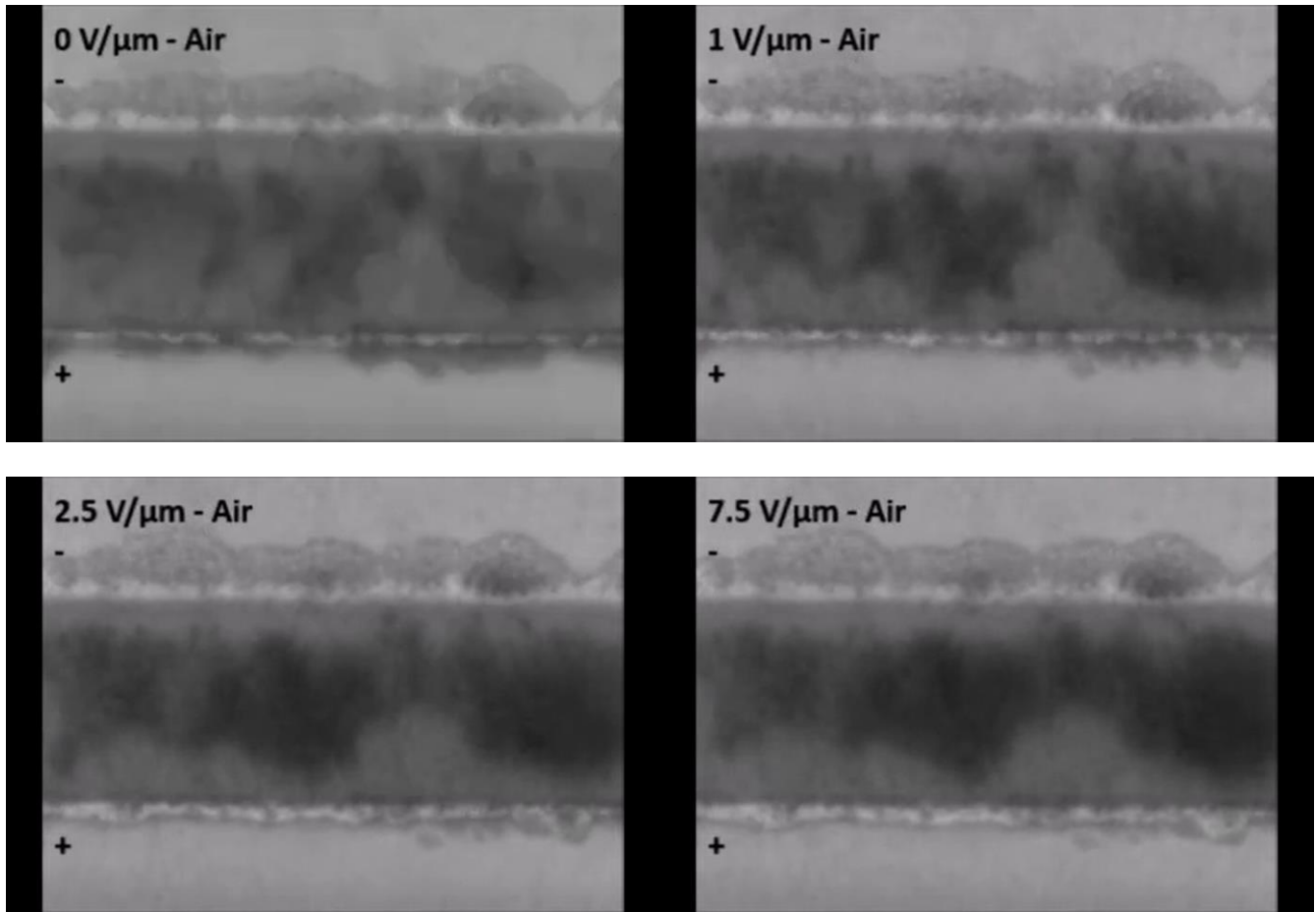**Photo A3.3.** Reversing poling field direction (images taken every 1 s).
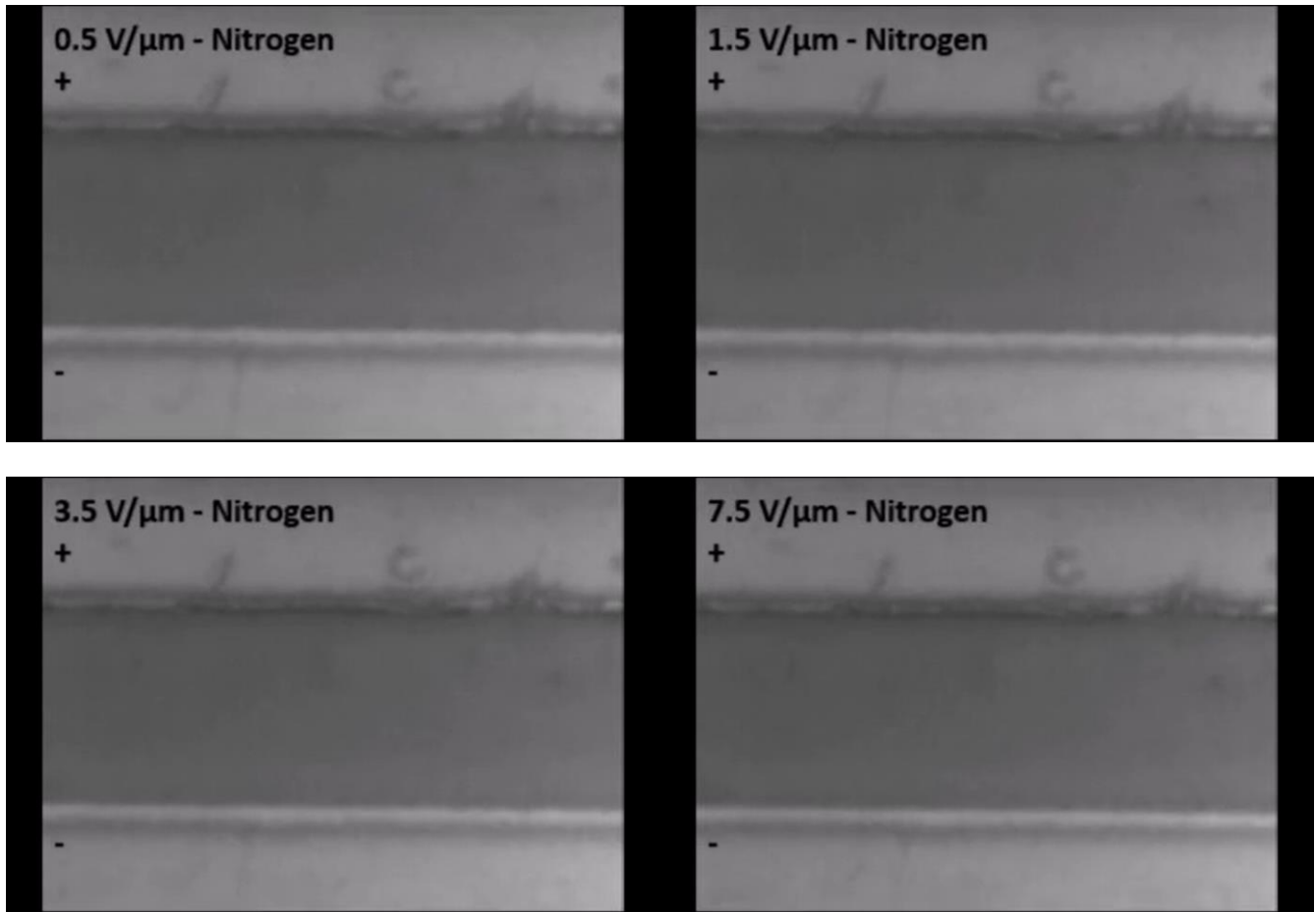
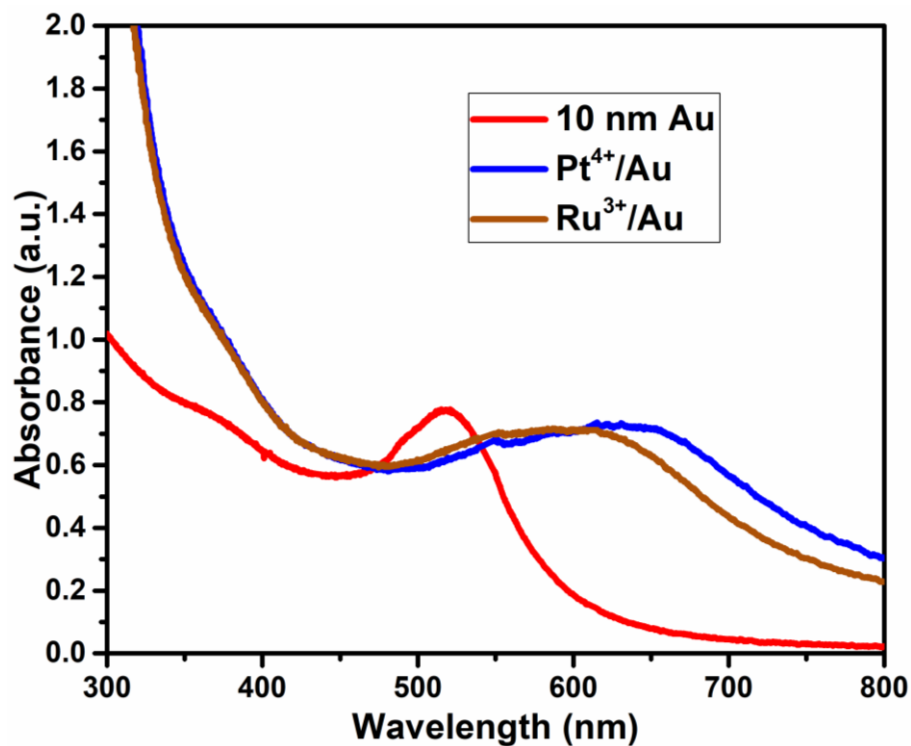**Photo A3.4.** Increasing poling voltage from 0 to 7.5 V μm^{-1} in N_2 (images taken every 10 s).

Figure A4.1. UV-Vis spectrum of metal cations assembled chains.

Table A4.1. Average size and zeta potential value measured using DLS.

Sample number	Size (nm)	Zeta potential (mV)
1	198.4	-38.5
2	223.8	-37.2
3	226.4	-33.4
4	190.8	-41
5	188.6	-33.3
6	245.5	-36.1
7	229.5	-33.6
8	277.7	-34.5
Average	222.6	-35.6
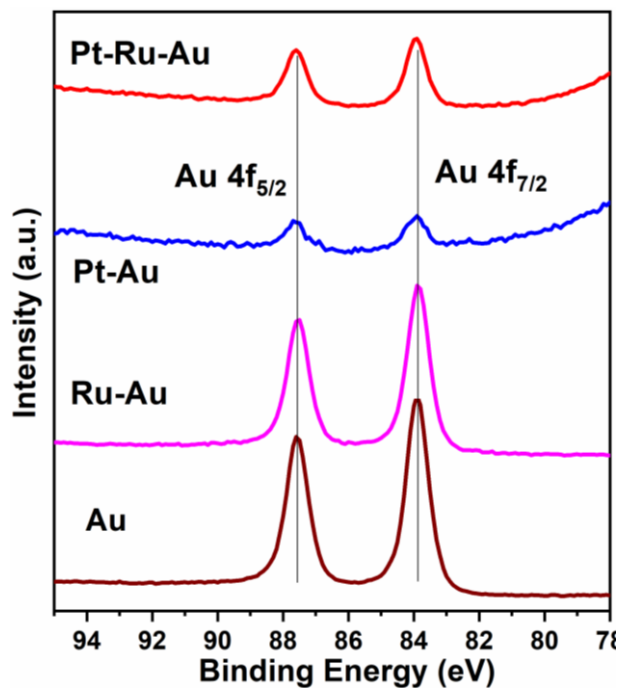
Figure A4.2. XPS spectra of plain Au nanoparticles, Ru-Au, Pt-Au, and Pt-Ru-Au nanocomposites.
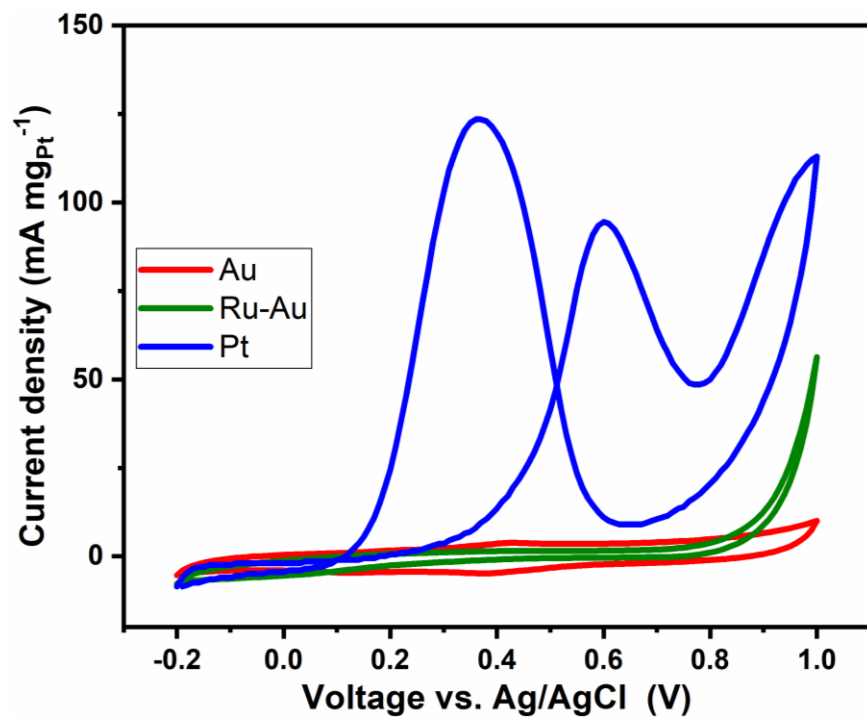

Figure A4.3. CVs of EOR measurements in 0.1 M $HClO_4$ and 1 M ethanol at 50 mV s^{-1} of plain Au nanoparticles, Ru-Au nanocomposite, and reduced Pt^{4+} in water without the Au nanoparticle chains.
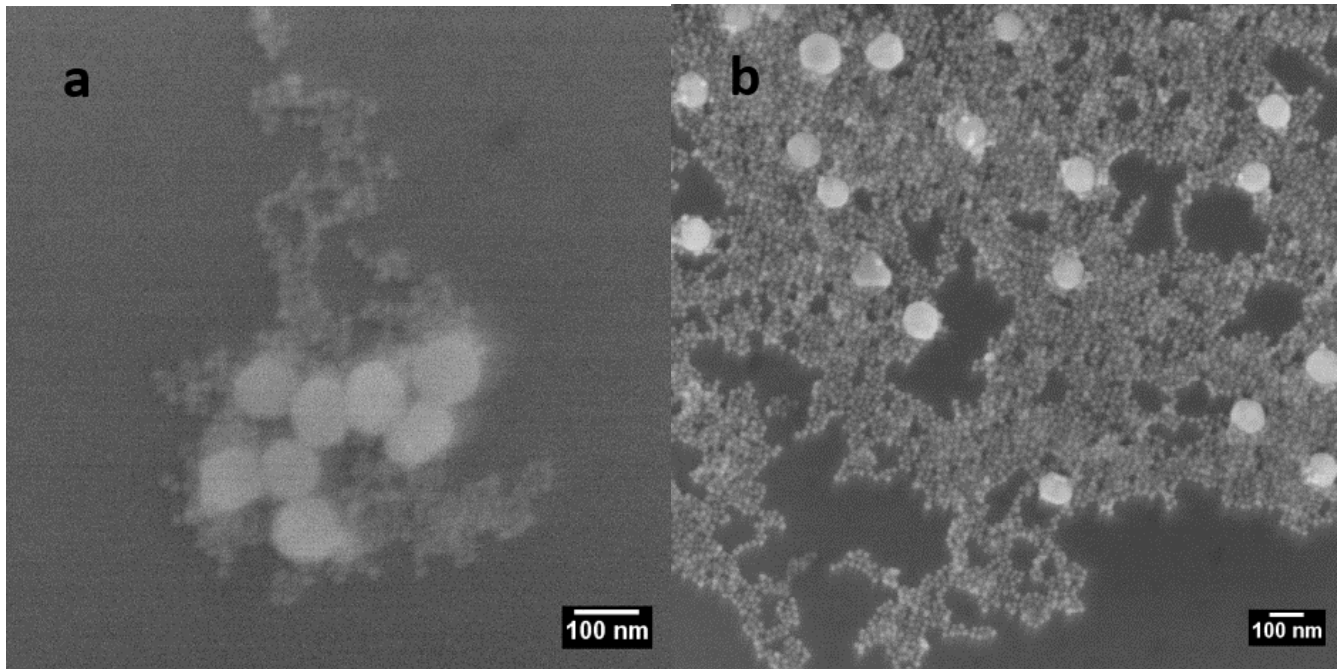
Figure A4.4. FESEM images of assembled 10 nm and 100 nm Au nanoparticles mixed at different stages: (a) two solutions mixed after self-assembly, (b) mixed at the beginning before the self-assembly.